Spring 5-2-2023

Radar Signatures in Tropical Cyclone Tornadic and Nontornadic Supercells

Michaela Wood
University of Nebraska-Lincoln, mwood@huskers.unl.edu

RADAR SIGNATURES IN TROPICAL CYCLONE TORNADIC AND NONTORNADIC SUPERCELLS

by

Michaela J. Wood

A THESIS

Presented to the Faculty of

The Graduate College at the University of Nebraska

In Partial Fulfillment of Requirements

For the Degree of Master of Science

Major: Earth and Atmospheric Sciences

Under the Supervision of Professor Matthew S. Van Den Broeke

Lincoln, NE

May 2023

RADAR SIGNATURES IN TROPICAL CYCLONE TORNADIC AND NONTORNADIC SUPERCELLS

Michaela J. Wood, M.S.

University of Nebraska, 2023

Advisor: Matthew S. Van Den Broeke

Tropical cyclones (TCs) contain highly-sheared environments that are conducive for supercell thunderstorms. These TC supercells sometimes produce tornadoes, often with little warning. Given the often-close proximity of tornadic and nontornadic TC supercells, environments may not be well-distinguished, pointing to the potential value of radar observations. In this study, dual-polarimetric radar signatures of a sample of TC supercells are examined in the context of known supercell structure and microphysics. Tornadic and nontornadic TC supercells are compared with their midlatitude counterparts, and the environments and characteristic structure of these storms are shown to be notably different. An attempt is made to distinguish differences between tornadic and nontornadic TC supercells that may hold operational promise. Prior research has only examined dual-polarimetric TC supercells using a case study approach; therefore, this study aims to create a more comprehensive picture with a large sample of cases. Differential reflectivity (Z_{DR}) columns remained shallower in TC supercells when compared to their midlatitude counterparts. Z_{DR} columns were also much rarer in TC cases than in midlatitude cases, making Z_{DR} columns an unreliable proxy for updraft characteristics in TC cases. However, no significant differences were present between

Z_{DR} columns in tornadic and nontornadic TC supercells. Z_{DR} arc remained as pronounced in TC supercells as they are in midlatitude cases, with maximum and mean Z_{DR} values within the signatures being larger in TC cases. This is likely due to the increased low-level wind shear in TC cases promoting more effective drop size sorting. Separation angle between the specific differential phase (K_{DP}) foot and Z_{DR} arc was larger in TC supercells than midlatitude supercells, again due to the increased low-level wind shear and drop size sorting. The inverse was seen with a normalized separation distance between the two signatures. Neither separation angle nor distance between the K_{DP} foot and Z_{DR} arc gave an indication of tornadic potential in TC supercells. The key finding from this research is that tornadic TC supercells had significantly stronger low-level mesocyclones as measured by normalized rotation (NROT) than nontornadic TC supercells.

Acknowledgements:

I would like to acknowledge my advisor, Professor Matthew Van Den Broeke for taking me on as a graduate student. I greatly appreciate his sharing of knowledge and guidance throughout this project. I am extremely grateful for all of the conversations and discussions that took place, helping me learn and gain new insights as a meteorologist. I would also like to acknowledge Matthew Wilson for allowing me to use his Python algorithm for this project and all of the guidance he has provided throughout multiple facets. I would like to acknowledge my committee members, Professor Adam Houston and Dawn Kopacz for their time and feedback on this thesis. I appreciate all of the eye opening and thoughtful conversations with my graduate colleagues in the Department of Earth and Atmospheric Sciences, including Devon Healey, Raychel Nelson, and Benjamin Schweigert. Finally, I would like to acknowledge my wonderful family for their continued support throughout my career. This work could not have been completed without them. I acknowledge NOAA grant NA19OAR4590340 and USDA grant USDA-NIFA-TCRGP-006773 for providing financial support for this project.

Table of Contents

Multimedia Objects

Chapter I: Introduction

Supercells are thunderstorms with a rotating updraft and a downdraft that is displaced due to vertical wind shear (Browning 1962; Weisman and Klemp 1982). It is important to gain a deep understanding of these storms as 90% of them produce severe weather at some point in their lifetime (Burgess and Lemon 1991). Supercells may be embedded within rainbands of tropical cyclones (TCs). These supercells are typically smaller in both the horizontal and vertical extent when compared to a typical midlatitude supercell (Edwards 2012), however their lifetime can range from minutes to several hours (McCaul 2004). TC supercells may also spawn tornadoes. TC tornadoes are typically weak (EF0-EF2) and account for 3.4% of all United States tornado occurrences (Schultz and Cecil 2009). The small size and extent of these supercells make it difficult for operational meteorologists to issue timely warnings.

A hodograph, a useful tool for assessing vertical wind profiles, can help to show supercell-favorable environments. Wind shear, the change in wind speed and direction with height, can be determined with a hodograph. A supercell-favorable hodograph includes a wind profile that increases in speed and veers (turns clockwise) with height (Weisman and Klemp 1982; Bunkers et al. 2000). Rotation within a supercell's updraft is created by the ingestion of streamwise vorticity (Wilhelmson and Klemp 1978; Davies-Jones 1984). The vertically integrated flux of streamwise vorticity that a supercell may ingest can be calculated from a hodograph with storm-relative helicity (SRH; Moller et al. 1994; Rasmussen and Blanchard 1998).

Thermodynamic environmental variables are also important when assessing if an environment favors supercells. Convective available potential energy (CAPE) is a

measure of the integrated work that the buoyancy force can perform on a parcel as it travels vertically through the atmosphere. CAPE may also be used as a proxy for potential updraft strength. Prior research has consistently shown that supercell environments typically present larger values of CAPE than nonsupercell environments (Parker 2014; Coffer et al. 2019; Coniglio and Parker 2020).

TC environments are typically characterized by large amounts of shear and small buoyancy. With an often-close proximity between tornadic and nontornadic TC supercells, the use of large environmental differences to aid in the decision-making process is typically ruled out (Spratt et al. 1997). This indicates the value of radar data when issuing timely tornado warning for TC supercells. A proper understanding of the use of dual-polarimetric radar signatures could prove extremely valuable for operational meteorologists.

The Next Generation Weather Radar (NEXRAD) network consists of 160 Weather Surveillance Radar-1988 Doppler (WSR-88D) radars across the United States, with upgrades to dual-polarimetric capabilities completed between 2011 and 2013. Dual-polarization (dual-pol) radars are different than conventional radars as they transmit and/or receive pulses in two orthogonal orientations: the horizontal and the vertical. The inclusion of two orientations provides better insight into the characteristics of scatterers in a sample volume. Repeatable dual-pol signatures have been well-studied in prior literature in the context of midlatitude supercells. Microphysical processes and storm-scale dynamics can be inferred from these repeatable signatures (Kumjian and Ryzhkov 2008). These signatures include the differential reflectivity (Z_{DR}) column (e.g., Caylor and Illingworth 1987; Conway and Zrnić 1993; Kumjian and Ryzhkov 2008; Kumjian et

al. 2014), Z_{DR} arc (e.g., Ryzhkov et al. 2005; Kumjian and Ryzhkov 2007, 2008; Dawson et al. 2014), the specific differential phase (K_{DP}) foot (e.g., Romine et al. 2008; Crowe et al. 2010, 2012), the separation distance and angle between the Z_{DR} arc and K_{DP} foot (e.g., Crowe et al. 2010, 2012; Loeffler and Kumjian 2018) and hail signature (Kumjian and Ryzhkov 2008; Van Den Broeke 2020).

In this thesis, repeatable dual-polarimetric signatures will be quantified for a large sample of both tornadic and nontornadic TC supercells. These signatures in TC supercells will be compared with midlatitude signatures in order to establish differences between TC supercell signatures and their midlatitude counterparts. Signatures will also be compared between tornadic and nontornadic TC supercells in order to establish differences that may give insights into a TC supercell's tornadic potential. Establishing these differences could prove beneficial to operational meteorologists in issuing timely warnings and lowering false alarm ratios for tornado warnings. Chapter 2 will provide background on midlatitude supercells, TC supercells, and the dual-polarimetric radar signatures of both, as well as hypotheses. Chapter 3 will include information on the data and methodology. This will include the process by which TC supercells are identified, the quantification of dual-polarimetric signatures and environmental variables, and statistical comparison methods. Chapter 4 will detail the results of this study. Chapter 5 will include conclusions and a discussion of the results.

Chapter II: Background

2.1: Midlatitude Supercells and Tropical Cyclone Supercells

a. Supercells

A supercell is a thunderstorm with a persistent rotating updraft. The term was first introduced by Browning (1962) and defined as a thunderstorm with a rotating updraft and a downdraft displaced by the vertical wind shear (Browning 1964; Weisman and Klemp 1982). Supercells are important to understand and forecast as 90% of them produce severe weather (i.e., strong winds, hail, flash flooding, tornadoes; Burgess and Lemon 1991). Updraft persistence is essential for a supercell, with circulation lasting for at least 30-45 minutes (Moller et al. 1994). One of the first detailed conceptual models of a supercell was constructed by Lemon and Doswell (1979) (Figure 2.1). The model consists of a divided mesocyclone with two downdrafts, one on the rear flank, the rear flank downdraft (RFD) and one on the forward flank, the forward flank downdraft (FFD). The divided mesocyclone in this model has a center of circulation separating the RFD and FFD as a result of horizontal vorticity tilting into the vertical (Wilhelmson and Klemp 1978; Lemon and Doswell 1979).

A supercell is made up of a towering cumulonimbus cloud with a large, flat cloud shield called an anvil spreading over the upper levels (Figure 2.2; Moller et al. 1994). In a strong supercell, an overshooting top penetrates above the anvil and into the tropopause. An abrupt cloud lowering under the rain-free cloud base is called a wall cloud, usually located under the strongest portion of the updraft. An intense wall cloud with rapid rotation may be associated with tornadogenesis. Along the forward flank, an inflow tail

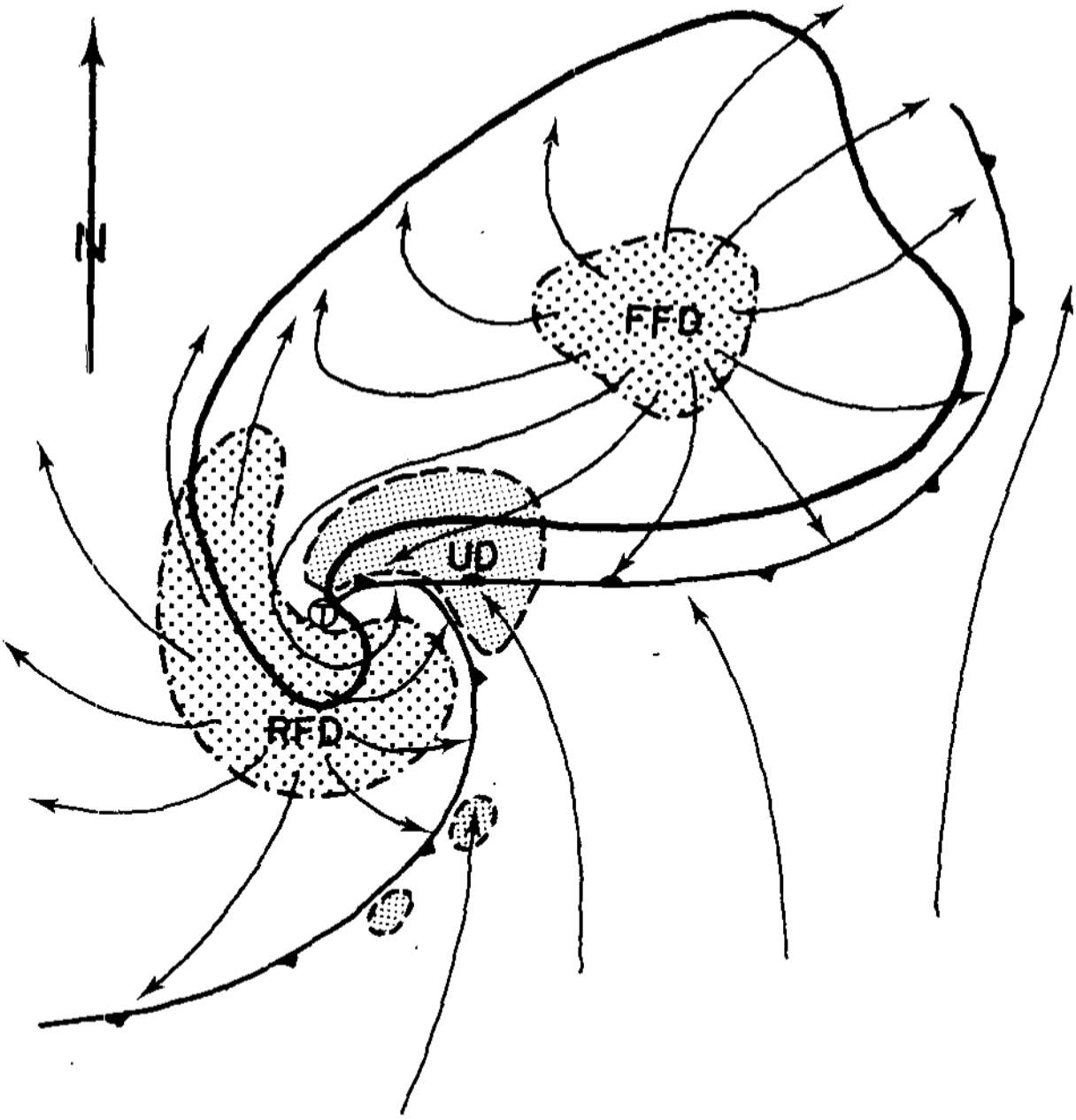

Figure 2.1: Plan view schematic of a tornadic supercell at the surface. Thick black line corresponds to the radar echo. The solid line and frontal symbols indicate the “gust front”. Shaded regions correspond to the surface position of the updraft (UD), rear flank downdraft (RFD) and forward flank downdraft (FFD) along with the associated streamlines. Location of the tornado is marked with a circled ‘T’. [Figure 7 from Lemon and Doswell (1979)]

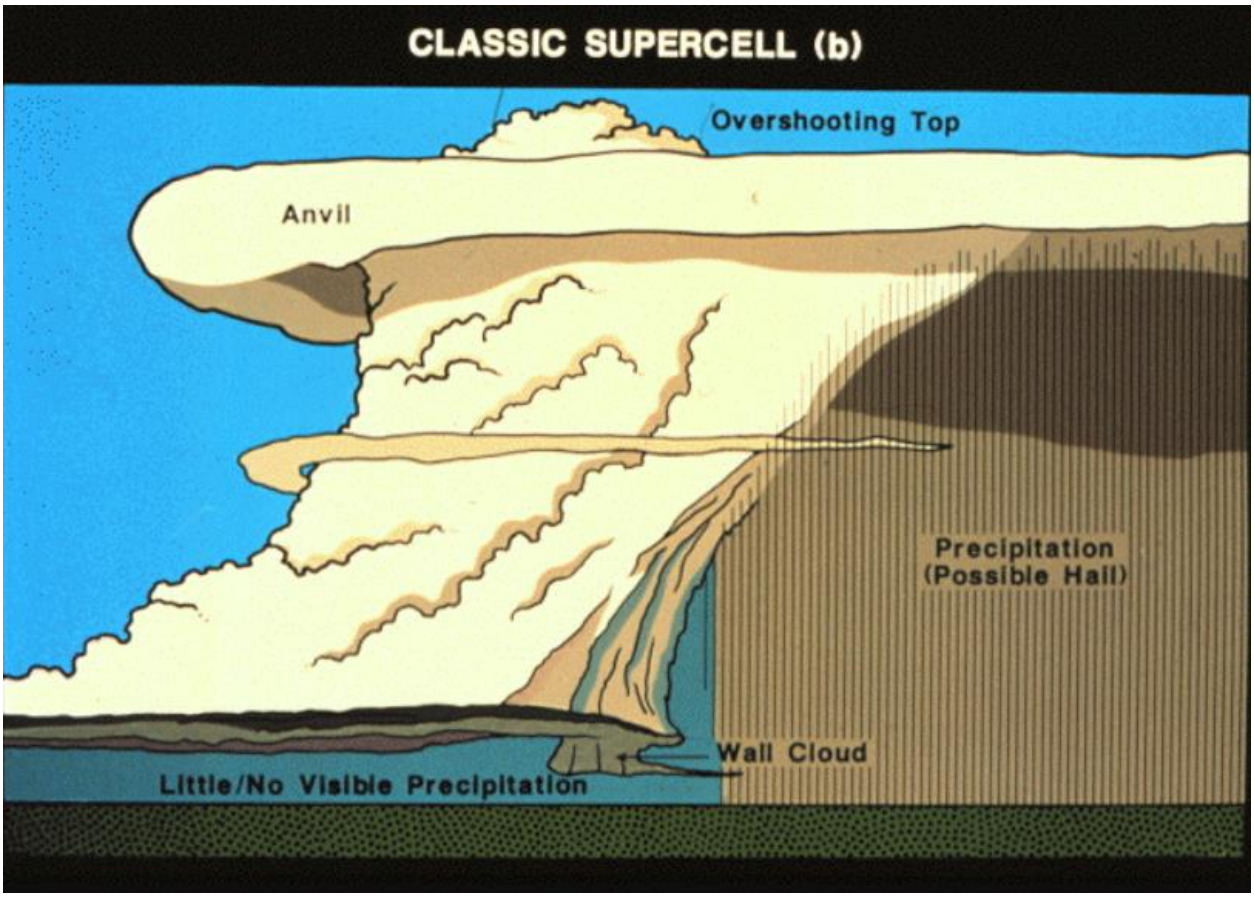

Figure 2.2. Classic supercell structure with an anvil, overshooting top, wall cloud, and precipitation core. [Figure from Doswell and Burgess (1993)]

cloud may be attached to and feeding the wall cloud. Adjacent to the updraft is the flanking line, comprised of cumulus clouds from the organized lift of warm air being ingested into the main updraft. On a radar image, a supercell may have a "hook echo" shape with an appendage indicating the mesocyclone. The bounded weak echo region (BWER) is an area of low reflectivity encircled by an area of higher reflectivity that is observed in some supercells and is evidence of the updraft.

The ingestion of streamwise vorticity is the primary source of rotation for a supercell's updraft (Wilhelmson and Klemp 1978; Davies-Jones 1984). A hodograph is a useful tool for examining helicity, a necessary ingredient for supercells. Supercell-favorable hodographs have wind that increases in speed and veers (turns clockwise in the northern hemisphere) with height (Weisman and Klemp 1982; Kerr and Darkow 1996; Bunkers et al. 2000; Thompson et al. 2003). Calculated from a hodograph, storm-relative helicity (SRH) is a parameter that quantifies the vertically integrated flux of streamwise vorticity that may be ingested into a supercell. SRH has been correlated with the longevity and intensity of supercells (Moller et al. 1994; Rasmussen and Blanchard 1998; Thompson et al. 2003). SRH values may also be used to understand dynamic pressure perturbations that form in the presence of strong rotation in a mesocyclone. A strong mesocyclone is favored with large values of SRH, meaning a large upward dynamic perturbation pressure gradient force will be associated with the pressure falls under the mesocyclone (Davies-Jones 1984; Markowski and Richardson 2014). Bulk shear is another parameter that can help differentiate between supercell and nonsupercell environments as it measures the bulk wind differences over a layer of the environment (Thompson et al. 2003, 2007; Houston et al. 2008).

Thermodynamic variables may also be used to characterize supercell environments. For parcels experiencing forced ascent, the height of the lifted condensation level (LCL) gives a reasonable cloud base height estimate. Previous work has consistently shown that supercell environments have lower LCL heights than nonsupercell environments (Thompson et al. 2003; Parker 2014; Coffer et al. 2019; Coniglio and Parker 2020). Convective available potential energy (CAPE) is a measure of the integrated work that the buoyancy force can perform on a parcel as it travels vertically through the atmosphere. CAPE is used as a proxy for atmospheric instability and gives insight into potential updraft strength. Surface-based CAPE (SBCAPE) is calculated for a parcel that originated at the surface and is then lifted to its LFC. Mixed-layer CAPE (MLCAPE) is calculated for air parcels in the lowest 100 hPa when lifted to the level of free convection (LFC); this parameter gives a representation of the air near the surface that the updraft may ingest. Most unstable CAPE (MUCAPE) is calculated for the most unstable parcel of air in the lowest 300 hPa of the atmosphere when lifted to its LFC. Studies consistently show that supercell environments typically present larger values of CAPE than nonsupercell environments, and values increase monotonically from nonsupercells to significantly tornadic supercells (≥F/EF2) (Thompson et al. 2003; Parker 2014; Coffer et al. 2019; Coniglio and Parker 2020).

The vertical pressure gradient in a mid-level mesocyclone contributes to the intensity of the updraft. However, in order for tornadogenesis to occur, a low-level mesocyclone (generally 500m – 1500m above ground level) is also needed (Markowski et al. 2008; Orf et al. 2017; Yokota et al. 2018). A low-level mesocyclone is connected to the mid-level mesocyclone and may help to support a tornado (Markowski 2002). It has

been theorized that the low-level mesocyclone forms and intensifies as the RFD tilts horizontal vorticity from the warm sector and FFD air into the mesocyclone (Markowski et al. 2008; Nowotarski et al. 2015; Mashiko 2016). An upward acceleration is generated from the pressure drop at the center of a low-level mesocyclone that in turn strengthens the low-level mesocyclone and leads to surface convergence, stretching the vertical vorticity near the surface and helping contribute to tornadogenesis if sufficient buoyancy is present (Markowski 2007; Davies-Jones 2015; Yokota et al. 2018). Previous research indicated that less than 30% of supercells produce tornadoes, motivating further exploration of the mechanisms responsible for tornadogenesis in these storms (Trapp et al. 2005).

b. Tropical Cyclone Supercells

Tropical cyclone (TC) rainbands often contain embedded convective cells with mesocyclones. These TC supercells have been described thoroughly in previous literature and have some contrasting features from the typical midlatitude supercell. These TC supercells show similarities to a midlatitude "miniature" supercell as they are smaller in horizontal and vertical extent (Davies 1990; Knupp et al. 1998; Edwards 2012). Although TC supercells may have relatively weak rotation, their lifetime can range from minutes to several hours (McCaul 2004; Edwards 2012). However, the size and extent of these storms makes it difficult to issue timely severe thunderstorm and tornado warnings.

Compared to a midlatitude supercell environment, tropical cyclone environments have increased lower-tropospheric vertical wind shear (McCaul 1991). TCs near the U.S. Atlantic and Gulf coasts may experience an enhanced vertical wind profile due to favorable interactions with the ambient westerlies (Molinari and Vollaro 2010).

Buoyancy is also much smaller in TC environments than in a Great Plains supercell environment (McCaul 1991). However, convective inhibition is limited, therefore only a small amount of lift is needed for deep convection initiation to occur in these buoyant areas (Green et al. 2011). A large amount of deep-tropospheric moisture in TC environments also leads to decreased lapse rates and smaller CAPE values (Edwards 2012).

Supercells are favored in the northeast (right-front) sector (with respect to the TC motion) of most Northern Hemisphere TCs as SRH is maximized down-shear from the TC center in a region co-located with maximum instability (Molinari and Vollaro 2010). Supercells are most common in the outer region (> 200 km from the center) of a TC within 48 hours of landfall with a diurnal peak in the afternoon. Inner region supercells are most common within 12 hours of landfall and show no diurnal bias (McCaul 1991; Schultz and Cecil 2009). Wind speeds are typically maximized in the eyewall, however vertical wind shear increases away from the eye wall (McCaul 1991; Molinari and Vollaro 2008). The convective mode near the TC center favors nonsupercell convection (Edwards 2012).

Tropical cyclone supercells may also spawn tornadoes. In an analysis conducted on a dataset containing tornadoes from 1950 to 2007, over 1800 tornadoes were associated with TCs, accounting for an estimated 3.4% of all United States tornado occurrences (Schultz and Cecil 2009). Strength of these TC tornadoes included 81.1% weak (F0-F1), 13.8% strong (F2-F3), less than 1% violent (F4) and zero F5-rated tornado occurrences (Schultz and Cecil 2009). Even though TC tornadoes are typically weak and result in a small fraction of TC damage, issuing warnings for TC tornadoes remains an important

challenge. Tornadic and nontornadic TC supercells often occur in proximity, ruling out the use of large environmental differences to aid in the decision-making process (Spratt et al. 1997).

Tornadic TC environments have lower CAPE values and greater deep-tropospheric moisture than midlatitude tornadic environments (Edwards 2012). Aligning with the previous discussion, most tornadoes are produced in the northeast sector of TCs where larger amounts of CAPE, 0-1 km SRH, and 0-6 km bulk shear are located (McCaul 1991; Davies 2006). Schulz and Cecil (2009) found that an estimated 80% of tornadoes occur in this sector (between 350 and 120 degrees relative to TC motion; Figure 2.3). Landfalls bordering the Gulf of Mexico have also been observed to produce more tornadoes than those along the Atlantic coast as a result of the northeast sector's more prominent exposure to land (McCaul 1991). Past studies have indicated that many of the same parameters used to distinguish between midlatitude tornadic and nontornadic supercells also have utility in TC cases (Davies 1990). However, there is little distinction in environmental parameters between weak (EF0-EF1) and strong (EF2-EF3) tornadic TC environments (Edwards 2012). Similar low-level thermodynamic characteristics between TC cases also decreases the utility of parameters such as LFC, LCL height, and 0-3 km CAPE in distinguishing between tornadic and non-tornadic TC environments (Davies 2006). Environmental interactions with features such as low-level boundaries and mid-level dry-air intrusions must also be considered when assessing tornadic potential (Schultz and Cecil 2009; Edwards 2012; Fritz and Wang 2013).

The number of tornadoes spawned by TCs increases with cyclone size, intensity, and TC motion moving northward and northeastward with a speed of at least 5 m s^{-1} (McCaul

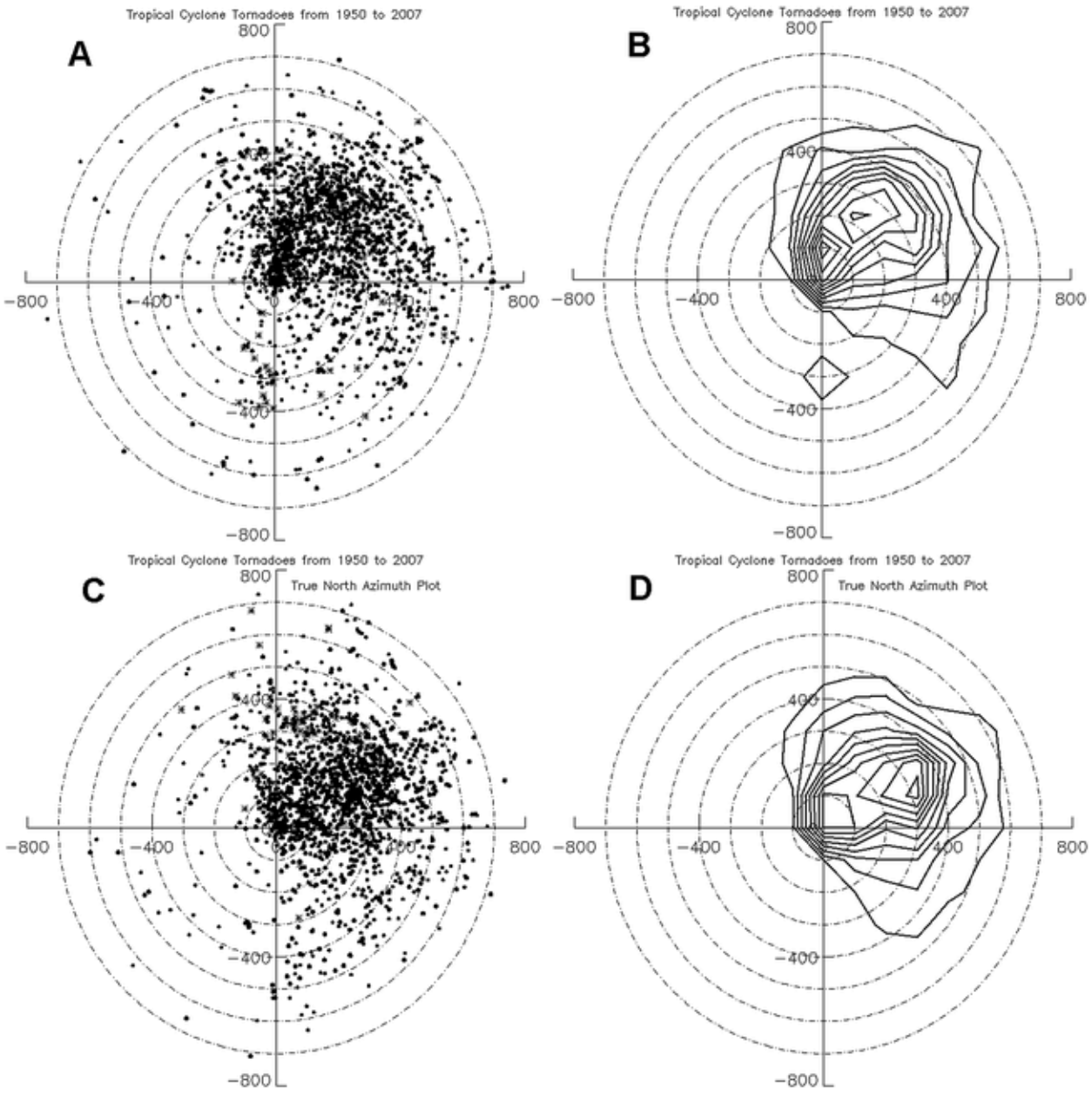

Figure 2.3: Tropical cyclone tornado locations (1950-2007) with 100 km increment range rings. Tornado location relative to the TC motion vector (a), 2D histogram of tornado locations relative to the TC motion vector (100 km x 100 km bin spacing) with ten tornado per grid box contour interval (b), and their locations relative to true north (c-d). [Figure 2 from Schultz and Cecil (2009)]

1991, Schultz and Cecil 2009). TC tornadoes are most common near the time of landfall, with an estimated 75% of tornadoes near the core occurring between 12 hours before and 24 hours after landfall (Schultz and Cecil 2009). However, it is possible for TC tornadoes to develop several days after landfall if favorable wind shear profiles are maintained (McCaul 1991). Occurrences of TC tornadoes are also dependent on distance from the coastline with rapidly decreasing instances within the first 150 km inland, yet this does not appear to have a relationship to tornado strength (Schultz and Cecil 2009). Frictional effects from the water-to-land transition increase low-level wind shear and convergence, causing an increase in tornado production along the coast as 60% of tornadoes occur within 100 km of the coast (Novlan and Grey 1974; Gentry 1983; McCaul and Weisman 1996; Schultz and Cecil 2009). A peak in TC tornadoes occurs in the late afternoon (1400-1700 LST), which is slightly earlier than the overall U.S. peak (1600-1800 LST) (Schultz and Cecil 2009). This diurnal bias is much stronger for tornadoes farther from the core of the TC as the environment is temporally steady towards the core. TC tornadoes near the core experience a more relaxed diurnal bias and are relatively weak (Schultz and Cecil 2009).

2.2 Dual-Polarization Radars and Supercell Dual-Polarization Signatures

a. Dual-Polarization Radars

Radars send out pulses of electromagnetic energy which are scattered by objects in the atmosphere and partially returned to the radar. Dual-polarization (dual-pol) radars are different than conventional radars as they transmit and receive pulses in two orthogonal orientations: the horizontal and the vertical. The inclusion of two orientations provides better insight into the characteristics of scatterers in the sample volume. The Joint

Polarization Experiment (JPOLE) was conducted in 2002-2003 to examine the utility of a dual-pol WSR-88D. This experiment found great operational utility with improvements in precipitation estimation, hydrometeor classification, and additional operational benefits (Scharfenberg et al. 2005). All 160 WSR-88D radars in the NEXRAD network were upgraded to include dual-pol capabilities between 2011 and 2013.

The upgrade to dual-pol capability came with additional radar products, including correlation coefficient (ρ_{hv}), differential reflectivity (Z_{DR}) differential phase shift (Φ_{DP}), and specific differential phase (K_{DP}). These additional products provide insight into the microphysical processes occurring in a sample volume. Correlation coefficient (ρ_{hv}) measures the diversity of scatterers present in a sample volume by calculating the correlation between the received horizontal and vertical polarizations. This variable helps to identify tornadic debris, large hail, the melting layer, and distinguish between meteorological and non-meteorological scatterers (Kumjian 2013). Higher values of ρ_{hv} indicate scatterers with a more consistent shape and size, such as uniform raindrops. Lower values of ρ_{hv} indicate that different shapes, sizes, phases, and/or orientation of scatterers are present. Low values of ρ_{hv} can also aid in the identification of tornadic debris (Ryzhkov et al. 2005; Van Den Broeke and Jauernic 2014).

Differential reflectivity (Z_{DR}) is the logarithmic ratio between the received horizontally versus vertically polarized reflectivity and can give insight into the shape of scatterers in a sample volume (Seliga and Bringi 1976). Spherical drops have Z_{DR} values near zero, given that their horizontal and vertical diameters are nearly equivalent. Hail typically has a spherical average shape, meaning its Z_{DR} value is near zero. Negative Z_{DR} values are typically associated with ice crystals or surface debris while positive Z_{DR}

values are associated with more oblate scatterers. Raindrops become more oblate as they grow, giving larger raindrops higher positive Z_{DR} values.

Differential phase shift (Φ_{DP}) measures the phase shift between the received horizontally- and vertically- polarized pulses. This product can give insight into the concentration and shape of droplets in a sample volume. As a pulse travels through a scatterer, it will attenuate and slow down, causing a shift in the phase. As the horizontally and vertically polarized pulses travel through the sample volume, they will encounter different media and therefore different phase shifts. However, Φ_{DP} accumulates the phase shift down the entire radial. If the beam encounters an area with a high concentration of large raindrops, high Φ_{DP} values will be present throughout the rest of the radial. Therefore, the derived product specific differential phase (K_{DP}) is preferred as it shows the change (range derivative) in Φ_{DP}. Positive values of K_{DP} can be seen in areas with large droplets as the horizontally polarized beam passes through more areas of the oblate liquid drops than the vertically polarized beam. K_{DP} is useful for both hydrometeor classification and rainfall rate estimation (Zrnić and Ryzhkov 1999; Liu and Chandrasekar 2000; Brandes et al. 2001).

b. Supercell Dual-Polarization Signatures

Dual-polarization signatures provide insight into the structure and microphysical processes occurring in supercell thunderstorms. Repeatable dual-pol signatures in supercells include the Z_{DR} column (e.g., Caylor and Illingworth 1987; Conway and Zrnić 1993; Kumjian and Ryzhkov 2008; Kumjian et al. 2014), the Z_{DR} arc (e.g., Ryzhkov et al. 2005; Kumjian and Ryzhkov 2007, 2008), the K_{DP} foot (e.g., Romine et al. 2008; Crowe et al. 2010, 2012), the separation distance and angle between the Z_{DR} arc and K_{DP} foot

(e.g., Crowe et al. 2010, 2012; Loeffler and Kumjian 2018), and hailfall signatures (Van Den Broeke 2020). Prior research has investigated the relationship these signatures have with the supercell environment, mesocyclone strength, and tornadic potential.

A Z_{DR} column encompasses a region of enhanced positive Z_{DR} values collocated with the updraft in a deep convective storm (Herzegh and Jameson 1992; Kumjian and Ryzhkov 2008; Kumjian et al. 2014; Van Den Broeke 2016). These columns are relatively narrow (4-8 km wide) and can be more than 3 kilometers deep in the mid- and upper levels of a supercell (Kumjian and Ryzhkov 2008; Kumjian et al. 2014). This enhancement in Z_{DR} is due to a region of liquid drops and water coated hailstones that have been lofted above the 0°C level by the updraft. The Z_{DR} column can be used to infer updraft strength and size (Kumjian et al. 2014; Van Den Broeke 2016; Van Den Broeke 2020). Environmental thermodynamic characteristics play a role in Z_{DR} column size and depth, and thus presumably also to the updraft size and vertical velocity, as they have shown correlation to LCL temperature, CAPE, midlevel relative humidity, and SRH (Van Den Broeke 2016). Temporal variation of Z_{DR} column may provide insight into whether a supercell is intensifying or decaying (Hubbert et al. 1998; Kumjian and Ryzhkov 2008; Kumjian et al. 2010). Previous studies with small sample sizes show potential that Z_{DR} columns can help to distinguish between tornadic and nontornadic supercells since tornadic storms tend to have larger Z_{DR} columns and less variability in size 25-30 minutes prior to tornadogenesis (Sessa and Trapp 2020; Van Den Broeke 2017; Van Den Broeke 2020).

The Z_{DR} arc is a region of enhanced Z_{DR} values along the forward flank of a supercell (Figure 2.4) (Kumjian and Ryzhkov 2008; Dawson et al. 2014). This shallow

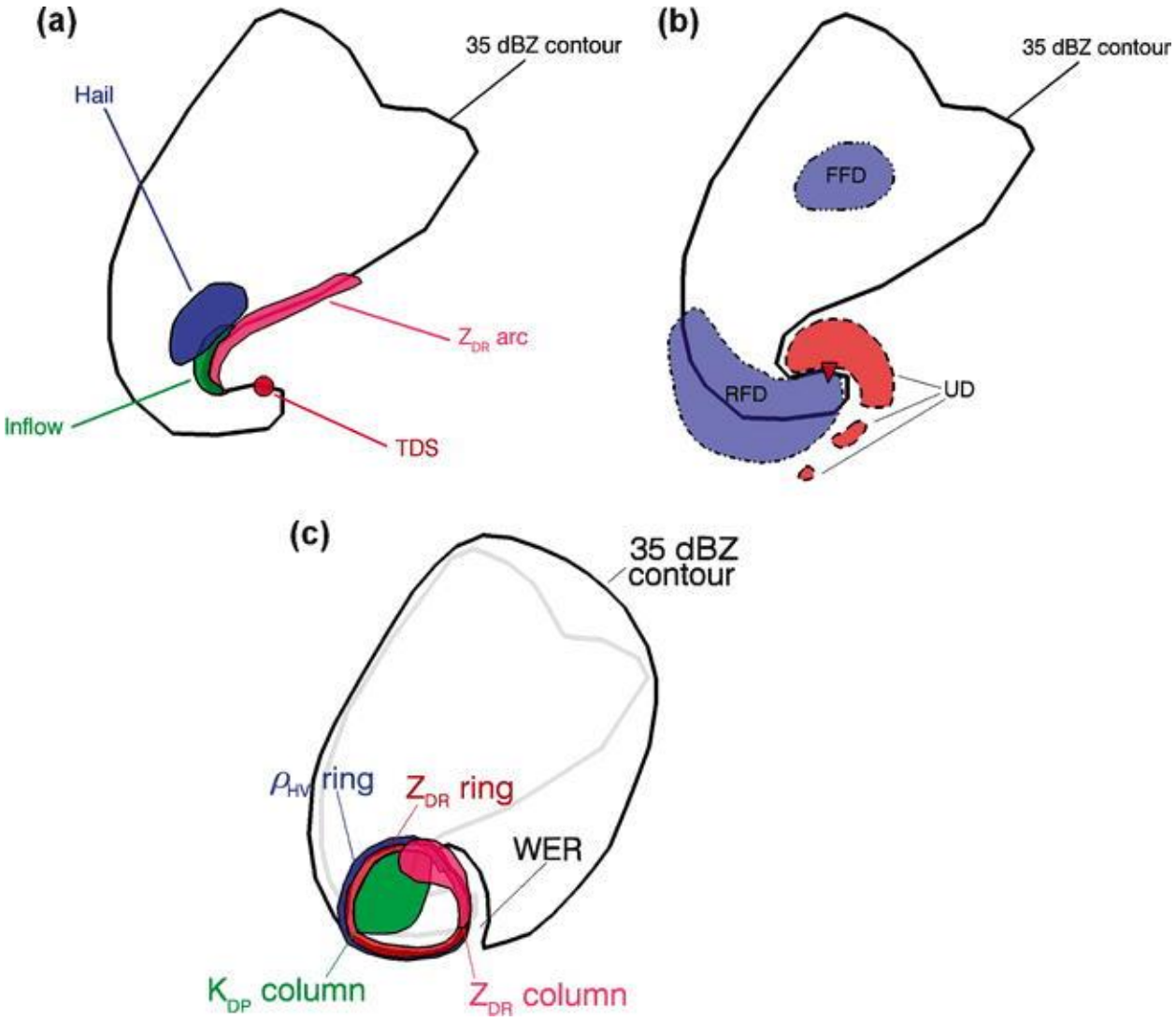

Figure 2.4: Schematic showing features of a supercell thunderstorm in (a) the low levels (<1 km), (b) regions of substantial vertical velocity, (c) midlevels (~5 km). Features include the tornadic debris signatures (TDS), Z_{DR} arc, low-level hail signature, low-level inflow, and the weak-echo region ("WER"). [Figure 1 from Kumjian and Ryzhkov (2008)]

signature is typically 1-2 km in depth with values over 2 dB but may exceed 4-5 dB (Kumjian and Ryzhkov 2008, 2009). Z_{DR} arcs contrast with Z_{DR} columns as arcs are shallow and elongated. Wind speeds increase and veer with height in right-moving supercells, allowing a size-sorting process that removes small drops from this region, leaving behind a collection of large, sparse drops (Kumjian and Ryzhkov 2007).

The Z_{DR} arc may give insight into the strength and lifecycle of a supercell. Previous work found a positive correlation between the Z_{DR} arc magnitude and SRH (Kumjian and Ryzhkov 2008, 2009). Low-level storm-relative inflow is the most important wind variable that relates to this size sorting process (Dawson et al. 2015). Z_{DR} arc magnitude was also shown to have a positive correlation with environmental variables such as low-level bulk shear, midlevel relative humidity, and the LFC height with a small sample size of cases (Van Den Broeke 2016). Cyclic patterns in the Z_{DR} arc have been observed in which the arc curvature increases as the mesocyclone organizes and tornadogenesis takes place only to decrease during the decay of the tornado and reorganization of the mesocyclone (Kumjian et al 2010; Palmer et al. 2011). Previous studies have also shown promise that Z_{DR} arc magnitude and orientation can help differentiate tornadic and nontornadic supercells as tornadic storms tend to have increased magnitude and curvature (Ryzhkov et al. 2005; Palmer et al. 2011; Crowe et al. 2012). Previous work using a small midlatitude storm sample found larger mean Z_{DR} arc values and a larger areal extent of the 3.5-dB Z_{DR} arc in tornadic supercells than nontornadic supercells, however no discernable differences were found between pretornadic and nontornadic supercells (Van Den Broeke 2017; Wilson and Van Den Broeke 2021).

The K_{DP} foot refers to an elongated maximum in K_{DP} values in the low levels of a supercell's forward flank (Romine et al. 2008). These enhanced values indicate a large liquid water content, typically from copious amounts of small raindrops or melting hail. Another useful parameter, the separation angle between the Z_{DR} arc and K_{DP} maximum, gives insight into active size sorting processes and mesocyclone strength (Crowe et al. 2010). This separation angle (Figure 2.5) is found by identifying a centroid for both the K_{DP} foot and Z_{DR} arc, followed by the calculation of a separation vector between the two centroids and the clockwise angle of the storm motion vector (Loeffler and Kumjian 2018).

Previous studies found that separation-vector direction and distance between the Z_{DR} arc and K_{DP} foot increases with mesocyclone strength as the separation between these features can add insight into the low-level wind shear within the supercell (Crowe et al. 2010). Increased separation implies stronger low-level wind shear that advects the smaller drops seen in the K_{DP} foot farther away from the updraft, leaving more separation between larger drops in the Z_{DR} arc and smaller drops in the K_{DP} foot. Tornadic supercells have also been observed to have a larger separation between these signatures than nontornadic supercells (Crowe et al. 2012). In tornadic cases, the Z_{DR} arc shifts towards the inflow of the supercell while the K_{DP} foot moves farther into the left side of the forward flank (Martinaitis 2017; Loeffler et al. 2020). In opposition, in nontornadic cases the Z_{DR} arc shifts towards the rear of the storm, near the updraft, while the K_{DP} foot shifts farther forward in the forward flank (Crowe et al. 2012).

Dual-pol variables can help detect regions with hailfall. Hail tends to be very reflective, so its reflectivity values often reach 55 dBZ, especially if the hail is water-

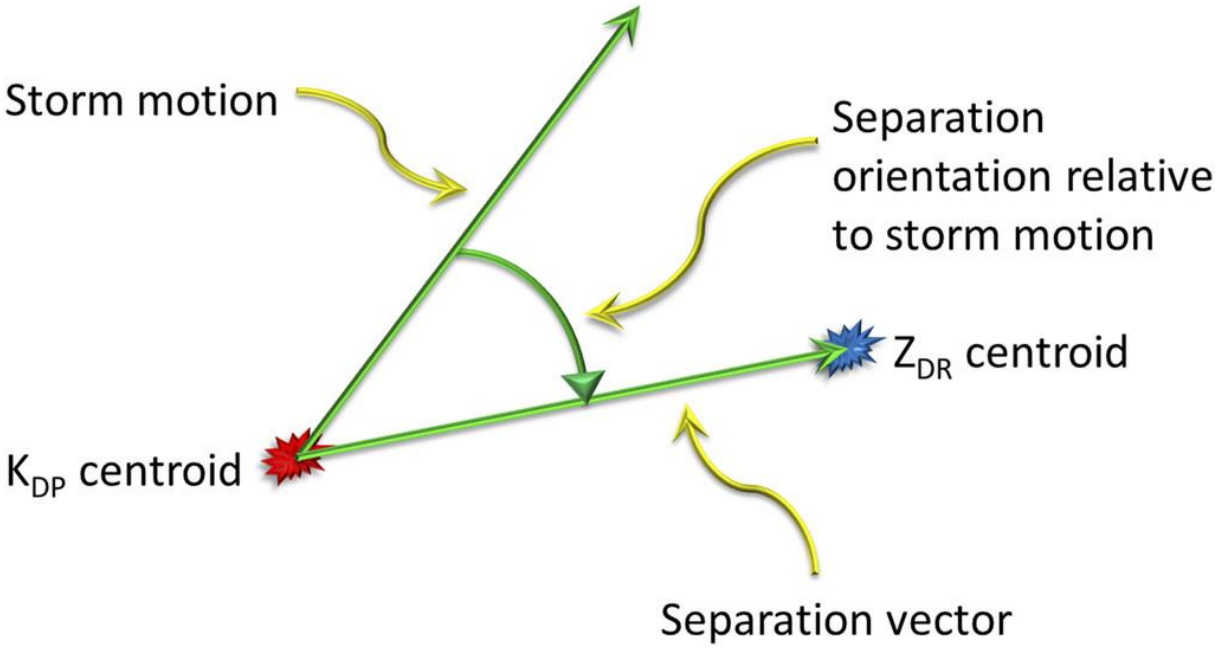

Figure 2.5: Schematic showing the separation vector between the Z_{DR} arc and K_{DP} foot. Defined as the distance between the Z_{DR} and K_{DP} centroids and the clockwise angle from the storm motion vector. [Figure 4 from Loeffler and Kumjian (2018)]

coated. Although hail comes in different shapes and sizes, it tumbles as it falls, appearing spherical to the radar and producing Z_{DR} values near zero. Due to hail often falling with raindrops, ρ_{hv} values are low and typically between 0.7 and 0.95. A hailfall region can often be found in the forward flank of a supercell, downshear from the mesocyclone (Van Den Broeke et al. 2008; Van Den Broeke 2016). The areal extent of the hailfall region can also be related to the periodicity of the storm with more prominent cycling of hailfall area in tornadic cases (Van Den Broeke 2016). Van Den Broeke (2020) also found that the hailfall region was typically larger and steadier in nontornadic storms than in pretornadic storms.

c. Tropical Cyclone Supercell Dual-Polarization Signatures

Relatively little work has been done to describe the polarimetric characteristics of TC supercells, with most studies using a case study approach. A more detailed examination is needed to determine if it will be possible to improve forecasting abilities and decrease false alarm ratios (FAR). A statistical analysis of tornado warnings in tropical cyclones revealed an above average FAR rate (NWS 2012). The high shear and high moisture environments in TCs allow for rapid tornadogenesis with subtle radar features, requiring a high skill level to accurately detect (Schneider and Sharp 2007; Martinaitis 2017). A better understanding of polarimetric characteristics in these storms is expected to improve operational performance.

The miniature size of TC supercells makes them difficult to sample with radar resolutions (Spratt and Nash 1995). When compared to midlatitude supercells, TC supercell features appear much subtler but are still identifiable in most cases. Features such as hooks, appendages, and BWERs become less identifiable at greater range

(Devanas et al. 2008). Thus, the appearance of these features adds an extra degree of confidence when making warning decisions. Rotational signatures are shallower in TC supercells (average depth 3.5 km) and appear more compact than midlatitude supercells, however the ratio of depth to storm top is comparable between the two (Spratt et al. 1997). These rotational differences make it difficult for current mesocyclone detection algorithms implemented in the WSR-88D to reliably identify TC supercells. In some cases, cyclic behavior may also be observed in TC supercells as the mesocyclone grows and collapses (Spratt et al. 1997).

An analysis of the polarimetric variables in three tornado-warned supercells in Hurricane Rita (2005) was conducted by Crowe et al. (2010). Of the three tornado-warned supercells examined: one was tornadic, one produced only a funnel cloud, and one produced neither a tornado nor a funnel cloud. Similar to their midlatitude counterparts, a larger separation of the Z_{DR} and K_{DP} maxima was observed at 1 km above ground level (AGL) in the tornadic case (Figure 2.6). In the tornadic case, the Z_{DR} maximum shifted downshear from the mesocyclone in the forward flank while the K_{DP} maximum was located in the right-rear quadrant. As seen in midlatitude supercells, this increased separation indicates a stronger size sorting process as mesocyclone strength increases (Kumjian and Ryzhkov 2008). The tornadic case also had more variation in the horizontal reflectivity (Z_H) than the nontornadic cases. An increase in the low-level Z_H was only observed in the tornadic case as the updraft began to collapse.

Martinaitis (2017) analyzed tornado-warned supercells in tropical storms Debby (2012) and Andrea (2013) to investigate precursors for tornadic events. The study realized different potential tornadic indicators dependent on the storms' distance from the

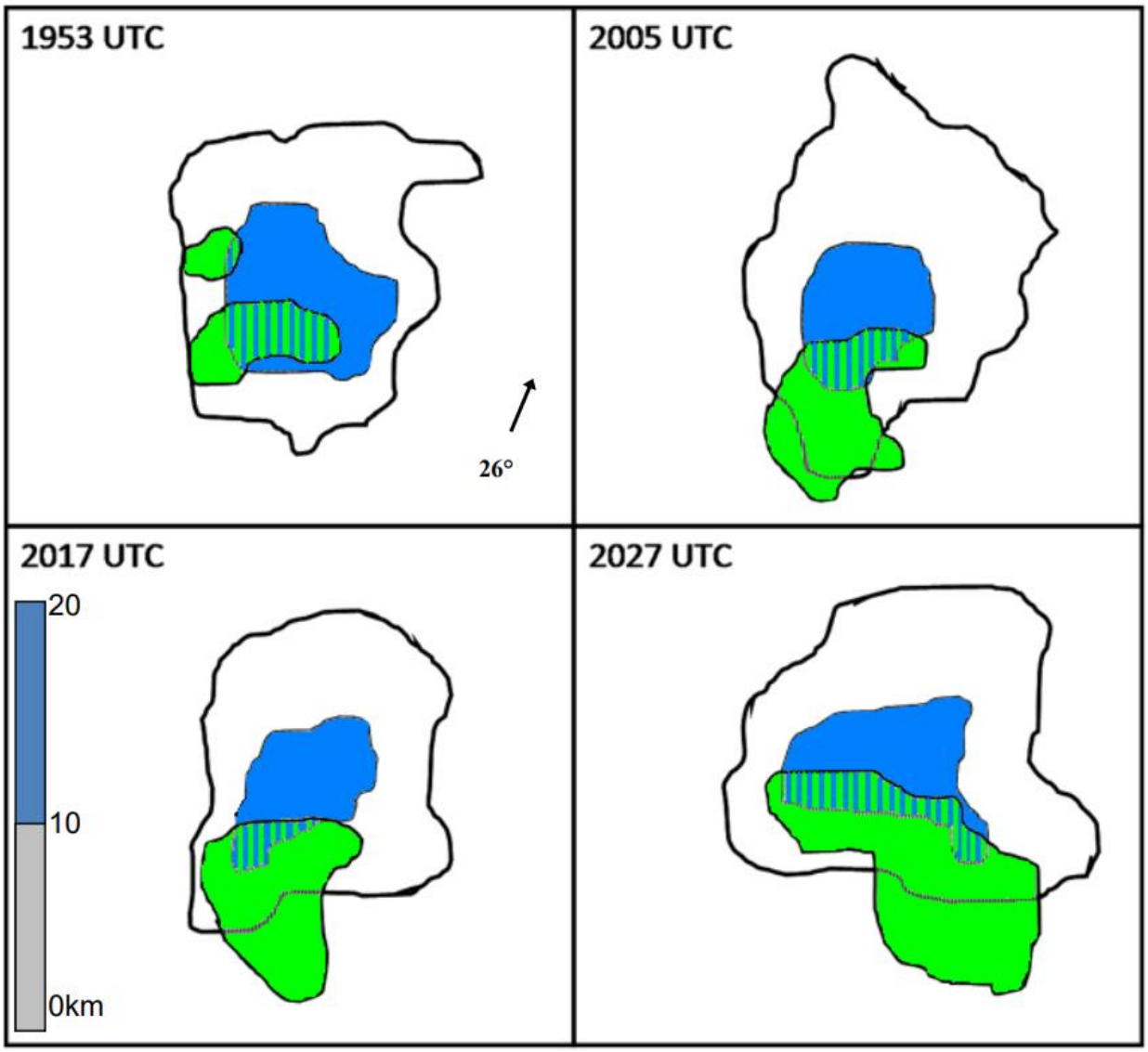

Figure 2.6: Time series of a tornadic supercell in Hurricane Rita (2005) at 1953 UTC (top left), 2005 UTC (top right), 2017 UTC (bottom left), and 2027 UTC (bottom right) at 1 km AGL. The storm motion vector is indicated by the black arrow. The length scale (km) is displayed on the bottom left. The thick black line is the 30 dBZ reflectivity contour, green shading indicates Z_{DR} values greater than 3 dB, and blue shading indicates K_{DP} values greater than 1.5° km^{-1}. [Figure 7 from Crowe et al. (2010)]

radar. In cases when the cell is within 74.1 km from the nearest radar, a hook echo should be observed in the reflectivity field and separation should exist between the Z_{DR} and K_{DP} maxima. Cases closer to a radar should also observe a contracting velocity signature with rotational velocity values $\geq$ 10.3 m s^{-1}. When a cell is observed between 74.1 and 129.6 km from the nearest radar, a characteristic supercell reflectivity signature may not be observed. Rotational velocity values $\geq$ 7.7 m s^{-1} are required at the 0.5° elevation angle.

Observations of rotational characteristics in the mid-levels of TC supercells are sparse. Schneider and Sharp (2007) rarely observed a mesocyclone above the 1.5° elevation angle; only the presence of broad rotation (at least 5.5 km separation between inbound and outbound velocities) was identified. Collocation of an enhanced midlevel radial velocity (at least 15.4 m s^{-1}) with a low-level rotational signature and hook echo was found in 14 of the 15 cases investigated. This velocity enhancement was typically observed between 2.1 and 4.2 km AGL and could potentially indicate tornadic development (Schneider and Sharp 2007). Previous work indicates promise that polarimetric characteristics can help distinguish between the tornadic and nontornadic supercells. Established similarities between TC and midlatitude supercells may further improve operational performance.

2.3 Hypotheses

Examining differences in dual-polarimetric signatures may provide valuable insight into size sorting processes occurring in TC supercells. Investigating differences between TC and midlatitude supercell dual-polarimetric signatures in a large number of cases can be a valuable tool for gauging insight into these processes. In turn, investigating dual-polarimetric signatures between tornadic and nontornadic TC supercells may

provide improved capabilities for nowcasting scenarios. Z_{DR} columns are dependent on the environmental freezing level, as they encompass a region of positive Z_{DR} values from liquid droplets or water coated ice particles being lofted above the environmental freezing level (Kumjian et al. 2014; Snyder et al. 2015; Wilson and Van Den Broeke 2022). TC environments typically have higher environmental freezing levels (McCaul 1991; Davies 2006) and a smaller vertical extent than midlatitude supercells (Spratt et al. 1997; Schneider and Sharp 2007; Edwards 2012). Z_{DR} column area and depth also have a positive correlation with both MLCAPE and MUCAPE (Wilson and Van Den Broeke 2022) as values of these variables are typically reduced in TC environments (McCaul 1991). Therefore, it is hypothesized that TC supercells will have smaller and shallower Z_{DR} columns than midlatitude supercells from a combination of the shallower updrafts and higher environmental freezing levels. Due to tornadic and nontornadic TC supercells often being in close proximity (Spratt et al. 1997; Schultz and Cecil 2009), it is hypothesized that Z_{DR} column area and depth will behave similarly between tornadic and nontornadic TC supercells as environmental differences are small.

Although TC mesocyclones are typically shallower and weaker than midlatitude cases (Spratt et al. 1997; Schneider and Sharp 2007), tornadic TC supercells have been shown to have stronger mesocyclones than nontornadic TC supercells (Schneider and Sharp 2007; Martinaitis 2017). Stronger mesocyclone in tornadic TC supercells may results from several mechanisms related to tornado production in landfalling TCs, such as increased convergence and low-level wind shear from the water-to-land transition or interactions with baroclinic boundaries (Novland and Grey 1974; Gentry 1983; McCaul and Weisman 1996). These effects can increase the vertical vorticity, therefore enhancing

the low-level mesocyclone. A stronger low-level mesocyclone will have an increased upward dynamic perturbation pressure gradient that can contribute to the stretching of vertical vorticity near the surface needed for tornadogenesis (Davies-Jones 1984; Markowski and Richardson 2014; Davies-Jones 2015; Yokota et al. 2018). It is hypothesized that tornadic TC supercells will have stronger mesocyclones as measured using rotational velocity than nontornadic cases.

Low-level wind shear in supercells is responsible for the size sorting process that removes smaller scatterers with smaller terminal velocities and allows large scatterers, and therefore higher Z_{DR} values, to remain in the Z_{DR} arc along the inflow edge of the FFD (Browning 1965; Conway and Zrnić 1993). Coincidentally, it has been found that an increase in low-level wind shear, and therefore an increase in the low-level storm relative inflow, may promote more effective size sorting (Dawson et al. 2014). The increased low-level wind shear in TC environments compared to midlatitude supercell environments leads to the hypothesis that Z_{DR} arcs will remain steady and pronounced in TC supercells (McCaul 1991; Nowotarski et al. 2021).

Strong low-level wind shear can increase the separation distance and angle between the K_{DP} foot and Z_{DR} arc as the smaller drops in the K_{DP} foot are advected farther away from the updraft (Crowe et al 2012; Loeffler and Kumjian 2018). Once again, the increased low-level wind shear in TC environments (McCaul 1991) should create a larger separation between these two signatures compared to midlatitude supercells. It is hypothesized that there will be an increase in both the separation angle and normalized separation distance between the K_{DP} foot and Z_{DR} arc in TC supercells when compared to midlatitude supercells. Both Crowe et al. (2012) and Martinaitis

(2017) observed a larger separation in tornadic than nontornadic TC supercells as increased mesocyclone strength and low-level wind shear in tornadic cases shifted the Z_{DR} arc towards the inflow of the supercell and the K_{DP} foot moved farther into the downdraft. Therefore, it is also hypothesized that greater separation will be present between tornadic and nontornadic TC supercells.

Wilson and Van Den Broeke (2022) found a moderate negative correlation between the environmental freezing level height and hailfall area. The larger freezing level heights in addition to the shallower updrafts expected in TC supercells will make the production of hail sparse (McCaul 1991; Spratt et al. 1997; Davies 2006; Edwards 2012). In cases when hail is produced, the increased deeper tropospheric moisture and decreased lapse rates in TC environments will make it difficult for hail to survive to the base scan (Baker et al. 2009; Crowe et al. 2010; Edwards 2012). Accordingly, it is hypothesized that relatively little, if any, hailfall will survive to base scan in TC supercells.

Establishing differences between TC and midlatitude dual-polarimetric signatures can give insight into the similarities and differences in the size sorting processes occurring in these storms. Additional emphasis will be placed on the differences in dual-polarimetric signatures in the 30 minutes prior to tornadogenesis versus the 30 minutes prior to maximum normalized rotational velocity (NROT) in nontornadic TC supercells. Establishing differences that may support or refute these hypotheses can be beneficial for operational meteorologists in order to better understand the kinematic environment in the low-levels of a supercell as well as possible indicators of tornadic potential.

Chapter III: Data and Methodology

3.1 Tropical Cyclone Supercell Identification

In this study, tornadic and nontornadic samples of tropical and extratropical supercells are compared. In order to create a large dataset of supercells associated with tropical cyclones, a manual analysis was performed to find times with convection associated with a tropical cyclone within 100 km of a WSR-88D radar after the dual-polarization upgrade. The manual analysis was conducted through the 2021 tropical cyclone season. Convection was required to be within 300 km of the coast and during the first 48 hours following landfall to be included. Fifty-seven periods were identified to be examined (Table 3.1).

Once the convective time periods were identified, a mesocyclone detection algorithm (MDA) was used to identify supercells within the convection (Stumpf et al. 1998). The MDA was designed as part of the Warning Decision Support System – Integrated Information (WDSS-II), a packet of severe weather analysis algorithms developed by the National Severe Storms Laboratory (NSSL) and the Cooperative Institute for Severe and High-Impact Weather Research and Operations (CIWRO) at the University of Oklahoma. A modified version of this NSSL MDA was used for this project. The algorithm allows for the input of a specific radar location and time to gather four-dimensional radial velocity data. The algorithm begins at the one-dimensional level where cyclonic azimuthal shear segments are identified. These shear segments then form horizontal associations in order to form two-dimensional features followed by vertical associations to form three-dimensional features. The fourth-dimensional level is then completed with associations tracked in time (Stumpf et al. 1998). The MDA includes tunable parameters

Analysis Period #	Date(s)	Storm	Radar	Analysis Period (UTC)
1	27 August 2011	Irene	KMHX	0000-1000
2	27 May 2012	Beryl	KJAX	1630-2200
3	28 May 2012	Beryl	KCAE	1430-2300
4	24-25 June 2012	Debby	KTBW	1900-0300
5	25 June 2012	Debby	KJAX	0630-1500
6	6 June 2013	Andrea	KAMX	1000-1300
7	6 June 2013	Andrea	KTBW	1430-1600
8	6 June 2013	Andrea	KJAX	2000-2230
9	7 June 2013	Andrea	KLTX	0500-1300
10	7 June 2013	Andrea	KMHX	0630-1200
11	3 July 2014	Arthur	KCLX	0600-0800
12	3 July 2014	Arthur	KLTX	0900-2130
13	3 July 2014	Arthur	KMHX	1730-0000
14	4 July 2014	Arthur	KAKQ	0400-0900
15	8 May 2015	Ana	KMHX	1500-2200
16	10 May 2015	Ana	KAKQ	1700-2000
17	16 June 2015	Bill	KHGX	1130-1930
18	31 May 2016	Bonnie	KLTX	1300-2100
19	31 May-1 June 2016	Bonnie	KMHX	1600-1500
20	7 October 2016	Matthew	KJAX	0100-1200
21	8 October 2016	Matthew	KLTX	1030-1430
22	8 October 2016	Matthew	KMHX	1500-2130
23	21 June 2017	Cindy	KLIX	0500-1430
24	22 June 2017	Cindy	KLCH	0930-1430
25	25 August 2017	Harvey	KCRP	0400-0800
26	25-26 August 2017	Harvey	KHGX	0800-1200
27	9-10 September 2017	Irma	KAMX	1500-1230
28	7 October 2017	Nate	KMOB	1800-2330
29	28 May 2018	Alberto	KTLH	0500-2000
30	28 May 2018	Alberto	KMXX	1730-2030
31	10 October 2018	Michael	KTLH	0700-1000
32	10 October 2018	Michael	KJGX	1730-2130
33	13 July 2019	Barry	KSHV	1900-2300
34	5 September 2019	Dorian	KLTX	0630-1230
35	5 September 2019	Dorian	KMHX	1230-2130
36	17-28 September 2019	Imelda	KHGX	2330-0700
37	27 May 2020	Bertha	KMHX	1745-1845
38	7 June 2020	Cristobal	KMOB	1030-1400
39	25 July 2020	Hanna	KCRP	0700-1400
40	25 July 2020	Hanna	KHGX	1500-2300
41	2 August 2020	Isaias	KMLB	1100-1700
42	2 August 2020	Isaias	KJAX	1500-2200
43	4 August 2020	Isaias	KMHX	0000-0630

44	16 September 2020	Sally	KEVX	0800-1030
45	21-22 September 2020	Beta	KHGX	1430-0700
46	10 October 2020	Delta	KGWX	1600-2200
47	28-29 October 2020	Zeta	KMOB	2230-0200
48	9 November 2020	Eta	KAMX	0530-1100
49	19 June 2021	Claudette	KLIX	0500-1500
50	19 June 2021	Claudette	KBMX	1420-1600
51	28 June 2021	Danny	KCLX	2200-2330
52	7 July 2021	Elsa	KTBW	0230-1100
53	7 July 2021	Elsa	KJAX	1800-2330
54	16 August 2021	Fred	KLTH	1600-1800
55	29-30 August 2021	Ida	KLIX	2130-0100
56	8 September 2021	Mindy	KLTH	1830-2200
57	13 September 2021	Nicholas	KHGX	2200-0000

Table 3.1: Manually constructed time periods of tropical cyclone convection in close proximity to a WSR-88D radar after the dual-polarimetric upgrade through the 2021 tropical cyclone season.

to adjust the sensitivity of mesocyclone detections while also removing false detections from non-meteorological scatterers such as ground clutter. The modified version of this MDA creates tunable rank thresholds with these azimuthal shear values in order to find locations of azimuthal shear maxima. These locations are then cross-examined for vortex signatures. These thresholds allow for a balance between removing false detection from non-mesocyclone phenomena while ensuring that some of the smaller mesocyclones from tropical cyclone supercells will not go undetected.

The modified NSSL MDA was applied to each time period identified during the manual analysis to detect the presence of tropical cyclone supercells in a consistent and repeatable fashion. The detections from the MDA were then cross-examined with radar data in the National Oceanic and Atmospheric Administration's (NOAA) Weather and Climate Toolkit (WCT), an independent software produced by NOAA's National Center for Environmental Information (NCEI) that allows for the visualization of weather and climate data including archived radar data. Time series of longitude and latitude produced by the MDA for each detection were plotted in WCT to ensure that detections contain characteristic radar signatures of supercells as described by Thompson et al. (2003). All false detections were discarded from the dataset. Detections associated with supercells were also required to be within 100 km of a WSR-88D radar over at least four successive base scans to improve the estimates of low-level radar metrics such as the Z_{DR} arc. Supercells that met the aforementioned criteria that became undetected at some point in their lifetime only to return as a detectable supercell later in time are counted as the same supercell. Detected supercells must also be over land as supercells over the ocean may be

tornadic with no official tornado report. A total of 216 supercells meeting all of these criteria make up the tropical cyclone supercell dataset used in this study (Table 3.2).

The supercells were then categorized as tornadic or nontornadic based on tornado reports from the NCEI Storm Events Database (https://www.ncdc.noaa.gov/stormevents/). Tornado reports from this database contain an approximate start and end time, latitude, longitude, and rating. Additional information is also provided on damage and detection details. Start and end longitude and latitude for tornado reports were plotted in WCT to find associated supercells from the tropical cyclone supercell dataset. This analysis identified twenty-four tornadic supercells, four of which produced multiple tornadoes (Table 3.3). The tornado reports included eighteen EF0 tornadoes, twelve EF1 tornadoes, and one EF2 tornado (Table 3.3). It should be noted that while the Storm Events Database is the most accurate archive for severe weather reports, it is possible that a nontornadic supercell was actually tornadic during its lifetime and missing an official report. This is possible in several scenarios including tornadoes that lack an official spotter report, cause little to no damage, occur in conditions where visibility may be lacking, and/or are embedded in strong straight-line winds.

The midlatitude dataset contains 206 supercells occurring between 2012 and 2020. This dataset includes 103 tornadic and 103 nontornadic supercells and was obtained from Wilson and Van Den Broeke (2022). Supercells in this dataset must include typical supercell reflectivity structures, a midlevel mesocyclone maintained for at least 30 minutes, and at least four successive radar scans with the forward flank region sampled < 1 km above radar level (ARL).

Analy-sis Period Origin #	MDA Detected Supercell Period (UTC)	Start Lat.	Start Long.	Analy-sis Period Origin #	MDA Detected Supercell Period (UTC)	Start Lat.	Start Long.
1	0001-0034	-76.484	34.234	26	0045-0143	-94.945	28.827
1	0001-0025	-76.917	34.252	26	0057-0207	-94.903	28.872
1	0001-0029	-76.777	34.324	26	0317-0401	-94.903	28.944
1	0015-0116	-76.340	34.203	26	0317-0619	-94.668	28.688
1	0015-0057	-76.124	34.198	26	0509-0724	-94.921	29.047
1	0034-0153	-75.859	34.243	27	1922-2023	-79.592	25.825
1	0048-0217	-75.721	35.316	27	1935-2037	-79.418	25.861
1	0053-0125	-75.974	35.330	27	2010-2111	-79.279	25.583
1	0107-0130	-75.739	35.146	27	2139-2246	-79.478	25.924
1	0130-0207	-76.563	34.468	27	2246-2354	-79.922	26.072
1	0135-0245	-76.099	34.504	27	0732-0824	-79.556	25.722
1	0203-0259	-76.484	34.432	28	1841-1929	-87.580	30.183
1	0245-0322	-75.914	34.603	28	1857-2000	-87.604	30.264
1	0245-0313	-75.950	35.487	28	1857-2000	-88.728	29.995
1	0259-0341	-76.400	34.633	28	2011-2139	-88.205	30.201
1	0304-0327	-76.118	34.885	28	2127-2227	-87.838	30.394
1	0322-0409	-76.154	35.204	28	2227-2325	-87.652	30.466
1	0327-0409	-75.781	34.921	28	2227-2325	-87.363	30.026
1	0327-0442	-75.703	34.908	29	0514-0644	-83.757	29.650
2	2100-2137	-80.612	30.226	32	1849-2027	-83.682	32.199
4	1900-2031	-83.048	27.457	32	1926-2041	-83.525	32.923
4	1934-2031	-82.718	27.874	34	0632-0758	-77.962	33.393
4	1900-1957	-82.531	28.072	34	0653-0813	-77.746	33.322
4	1900-1934	-81.474	27.174	34	0706-0833	-77.806	33.335
4	1900-1934	-81.518	26.922	34	0739-0941	-77.584	33.483
4	1929-1952	-83.138	27.021	34	0813-0954	-77.620	33.766
4	1934-2026	-81.991	27.919	34	0805-0934	-78.726	33.717
4	1952-2139	-82.459	27.757	34	0839-1116	-77.602	33.762
4	1952-2139	-82.994	27.677	34	0854-1123	-77.427	33.753
4	2003-2100	-82.982	27.452	34	0913-1048	-77.367	33.820
4	2048-2238	-82.844	27.802	34	0941-1116	-77.457	33.946
4	2139-2238	-82.273	28.081	34	0934-1116	-77.980	33.474
4	2250-2324	-83.060	27.394	34	1014-1109	-77.499	34.121
4	2315-0026	-82.970	27.088	34	1041-1224	-77.457	34.233
4	2352-0049	-82.850	27.421	35	1231-1351	-77.067	34.610
5	0852-0949	-81.555	30.487	35	1237-1418	-76.965	34.606
5	1134-1334	-81.471	30.357	35	1237-1357	-77.145	34.350
5	1134-1340	-81.453	30.208	35	1651-1815	-77.192	34.143
5	1140-1334	-81.441	30.527	35	1710-1815	-76.880	34.049
5	1248-1334	-81.219	30.621	35	1730-1815	-76.484	34.004

5	1351-1431	-80.978	30.711	35	1737-1903	-76.394	33.959
5	1403-1431	-81.044	30.383	35	1755-1910	-76.868	35.221
6	1002-1124	-80.728	25.776	35	1822-1947	-76.886	34.076
6	1002-1124	-80.626	26.023	35	1903-2008	-76.189	34.341
6	1002-1056	-80.163	26.319	35	1849-1941	-77.073	34.045
6	1046-1157	-80.824	25.852	35	2026-2124	-76.983	34.458
6	1129-1201	-80.349	26.216	35	2054-2129	-76.977	35.086
7	1437-1557	-82.868	26.833	36	2335-0131	-95.414	29.474
7	1443-1538	-82.814	27.654	36	0046-0148	-95.528	29.263
7	1448-1557	-82.562	26.999	38	1033-1136	-87.862	29.963
7	1500-1557	-82.447	26.887	38	1038-1131	-87.830	30.004
9	0504-0618	-78.113	33.447	38	1110-1212	-87.568	30.017
9	0504-0541	-77.709	33.806	38	1121-1159	-87.538	30.170
9	0642-0747	-77.530	33.667	38	1159-1232	-87.562	30.305
9	0728-0756	-77.632	33.802	38	1159-1327	-88.427	29.927
9	0856-0928	-78.864	34.274	38	1239-1327	-87.381	30.267
9	0952-1029	-78.557	34.224	38	1232-1327	-87.532	30.156
10	0634-0735	-77.409	34.377	38	1239-1340	-87.970	29.923
10	0634-0716	-77.151	34.318	39	0702-0752	-96.778	27.860
10	0634-0904	-77.091	34.224	39	0901-1048	-96.657	27.887
10	0648-0803	-76.856	34.022	39	0942-1009	-96.916	27.972
10	0730-0854	-77.451	34.143	40	1737-1818	-95.504	29.173
10	0744-0845	-76.580	34.260	40	1755-1841	-95.522	28.930
10	0812-0946	-77.343	34.332	40	1829-1858	-96.173	29.317
10	0922-1013	-76.532	34.292	43	0033-0105	-77.457	34.063
10	0946-1114	-76.448	34.349	43	0143-0343	-76.580	33.968
12	1330-1415	-77.986	33.604	43	0156-0248	-77.169	33.959
12	1330-1421	-77.884	33.640	43	0156-0242	-77.313	33.973
12	1607-1655	-77.806	33.874	43	0337-0508	-76.279	34.031
12	1655-1741	-77.704	34.098	43	0356-0528	-76.321	34.287
12	1808-1900	-77.896	34.381	43	0402-0454	-76.562	34.848
12	1937-2013	-77.770	34.341	43	0515-0547	-77.097	35.028
13	2059-2153	-77.079	34.054	44	0811-0855	-86.347	29.975
13	2059-2153	-76.989	33.986	44	0811-1024	-86.227	29.737
13	2231-2304	-76.556	34.790	44	0800-0907	-85.266	30.042
14	0400-0523	-76.428	36.495	44	0849-0919	-86.215	29.893
14	0513-0549	-76.103	36.881	44	0907-1012	-86.311	30.253
14	0550-0646	-76.302	36.643	44	0855-0953	-85.542	30.074
15	1704-1739	-77.073	34.538	44	0930-1024	-82.206	29.934
17	1610-1655	-94.374	29.088	45	0019-0153	-88.972	34.153
17	1737-1806	-94.642	29.469	45	0135-0219	-88.731	33.933
20	0835-0928	-81.171	30.159	45	0213-0258	-88.539	34.086
20	0953-1028	-81.207	30.652	46	1602-1645	-88.149	33.201
21	1035-1122	-77.800	34.103	46	1602-1724	-87.644	33.323
21	1035-1129	-77.602	34.022	46	1651-1818	-87.950	34.135

21	1136-1215	-77.626	34.323	46	1705-1928	-88.397	29.882
21	1255-1437	-78.761	34.170	46	1955-2138	-88.078	29.865
21	1308-1427	-78.095	33.775	46	2056-2123	-88.121	29.860
22	1740-1834	-76.189	34.175	47	2232-2315	-87.742	29.887
22	1750-1913	-76.081	34.494	47	2238-2346	-88.079	29.815
22	1959-2051	-76.628	34.601	47	2303-2358	-87.790	29.891
22	2019-2051	-77.019	34.691	47	2303-2358	-87.946	29.874
23	0517-0625	-89.526	29.751	47	2315-2358	-95.232	29.528
23	0544-0639	-89.279	29.917	47	2321-0024	-95.389	29.294
23	0618-0707	-89.015	30.186	47	2327-0035	-95.347	29.635
23	0817-0937	-89.039	30.289	52	0232-0336	-81.750	27.255
23	0950-1038	-89.231	30.258	52	0259-0515	-81.756	27.214
23	0950-1044	-89.411	30.088	52	0248-0515	-82.327	26.859
24	1058-1131	-93.350	29.398	52	0445-0632	-82.249	27.008
26	0852-0944	-94.530	29.469	52	0455-0650	-82.237	26.936
26	1432-1511	-94.825	28.589	52	0504-0805	-82.255	26.864
26	1849-2000	-94.572	29.222	53	1828-1914	-81.676	29.764
26	2148-2342	-94.843	28.679	53	1828-2057	-81.603	29.719
26	2211-2320	-95.564	28.966	53	2018-2139	-81.579	29.970
26	2211-2245	-95.672	28.971	53	2018-2104	-81.663	29.679
26	2240-2354	-94.867	28.764	54	1605-1731	-84.185	29.758
26	2257-0040	-94.825	28.796	54	1625-1745	-83.422	29.466
26	2342-0102	-94.464	28.648	56	2019-2113	-83.821	29.882

Table 3.2. Supercells detected by the MDA with at least five successive scans within 100 km of a WSR-88D. The associated manual analysis constructed time slot for each supercell is displayed in the first column, the time range (UTC) in which the MDA detected the supercell is located is in the second column, and the starting latitude and longitude are in columns three and four, respectively.

Corresponding Supercell #	Storm	Time Period (UTC)	Start Lat.	Start Long.	Rating
21	Debby	1940-1943	-82.844	27.878	EF1
24	Debby	1923-1930	-81.440	27.270	EF1
28	Debby	2039-2041	-82.375	28.151	EF0
29	Debby	2117-2119	-82.715	28.237	EF1
35	Debby	0021-0025	-82.740	27.700	EF1
51	Andrea	1513-1516	-82.414	27.027	EF0
77	Arthur	0540-0541	-76.270	36.920	EF0
102	Harvey	1918-1919	-94.770	29.310	EF0
103	Harvey	2311-2320	-95.545	29.146	EF0
112	Harvey	0528-0537	-95.305	29.299	EF0
112	Harvey	0550-0557	-95.450	29.438	EF0
112	Harvey	0550-0552	-95.452	29.438	EF1
112	Harvey	0552-0553	-95.460	29.448	EF1
112	Harvey	0556-0559	-95.517	29.487	EF1
113	Harvey	0712-0714	-96.760	29.700	EF0
117	Irma	2235-2239	-80.104	26.138	EF0
120	Nate	1858-1859	-87.693	30.246	EF0
128	Michael	1932-1936	-83.880	32.460	EF0
128	Michael	1958-2007	-84.027	32.653	EF1
134	Dorian	0923-0926	-78.265	34.062	EF1
136	Dorian	0919-0925	-77.940	33.969	EF0
137	Dorian	1037-1041	-78.247	34.252	EF0
139	Dorian	1017-1022	-78.265	34.062	EF0
139	Dorian	1039-1041	-77.940	33.969	EF0
142	Dorian	1145-1153	-78.247	34.352	EF0
144	Dorian	1302-1331	-77.900	34.221	EF2
150	Dorian	1830-1838	-77.120	35.350	EF0
179	Isaias	0448-0449	-76.801	35.644	EF1
179	Isaias	0450-0451	-76.729	35.426	EF1
212	Elsa	2045-2051	-81.607	30.281	EF1

Table 3.3. Information regarding tornado reports in the TC tornadic supercell cases. Column one indicates the supercell number the tornado report is associated with (from Table 3.2), column two indicates the associated tropical cyclone, column three lists the start and end times (UTC) of the tornado, columns four and five list the start latitude and longitude of the tornado report and column six lists the rating of the tornado.

3.2 Environmental Data

Environmental data were gathered for each supercell in the TC and midlatitude dataset in order to compare environmental characteristics to polarimetric signatures in tornadic and nontornadic tropical cyclone supercells. Proximity soundings from the NCEI archive of Rapid Refresh (RAP) model analysis were obtained for each supercell from the RAP archive Thematic Real-time Environmental Distributed Data Services (THREDDS) server. RAP model soundings include 51 vertical levels with a horizontal grid spacing of 13 km. Cases before 1 May 2012 were obtained from the Rapid Update Cycle (RUC) model which includes 40 vertical levels and a horizontal grid spacing of 40 km. For the nontornadic cases, RAP model soundings were obtained at the closest hour to the supercell's maximum low-level rotation, measured using normalized rotation (NROT). NROT is calculated using azimuthal shear values associated with a rotation couplet that is then normalized by range. These values range from -5 to 5, in which values over 1 are significant and values over 2.5 are extreme (Cooper and Vorst 2016). If the maximum NROT occurred between 25 and 35 minutes after the hour, a RAP model sounding was obtained from the bottom and top of the hour and averaged to estimate the environmental conditions midway through the hour. A similar procedure was followed to identify RAP model sounding times for tornadic cases in which the initial time was dependent on the hour closest to the first tornado report.

Location of the RAP model sounding was required to be no more than 40 km away from the storm in the inflow region. The inflow region was determined with the guidance of radar data downloaded from the NCEI Nex-Generation Radar (NEXRAD) archive at the previously determined time of the RAP model sounding

(https://www.ncdc.noaa.gov/nexradinv/map.jsp) and examined in the Gibson Ridge Analyst-2 software (http://www.grlevelx.com/). A marker was first placed across the gradient of low reflectivity values to high reflectivity values near the weak echo region (WER). This tight reflectivity gradient is a proxy for the updraft region of a supercell and therefore represents a region where air is being ingested into the storm (Potvin et al. 2010). From the location of the first marker, a RAP sounding location was chosen approximately 40 km from the supercell following the inflow wind direction to obtain the sounding. Midlatitude RAP soundings were obtained by Wilson and Van Den Broeke (2022) following the same methodology; however these may be from up to 80 km away from the supercell. Thermodynamic and kinematic environmental variables as well as derived parameters were calculated in Python using the Meteorological Python (MetPy Version 1.4, May et al. 2017) and Sounding/Hodograph Analysis and Research Program (SHARPpy Version 1.4, Blumberg et al. 2017) packages.

Care was taken to ensure sounding locations did not interact with outflow from other storms. The model soundings were examined to determine if they are convectively contaminated. A sounding is considered convectively contaminated if it is saturated throughout a majority of the atmosphere and vertical accelerations exceeded that of a typical synoptic scale environment and instead resemble speeds consistent with a convective updraft (Durran and Snellman 1987). This examination found 63 soundings with convective contamination. Median values of environmental variables calculated for cases with and without convective contamination showed considerable differences in variables important for supercell favorable environments including CAPE, LCL Height, and SRH (Table 3.4), therefore non-contaminated environments will be used in hereafter.

Environmental Variable	Not Convectively Contaminated	Convectively Contaminated	WMW *p*-value
LCL Height [m]	612.0	502.3	< **0.001**
LFC Height [m]	734.3	622.0	**0.04**
Mixed Layer CAPE [J kg^{-1}]	1063	573	< **0.001**
Most Unstable CAPE [J kg^{-1}]	1949	1344	< **0.001**
CIN [J kg^{-1}]	-0.3	-0.1	0.18
Effective SRH [m^2 s^{-2}]	195.1	235.6	0.10
Supercell Composite Parameter	7.5	6.2	0.39
Significant Tornado Parameter	1.9	1.8	0.72
3 km Relative Humidity [%]	88.9	98.7	< **0.001**
6 km Relative Humidity [%]	89.1	97.2	< **0.001**
9 km Relative Humidity [%]	74.3	80.9	< **0.001**
3 km Pressure [hPa]	709.5	708.3	< **0.001**
6 km Pressure [hPa]	489.4	488.5	< **0.001**
9 km Pressure [hPa]	329.6	328.7	**0.01**
Freezing Level Height [m]	4846.2	4791.3	0.96
CCL Temperature [K]	295.3	294.9	**0.04**
LCL Temperature [K]	294.2	293.7	**0.04**
1 km Storm Relative Helicity [m^2 s^{-2}]	173. 5	212.8	**0.01**
3 km Storm Relative Helicity [m^2 s^{-2}]	241.7	336.3	< **0.001**
Surface – 1 km Shear [kts]	25.6	31.1	**0.01**
Surface – 3 km Shear [kts]	31.0	37.7	**0.02**
Surface 6 – km Shear [kts]	31.7	35.2	< **0.001**

Table 3.4: Median values of environmental variables from model soundings with convection contamination (n=63) and without convective contamination (n=153) for tropical cyclone supercell cases and their corresponding Wilcoxon-Mann-Whitney *p*-values (boldface values indicate statistical significance at the 5% level).

A number of thermodynamic and kinematic environmental variables are important in supporting the development of supercells. Thermodynamic variables include MLCAPE, MUCAPE, 0-3 km CAPE, convective inhibition (CIN), height of the freezing level, and the height and temperature of the LFC (Thompson et al. 2003). MLCAPE describes the potential energy available for parcels of air when the lowest 100 hPa are mixed and lifted to the LFC, while MUCAPE is calculated for the most unstable parcel of air in the lowest 300 hPa when lifted to the LFC. CIN quantifies the "negative" energy that a parcel must overcome before convective initiation can occur.

Kinematic environmental variables considered include 0-1 km, 0-3 km, and 0-6 km shear. Shear magnitudes represent the vertical shear difference between the surface and low- to mid-level depths. Storm relative helicity (SRH) utilizes the expected storm motion and the low-level vertical wind shear to measure the potential for cyclonic rotation in a supercell's updraft. SRH was calculated using Bunkers sounding-derived storm motion for the effective inflow layer (ESRH), 0-1 km layer, and 0-3 km layer (Bunkers et al. 2014). Prior literature has indicated that Bunkers motion is a reliable estimate in supercells associated with landfalling tropical cyclones (Bunkers et al. 2000; Nowotarski et al. 2021). Bunkers motion was compared with observed storm motion in a random 10 percent of cases in this study and corresponded well (mean absolute error of 5.2 deg and 4.6 kts for storm direction and speed, respectively). Supercell composite parameter (SCP) was derived to highlight environments with a conglomerate of supercell-favorable ingredients. Significant tornado parameter (STP) was also derived to highlight environments with ingredients favorable for supercells with EF2-EF5 tornadoes (Thompson et al. 2004). Environments were also required to be spatiotemporally

independent as one representative sounding was chosen for cases within 120 km and 3 hours of each other (Thompson et al. 2003). This requirement removed 89 soundings while 50 nontornadic and 14 tornadic TC soundings remain.

3.3 Quantifying Dual-Polarimetric Radar Signatures

Dual-polarimetric signatures in each supercell were analyzed with the Supercell Polarimetric Observation Research Kit (SPORK; Wilson and Van Den Broeke 2021). This automated Python algorithm identifies and quantifies dual-pol signatures through time in WSR-88D data. The algorithm allows for the user to input two reflectivity thresholds to aid in the tracking algorithm. The first reflectivity threshold was set to 40 dBZ to create contours of reflectivity values and assign a set storm ID to the storm centroid and allow the storm to be tracked through time. A second reflectivity threshold was set to 45 dBZ which allows for a storm object with a size greater than 300 km^2 to be divided into multiple storm objects. These reflectivity thresholds are small enough to allow TC supercells to be assigned an identifier while neighboring convection associated with tropical cyclone rainbands typically is not. To allow for the tracking of a storm through time, the algorithm utilized a radius threshold set to 10 km to determine if the storm centroid would retain its previous storm ID. A new identifier was assigned if this distance threshold was exceeded. This threshold may be altered for faster moving storms, however that was not necessary for any of the TC cases. A forward-flank downdraft (FFD) vector was also input for each case. This value was determined manually by plotting a vector perpendicular to the storm's forward flank and pointing towards the core of the storm. The input of this variable allows the algorithm to identify the inflow side of the storm for Z_{DR} arc calculations. A Z_{DR} calibration factor was also input into the

algorithm to modify the Z_{DR} field in order calibrate the Z_{DR} field (Ryzhkov et al. 2005). Z_{DR} calibration was accomplished using the methodology of Picca and Ryzhkov (2012) that was later applied by Van Den Broeke (2017).

Due to the often small and varying nature of dual-pol signatures in TC supercells, this study opted to use the Thunderstorm Risk Estimation from Nowcasting Development via Size Sorting (TRENDSS; Kingfield and Picca 2018) version of the SPORK algorithm. The TRENDSS algorithm creates Z_{HH}-Z_{DR} relationships for each individual radar scan at every elevation angle to identify positive Z_{DR} outliers that may be indicative of size sorting. This algorithm is a more reliable identifier for size sorting than a static threshold, and mitigates issues that may interfere with the algorithm (Wilson and Van Den Broeke 2021).

For comparisons between pretornadic and nontornadic dual-polarimetric signatures, the analysis period for pretornadic supercells is defined as 30 minutes prior to the first tornado report. For nontornadic supercells, the analysis period is 30 minutes prior to the maximum low-level NROT at the lowest elevation angle scan (Cooper and Vorst 2016). Maximum NROT values were calculated by the Gibson Ridge Analyst-2 software (http://www.grlevelx.com/). Cases that did not have a consistent MDA detection for the 30 minutes prior to the maximum NROT value or first tornado report are excluded from these calculations, therefore removing 34 nontornadic cases and one tornadic case. This methodology is consistent with the comparative midlatitude dataset in which 19 nontornadic cases and eight tornadic cases were removed (Wilson and Van Den Broeke 2022). Dual-polarimetric signatures quantified by the SPORK algorithm for each scan of the identified storms include:

1) Z_{DR} arc maximum value (dB)
2) Z_{DR} arc mean value (dB)
3) Z_{DR} arc median values (dB)
4) Hailfall area (km^2)
5) Reflectivity area greater than 35 dBZ (km^2)
6) K_{DP}-Z_{DR} separation distance (km)
7) K_{DP}-Z_{DR} separation angle (deg)
8) Z_{DR} column area (km^2)
9) Z_{DR} column maximum depth (km)
10) Z_{DR} column mean depth (km)

An example SPORK run with plotted signatures for a TC supercell may be viewed in Figure 3.1. These quantified variables were compared between tornadic and non-tornadic TC supercells as well as between TC and midlatitude supercells.

Post-processing of SPORK output included a few additional measures to ensure data quality. The algorithm outputs a value of zero for very small non-zero values that may be a result of the WSR-88D resolution or the absence of a signature in a supercell. Due to this issue, for all signatures where zero is an unrealistic result, zero values were removed from calculation. Unrealistic zero values were removed in the K_{DP}-Z_{DR} separation angle and distance outputs (Table 3.5). For Z_{DR} arc and K_{DP} foot variables besides area, the SPORK algorithm reports the value as zero even if the signature is not present, so zero values were also removed for these signatures. Due to the small and relatively weaker nature of TC supercells, it was not uncommon for supercells to not exhibit the full set of dual-polarimetric signatures analyzed by SPORK. Of the 216 TC

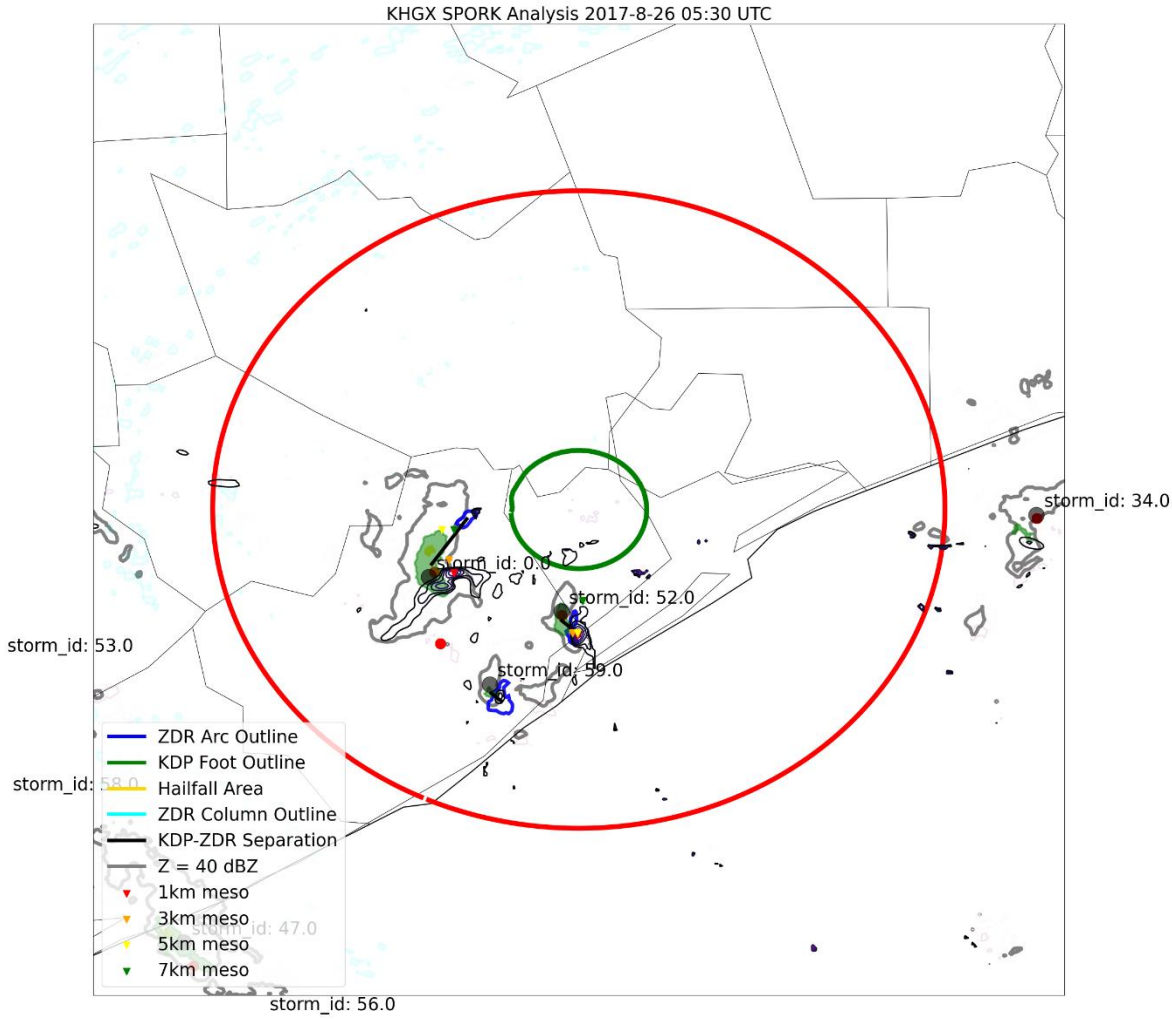

Figure 3.1. Example of a SPORK output file from KHGX tracking two TC supercells in Hurricane Harvey on 26 August 2017 at 0530 UTC. The radar appears in the center of the image with the green circle indicating 10 km range and the red circle indicating 75 km range. Grey dots indicate storm centroids with the associated storm ID to the northeast, red dots indicate storm centroid locations from the previous scan, grey contours indicate reflectivity values greater than or equal to 40 dBZ, blue contour surrounds the Z_{DR} arc, green shading encompasses the K_{DP} foot, and the black line indicates the separation between the Z_{DR} arc and K_{DP} foot. Triangles indicate the 1 km, 3km, 5km, and 7km mesocyclone in red, orange, yellow, and green, respectively.

Signature	Units	Zero values removed	Total # of Occurrences in TC Cases
Z_{DR} Arc Maximum Value	dB	Yes	116
Z_{DR} Arc Mean Value	dB	Yes	116
Z_{DR} Arc Median Value	dB	Yes	116
Hailfall Area	km^2	No	9
Reflectivity Area > 35 dBZ	km^2	No	202
K_{DP}-Z_{DR} Separation Distance	km	Yes	116
K_{DP}-Z_{DR} Separation Angle	deg	Yes	116
Z_{DR} Column Area	km^2	No	41
Z_{DR} Column Maximum Depth	km	No	41
Z_{DR} Column Mean Depth	km	No	41

Table 3.5. Dual-polarimetric signatures recorded with the SPORK algorithm and their corresponding units in the second column. The third column indicates whether or not algorithm-reported zero values are removed and the fourth column indicates how many storms exhibited each signature out of the 216 TC cases.

supercell cases, 116 cases had a Z_{DR} arc, 119 cases had a K_{DP} foot, 41 cases had a Z_{DR} column, and 9 cases had a hailfall area (Table 3.5). Due to the presence of both a Z_{DR} arc and K_{DP} foot being required in order to obtain the K_{DP}-Z_{DR} separation angle and distance, 116 cases had separation distance and angle values. Reflectivity area values were contaminated in 14 cases by interference from surrounding convection associated with TC rainbands. Reflectivity signatures from these cases were not included in further analyses. These quantified variables were compared between midlatitude and TC supercells and between tornadic and nontornadic TC supercells.

3.4 Statistical Analysis

For both the TC and midlatitude supercell cases, median values of SPORK metrics were calculated for either the 30 minutes prior to the maximum NROT value for nontornadic cases or 30 minutes prior to the first tornado report for tornadic cases. Median values were chosen instead of means since median is more outlier resistant. Wilcoxon-Mann-Whitney (WMW) statistics were calculated for the comparison of two variables with a null hypothesis that the metric median values could have come from the same distribution. WMW statistics were utilized to calculate *p* values for radar metrics as they may be non-Gaussian.

Chapter IV: Results

4.1 Comparison of Tropical Cyclone Tornadic and Nontornadic Supercell Environments with Midlatitude Environments

The tropical cyclone environment differs from that of a typical midlatitude supercell. This section investigates the differences between TC and midlatitude supercell environments in the context of known differences. Consistency with prior findings would support that this sample of TC supercells is representative, indicating that radar signatures are also likely to be representative. In order to compare the environments of TC supercells and midlatitude supercells, proximity RAP model soundings from supercells in each group will be utilized. For the TC supercell environments, only the environments that did not experience convective contamination were included in the comparisons. The 154 TC soundings were divided into 132 nontornadic cases and 21 tornadic cases. The midlatitude supercell environments contain 206 soundings split between 103 tornadic cases and 103 nontornadic cases. Although the midlatitude dataset contains both weakly tornadic and significantly tornadic cases, these groups will not be investigated individually due to the small sample size in TC cases.

Thermodynamic and kinematic environmental variables that can help to distinguish between pretornadic and nontornadic supercells show contrasting characteristics between TC and midaltitude supercells (Table 4.1). Buoyancy is limited in TC environments as the lapse rate is typically close to moist adiabatic, leading to lower values of sounding-derived thermodynamic parameters such as MLCAPE and MUCAPE when compared to midlatitude supercell environments (Figure 4.1). Environments of TC supercells displayed lower values of both MLCAPE (1121 J kg^{-1} and 1672 J kg^{-1},

Variable	Median, Tropical Cyclone	Median, Midlatitude	WMW *p*-value
Lifting condensation level [m]	598.3	1035.0	< **0.001**
MLCAPE [J kg^{-1}]	1121	1672	< **0.001**
MUCAPE [J kg^{-1}]	1978	2256	**0.04**
CIN [J kg^{-1}]	-0.2	-17.1	< **0.001**
Effective SRH [m^2 s^{-2}]	214.8	194.7	0.53
Supercell Composite Parameter	6.7	8.2	0.05
Significant Tornado Parameter	2.0	1.5	0.09
Freezing Level Height [m]	4824.2	3639.1	< **0.001**
0-1 km Storm Relative Helicity [m^2 s^{-2}]	176.0	147.8	**0.05**
0-3 km Storm Relative Helicity [m^2 s^{-2}]	244.4	229.2	0.38
0-1 km Shear [kts]	26.5	19.0	< **0.001**
0-3 km Shear [kts]	32.0	32.9	0.18
0-6 km Shear [kts]	31.0	47.2	< **0.001**

Table 4.1. Variables associated with differences between tornadic and nontornadic storm environments (column 1). Median values of tropical cyclone environments without contamination (columns 2) and median values of midlatitude supercells (column 3) are shown, and the WMW *p*-values from the median value comparisons (column 4) with boldface values indicating statistical significance at the 5% level.

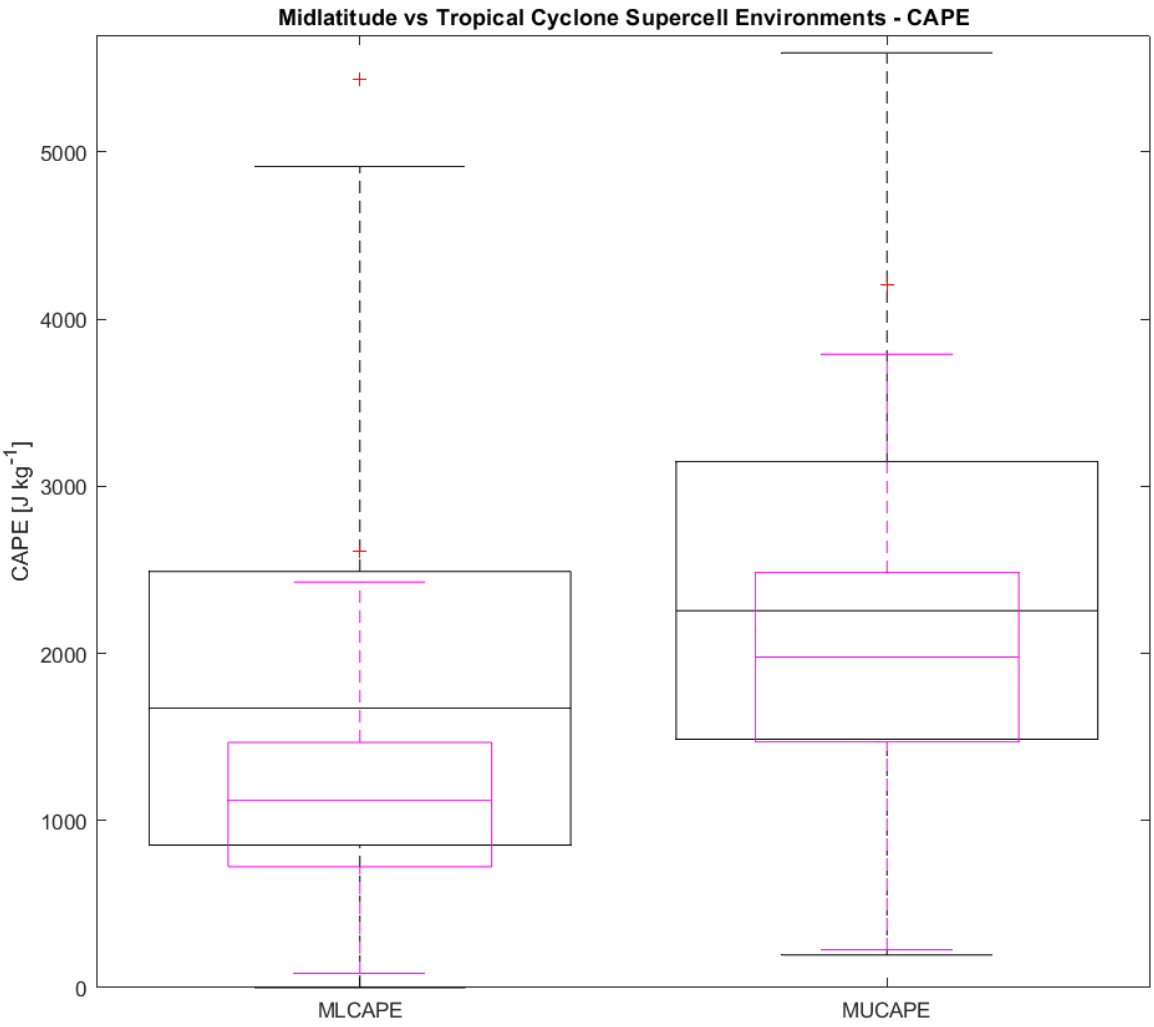

Figure 4.1. Box and whisker plots displaying the distributions of MLCAPE and MUCAPE. The black box and whisker plots display the distribution for midlatitude supercell environments (n=206) while the purple box and whisker plots display the distribution for tropical cyclone supercell environments (n=64). The boxes display the 25th and 75th percentile with the horizontal line indicating the median value. Whiskers convey the 10th and 90th percentile with the outliers represented by red crosses.

respectively) and MUCAPE (1978 J kg^{-1} and 2256 J kg^{-1}, respectively) when compared to midlatitude supercell environments, these differences were statistically significant ($p < 0.001$ and $p = 0.04$, respectively). Distributions of these values in TC cases were more limited than in midlatitude cases with some overlap on the lower end of values (Figure 4.1). This finding is consistent with prior literature noting that buoyancy and CAPE values are much smaller in TC supercell environments than in midlatitude environments (McCaul 1991; McCaul and Weisman 1996; Davies 2006; Nowotarski et al. 2021). Freezing level heights are also greater in TC environments than midlatitude environments (4824.2 m and 3639.1 m, respectively); this difference is statistically significant ($p < 0.001$). However, LCL heights are typically smaller in TC environments than midlatitude environments (598.2 m and 1035.0 m, respectively; $p < 0.001$). These results were expected due to the high dewpoints and fairly uniform low-level thermodynamic profile in TC environments.

Kinematic environmental variables also differ between TC and midlatitude supercell environments. Low-level vertical wind shear in TC environments is generally larger than in midlatitude environments, helping to aid the production of supercells even in a buoyancy-limited environment. TC environments displayed significantly larger 0-1 km shear values than midlatitude environments (26.5 kts and 19.0 kts, respectively; $p < 0.001$; Table 4.1). In turn, midlatitude environments when compared to TC environments had significantly larger values of both 0-6 km shear (47.2 kts and 31.0 kts, respectively; $p < 0.001$; Figure 4.2). A similar result was seen for SRH as TC environments had larger 0-1 km SRH (176.0 m^2 s^{-2} and 147.8 m^2 s^{-2}, respectively; $p = 0.05$; Figure 4.3). Larger values of both low-level shear and SRH in TC cases is consistent with prior literature as

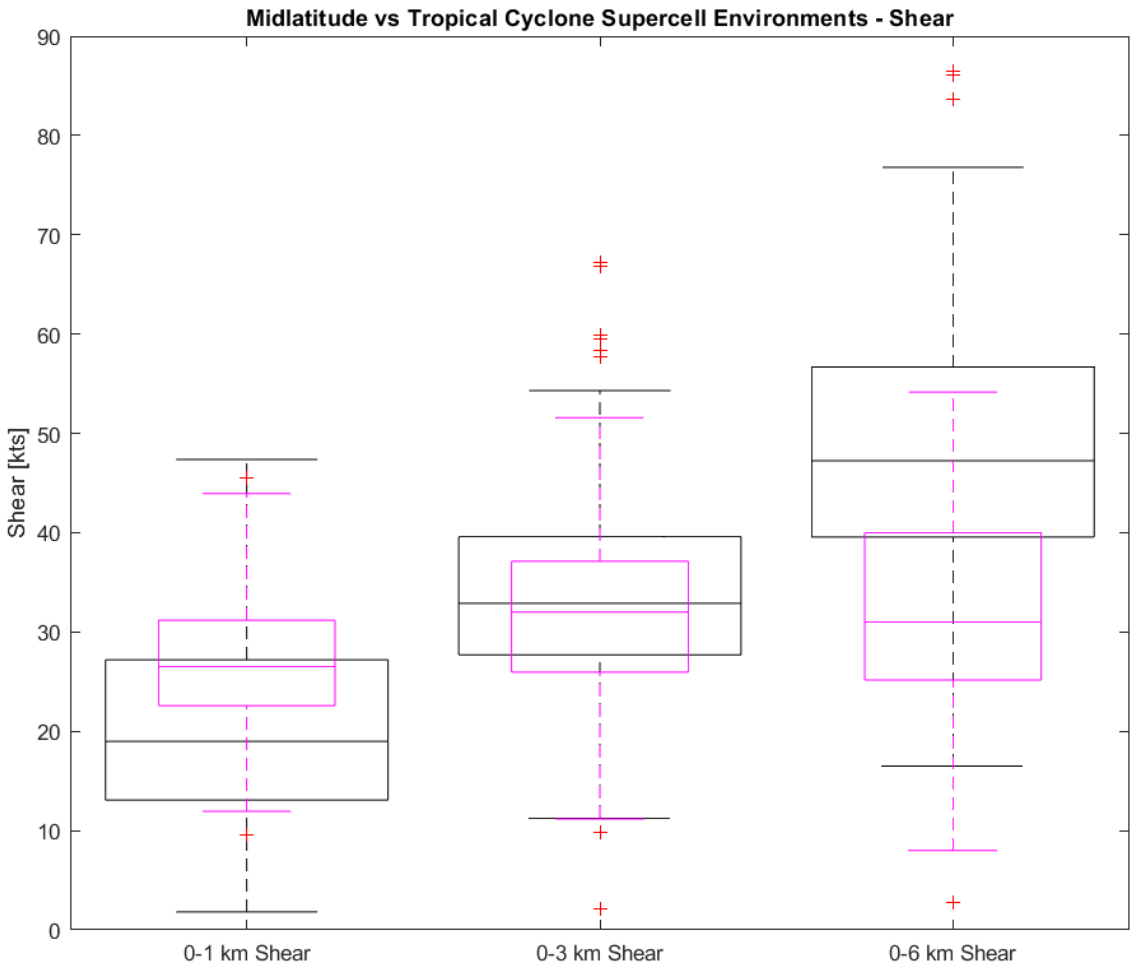

Figure 4.2. As in Fig, 4.1, but for 0-1 km, 0-3 km, and 0-6 km shear.

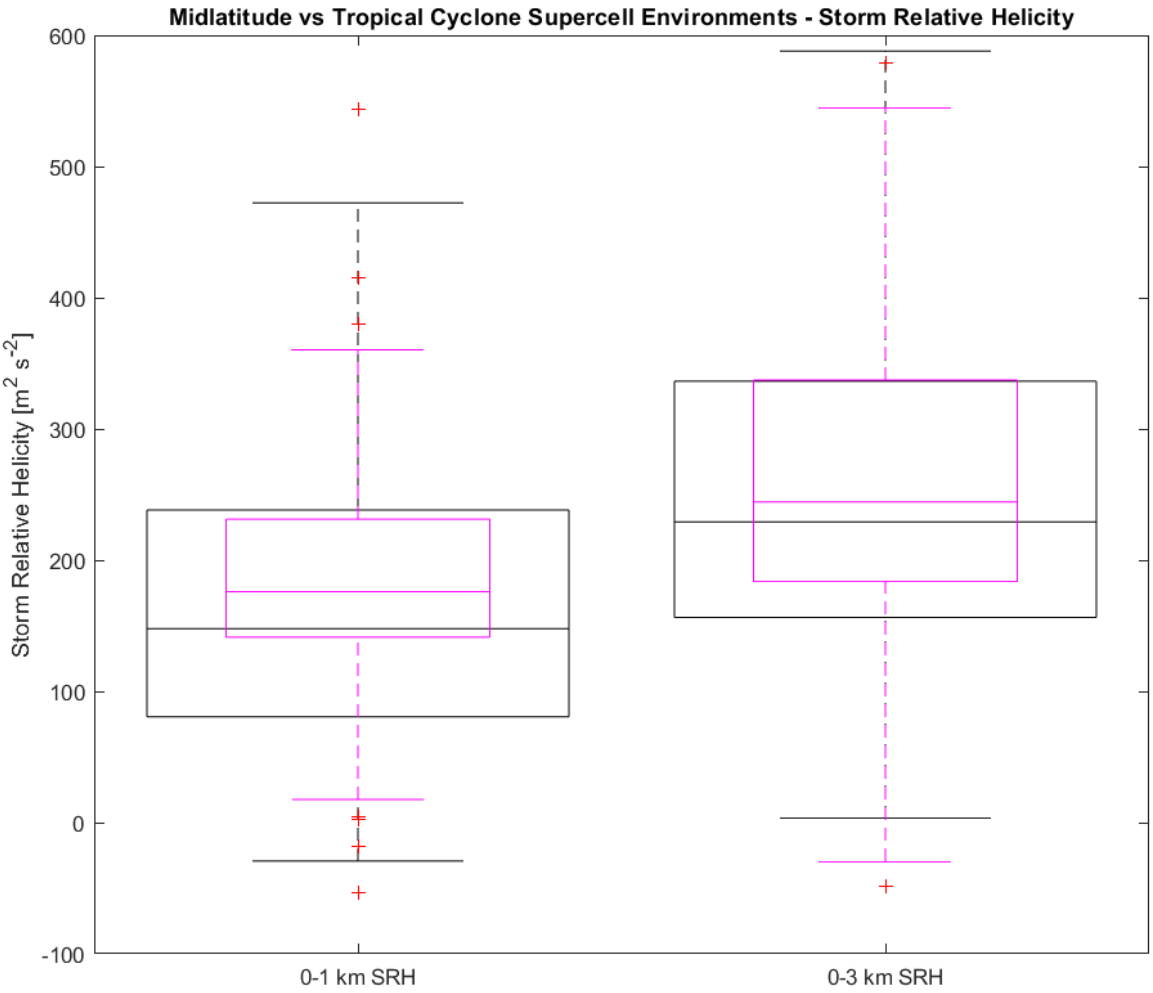

Figure 4.3. As in Fig. 4.1, but for 0-1 km and 0-3 km SRH.

SRH tends to be maximized downshear from the TC center in the supercell-favored northeast sector (McCaul 1991; McCaul and Weisman 1996; Schneider and Sharp 2007; Molinari and Vollaro 2010). Despite differences in thermodynamic and kinematic variables between TC and midlatitude environments, no significant differences were found between SCP and STP (Table 4.1). This result shows that while the environments are very different, the buoyancy-shear relationship is fairly similar between them.

Environments showed fewer differences between midlatitude and TC tornadic cases. While freezing level height and LCL height remained significantly larger in midlatitude tornadic cases, both 0-1 km and 0-3 km shear and SRH showed no significant differences (Table 4.2). Median tornadic 0-1 km shear and SRH values for both the TC and midlatitude datasets are consistent with those of Thompson et al. (2003) who observed 413 close proximity RUC soundings to midlatitude tornadic and nontornadic supercells. These variables have reasonably low overlap between tornadic and nontornadic midlatitude cases, however this is not the case between tornadic and nontornadic TC cases (Figure 4.4). There is large overlap in 0-1 km shear and SRH between tornadic and nontornadic TC cases, making it a less reliable indicator of a supercell's tornado potential. This will be discussed further in the next section.

Differences in environmental variables can provide insight into the expected changes in radar metrics between midlatitude and TC supercells. It is expected that hailfall area will be larger in midlatitude supercells and rarely observed in TC supercells. Significantly larger freezing level heights and higher RH throughout the depth of TC environments make the likelihood of hail surviving to base scan low. In addition, previous modeling work has shown that supercells with higher SRH and more curved

Variable	Median, Tornadic Tropical Cyclone	Median, Tornadic Midlatitude	WMW p-value
Lifting condensation level [m]	586.1	884.4	< **0.001**
MLCAPE [J kg^{-1}]	1409	1710	0.09
MUCAPE [J kg^{-1}]	2428	2408	0.70
CIN [J kg^{-1}]	-0.2	-10.0	< **0.001**
Effective SRH [m^2 s^{-2}]	233.3	251.9	0.81
Supercell Composite Parameter	10.4	9.9	0.84
Significant Tornado Parameter	2.6	2.1	0.31
Freezing Level Height [m]	4800.1	3717.4	< **0.001**
0-1 km Storm Relative Helicity [m^2 s^{-2}]	191.8	186.4	0.92
0-3 km Storm Relative Helicity [m^2 s^{-2}]	270.6	271.8	0.94
0-1 km Shear [kts]	26.1	23.7	0.19
0-3 km Shear [kts]	31.4	34.2	0.36
0-6 km Shear [kts]	34.8	48.9	< **0.001**

Table 4.2. As in Table 4.1, but for tornadic tropical cyclone and midlatitude environments.

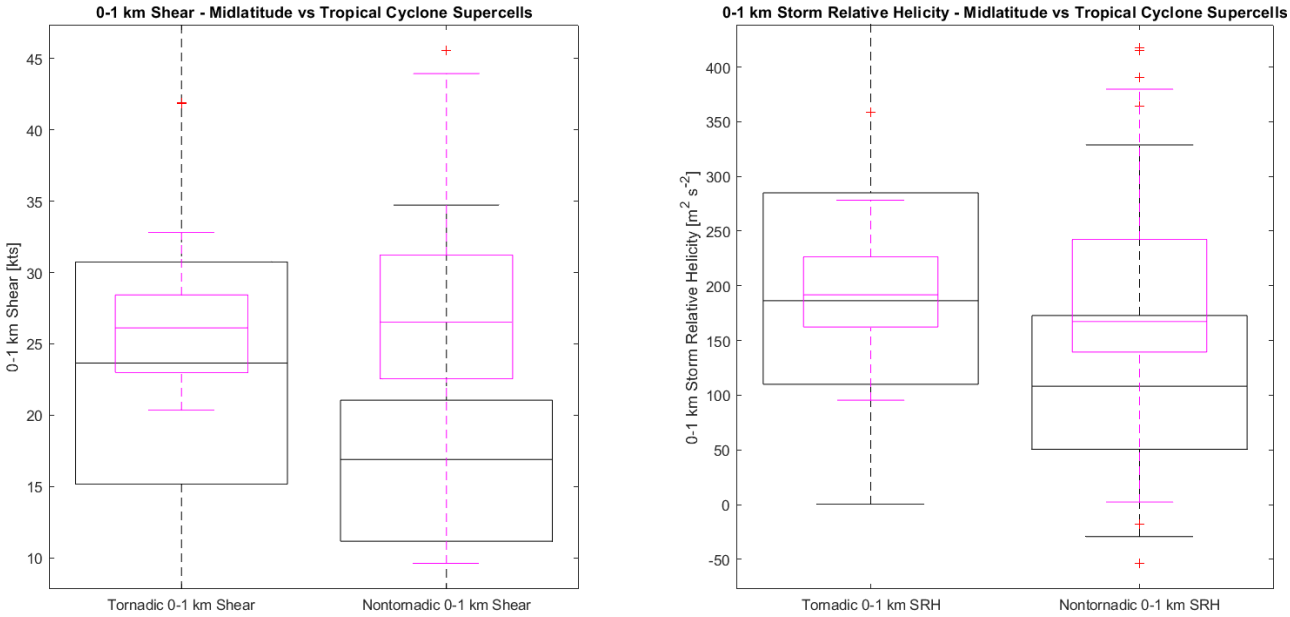

Figure 4.4. As in Fig. 4.1, but for tornadic and nontornadic 0-1 km shear (left panel) and 0-1 km storm relative helicity (right panel).

hodographs are less likely to produce large amounts of hail (Kumjian et al 2021; Lin and Kumjian 2022). This is consistent with the findings of Wilson and Van Den Broeke (2022) who saw larger hailfall areas occurring in environments with weaker low-level shear and SRH. The study also found a correlation between hailfall area and both LFC and LCL height, providing more unfavorable conditions for hail surviving to base scan in TC environments as the lower LCL and LFC heights make it harder for hail to survive.

The general miniature nature of TC supercells leads to the expectation that Z_{DR} column area and depth will be smaller in TC cases than midlatitude cases with environmental variables supporting this hypothesis. Wilson and Van Den Broeke (2022) found a low positive correlation between Z_{DR} column area and MLCAPE (r = 0.35), MUCAPE (r = 0.32), and freezing level height (r = 0.37). The study also found a moderate positive correlation between Z_{DR} column maximum and mean depth with MLCAPE (r = 0.52 and r = 0.52, respectively), MUCAPE (r = 0.50 and r = 0.49, respectively), and a low negative correlation with freezing level height (r = 0.35 and r = 0.41, respectively). This supports the hypothesis that larger Z_{DR} column area and depth will be seen in the midlatitude environments with their lower freezing level heights and greater conditional instability than in TC environments.

Environmental differences may also lead to expected differences in Z_{DR} arc size and intensity. Wilson and Van Den Broeke (2020) found that Z_{DR} arcs tend to be larger and more intense in environments with higher LCL heights, lower RH in the low- and mid-levels, and higher values of MLCAPE. This is consistent with Kumjian and Ryzhkov (2008) and Van Den Broeke (2016) who hypothesized that environments with strong updrafts, large values of CAPE, drier low- to mid-levels, and more saturated upper levels

allow for small drops to evaporate while larger drops persist. Wilson and Van Den Broeke (2020) also found a weak correlation between Z_{DR} arc size and intensity with low-level shear and SRH, contrasting with the findings of Kumjian and Ryzhkov (2009). These results lead to the inference that Z_{DR} arcs will be smaller and less intense in TC supercells than midlatitude supercells as the smaller CAPE values and stronger RH throughout the depth of the troposphere will inhibit both the evaporation of smaller drops and increased production of larger drops.

Expectations for separation angle are difficult to account for as Wilson and Van Den Broeke (2022) found moderate positive correlations between 0-1 km shear (r = 0.45), 0-1 km SRH (r = 0.31), and 0-3 km SRH (r = 0.41). These results were consistent with Kumjian (2018, 2020) who indicated that larger separation angles are consistent with environments containing larger SRH values. Loeffler and Kumjian (2020) found that separation angle is typically larger in tornadic environments than nontornadic environments; this was also supported in a small number of TC cases (Crowe et al. 2010). Prior literature indicates that separation angle may behave similarly between TC and midlatitude environments as mesocyclone-induced increases in directional shear aid in drop size sorting of hydrometeors similarly in both environments (Kumjian and Ryzhkov 2008, 2009; Crowe et al. 2010).

4.2 Comparison of Tornadic and Nontornadic Tropical Cyclone Supercell Environments

This section explores the differences between tornadic and nontornadic TC supercell environments in the context of known differences. As in the previous section, RAP model soundings were utilized from nontornadic (n=50) and tornadic (n=14) TC

supercells that did not experience convective contamination. Results that are generally consistent with prior literature are thought to indicate a representative sample. Prior research has indicated that thermodynamic environmental parameters such as LCL, LFC, and freezing level height are not indicative of tornadic potential in a TC environment due to large RH values creating a fairly uniform low-level thermodynamic profile (Davies 2006). This is consistent with our TC dataset as no statistically significant differences between tornadic and nontornadic cases were observed with these variables (Table 4.3). MLCAPE is one of the few thermodynamic variables that prior literature indicates as a discriminator between tornadic and nontornadic cases, with larger values being indicative of higher tornado probability (Davies 2006; Edwards 2012; Nowotarski et al. 2021). The TC dataset shows significantly larger MLCAPE values in tornadic supercells when compared to nontornadic cases (1409 J kg^{-1} and 1037 J kg^{-1}, respectively; $p = 0.03$), though there remains overlap between the 25^{th} percentile of tornadic cases and 75^{th} percentile of nontornadic cases (Figure 4.5).

In terms of kinematic environmental parameters, prior research has indicated that 0-1 km SRH and 0-6 km shear are the best indicators for tornadic potential in TC supercells (Davies 2006; Nowotarski et al. 2021). Both 0-1 km SRH (195.4 $m^2 s^{-2}$ and 171.8 $m^2 s^{-2}$, respectively) and 0-6 km shear (48.9 kts and 35.0 kts, respectively) showed no statistical differences between tornadic and nontornadic cases ($p = 0.17$ and $p = 0.11$, respectively; Table 4.3) though median values appear to be larger in tornadic cases. With these established differences in kinematic and thermodynamic parameters, it is not surprising that there is a statistically significant difference in both SCP (10.8 and 6.84, respectively) and STP (2.6 and 1.7, respectively) between tornadic and nontornadic TC

Variable	Median, Nontornadic	Median, Tornadic	WMW *p*-value
Lifting Condensation Level [m]	602.8	586.1	0.89
Level of Free Convection [m]	731.8	678.2	0.40
MLCAPE [J kg^{-1}]	1037	1409	**0.03**
MUCAPE [J kg^{-1}]	1904	2428	0.11
0-3 km CAPE [J kg^{-1}]	236	247	0.69
CIN [J kg^{-1}]	-0.2	-0.2	0.99
Effective SRH [m^2 s^{-2}]	201.8	233.3	0.09
Supercell Composite Parameter	5.9	10.4	**0.03**
Significant Tornado Parameter	1.7	2.6	**0.03**
Freezing Level Height [m]	4842.8	4800.1	0.69
0-1 km Storm Relative Helicity [m^2 s^{-2}]	167.3	191.8	0.40
0-3 km Storm Relative Helicity [m^2 s^{-2}]	235.4	270.6	0.33
0-1 km Shear [kts]	26.5	26.1	0.99
0-3 km Shear [kts]	32.4	31.4	0.31
0-6 km Shear [kts]	29.9	34.8	0.37

Table 4.3. Environmental variables for tornadic and nontornadic TC storms without convective contamination (column 1). Median values of tornadic cases (column 2) and nontornadic cases (column 3) are shown as well as the WMW *p*-values from the median value comparisons (column 4) with boldface values indicating statistical significance at the 5% level.

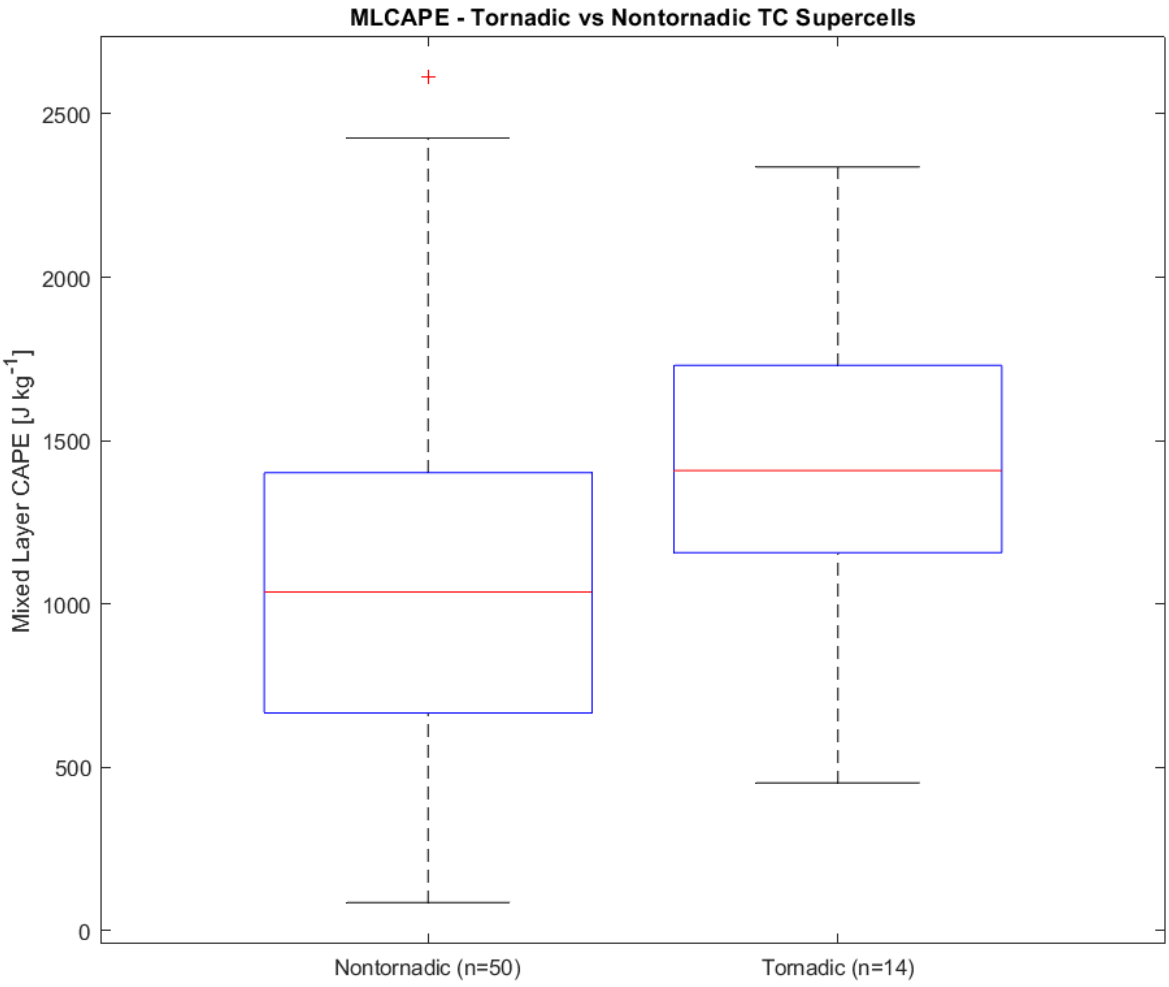

Figure 4.5. Box and whisker plots displaying the distributions of MLCAPE for uncontaminated tornadic and nontornadic TC cases. The boxes display the 25th and 75th percentile with the red horizontal line indicating the median value. Whiskers convey the 10th and 90th percentile with the outliers represented by red crosses.

cases (p = 0.01 and p = 0.01, respectively; Table 4.3). Median values for both SCP and STP were larger for tornadic cases than for nontornadic cases. However, there remains some overlap between the 25th percentile of tornadic cases and 75th percentile of nontornadic cases for both parameters (Figure 4.6). These results are consistent with Nowotarski et al. (2021) who observed similar differences in these parameters between tornadic and nontornadic supercells in Hurricane Harvey (2017).

Differences in near-cell environments tell an important story about the tornadic potential of TC supercells. Nonetheless, each of these environmental variables experience some degree of overlap between the tornadic and nontornadic cases. This overlap points towards the potential importance of radar data to aid in the detection of a supercell's tornadic potential. Understanding the discriminatory differences between radar signatures in pretornadic and nontornadic supercells can play a key role in understanding the microphysical processes occurring in a storm. Understanding and identifying these differences can lead to improved warning times and lower false alarm ratios for TC supercells.

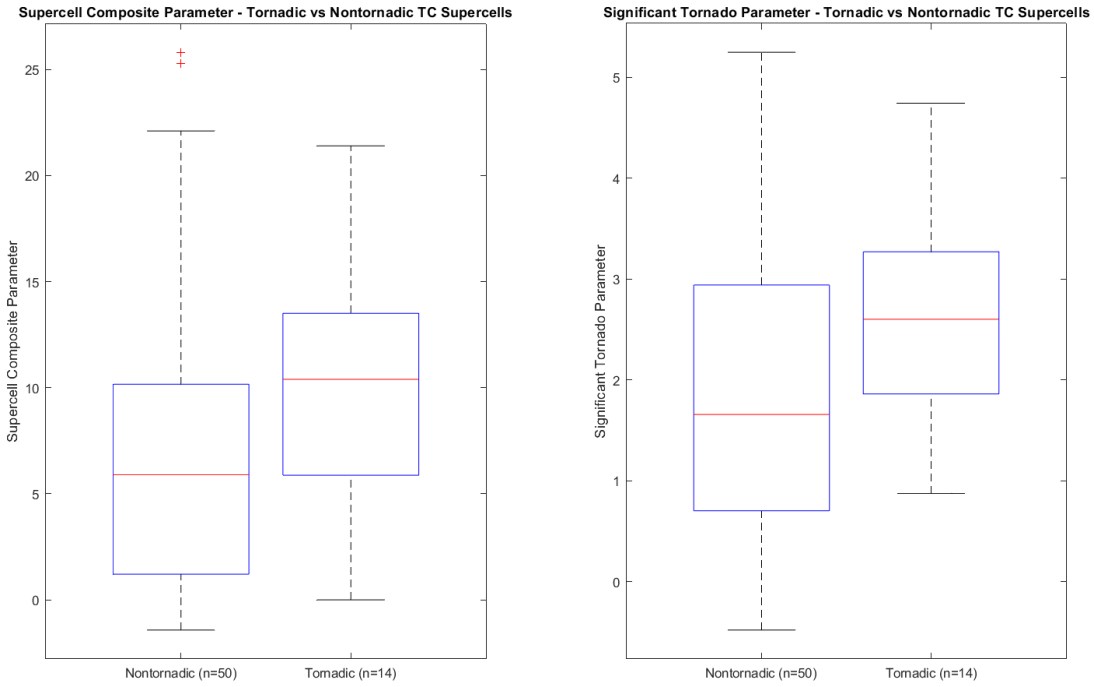

Figure 4.6. As in Fig. 4.5, but for supercell composite parameter (left panel) and significant tornado parameter (right panel).

4.3 Comparison of Polarimetric Signatures between Tropical Cyclone and Midlatitude Supercells

Establishing differences between polarimetric signatures in midlatitude and tropical cyclone supercells can aid in the understanding of physical mechanisms responsible for these signatures and the microphysical implications they have in a TC setting. With prior literature establishing that tropical cyclone supercells are typically smaller in both the horizontal and vertical extent when compared to their midlatitude counterparts (Edwards 2012), these differences should be seen in their polarimetric signatures. Established environmental differences may also promote contrasting polarimetric signature characteristics between midlatitude and TC supercells.

Median values of pre-tornadic (PT) and pre-maximum NROT (NT) polarimetric signatures in both midlatitude and TC cases as well as their corresponding WMW *p* values between midlatitude and TC cases can be seen in Table 4.4. Storm size was significantly smaller in TC cases than midlatitude cases for both NT and PT storms ($p < 0.001$; Figure 4.7). On average, supercells were approximately half the size in TC cases when compared to midlatitude cases (Table 4.4). This result agrees with prior literature that TC supercells are generally smaller in horizontal extent than midlatitude supercells. Hailfall area was also significantly smaller in TC cases than midlatitude cases ($p < 0.01$ for NT and $p = 0.01$ for PT cases), with median hailfall area in TC cases of 0.00 km^2 in both NT and PT TC cases (Figure 4.8). The lack of hailfall area in TC supercells will be discussed further in the next section.

Variable	Pre-Maximum NROT			Pretornadic		
	Median, Mid-Latitude	Median, Tropical Cyclone	WMW *p*-Value	Median, Mid-Latitude	Median, Tropical Cyclone	WMW *p*-Value
Reflectivity Area [km^2]	471.13	252.57	< **0.001**	429.54	200.21	< **0.001**
Hailfall Area [km^2]	4.24	0.00	< **0.001**	0.00	0.00	**0.01**
Z_{DR} Column Area [km^2]	23.15	2.95	< **0.001**	33.92	4.44	< **0.001**
Normalized Z_{DR} Column Area	0.05	0.01	< **0.001**	0.07	0.03	**0.02**
Z_{DR} Column Mean Depth [km]	1.58	0.56	< **0.001**	1.72	1.27	**0.01**
Z_{DR} Column Maximum Depth [km]	3.00	1.50	< **0.001**	3.25	1.56	< **0.001**
Z_{DR} Arc Mean Value [dB]	3.66	4.02	< **0.001**	3.67	3.98	< **0.001**
Z_{DR} Arc Maximum Value [dB]	4.64	5.33	< **0.001**	4.58	5.32	< **0.001**
K_{DP}-Z_{DR} Separation Distance [km]	7.30	5.25	< **0.001**	7.10	5.18	< **0.001**
Normalized K_{DP}-Z_{DR} Separation Distance	0.02	0.02	0.06	0.02	0.02	**0.01**
K_{DP}-Z_{DR} Separation Angle [deg]	27.61	115.89	< **0.001**	69.78	101.98	< **0.001**

Table 4.4. Midlatitude and tropical cyclone supercell SPORK median values of polarimetric radar metrics (column 1) for pre-maximum NROT cases (columns 2-4) and pretornadic cases (columns 5-7). Corresponding WMW *p* values between pre-maximum NROT midlatitude and TC cases are displayed in column 4 while WMW *p* values between pretornadic midlatitude and TC cases are displayed in column 7 with boldface values indicating statistical significance at the 5% level.

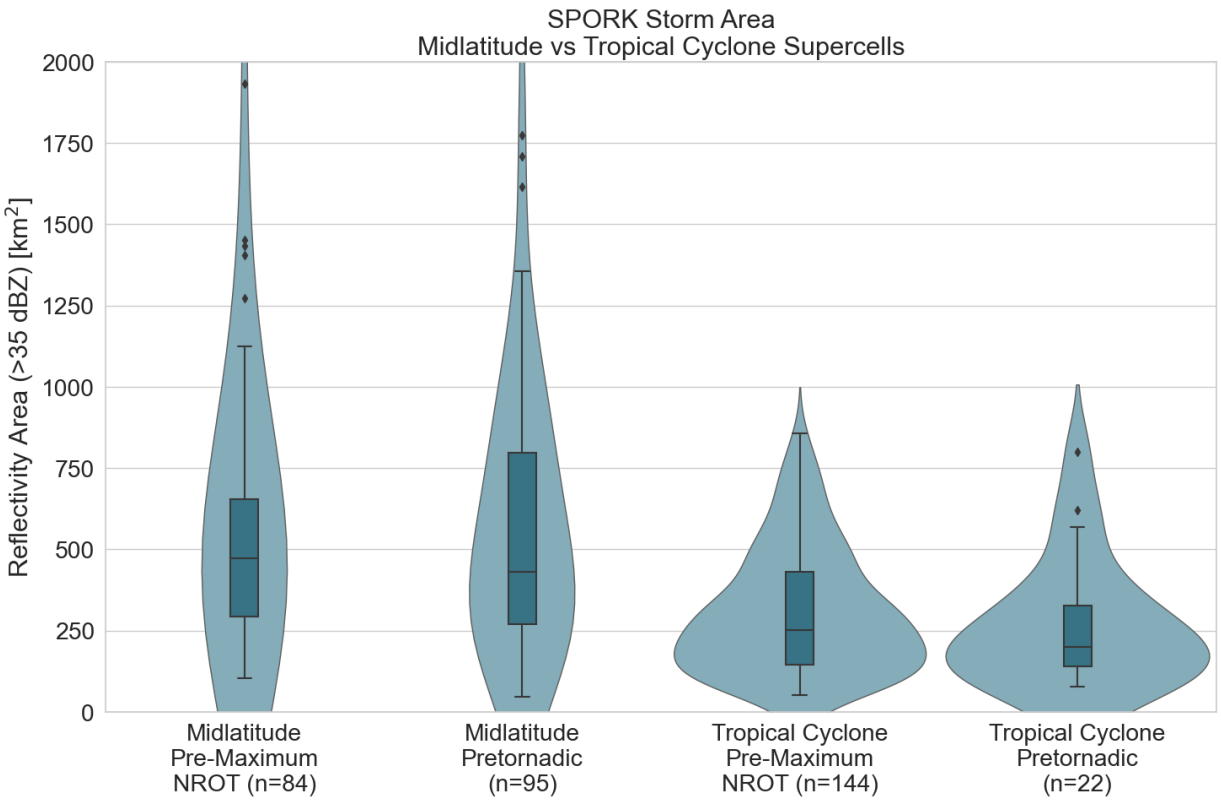

Figure 4.7. Violin plots displaying the distribution of median SPORK reflectivity area greater than 35 dBZ [km^2] for midlatitude pre-maximum NROT (left), midlatitude pretornadic (middle left), tropical cyclone pre-maximum NROT (middle right), and tropical cyclone pretornadic (right) TC supercells. Values are valid for 30 minutes prior to the maximum NROT and first tornado report. The number of samples contributing to each violin are indicated on the axis labels. Box and whisker plots are embedded in violin plots with boxes displaying the 25th and 75th percentile and the black horizontal line indicating the median value. Whiskers convey the 10th and 90th percentile with the outliers represented by black diamonds.

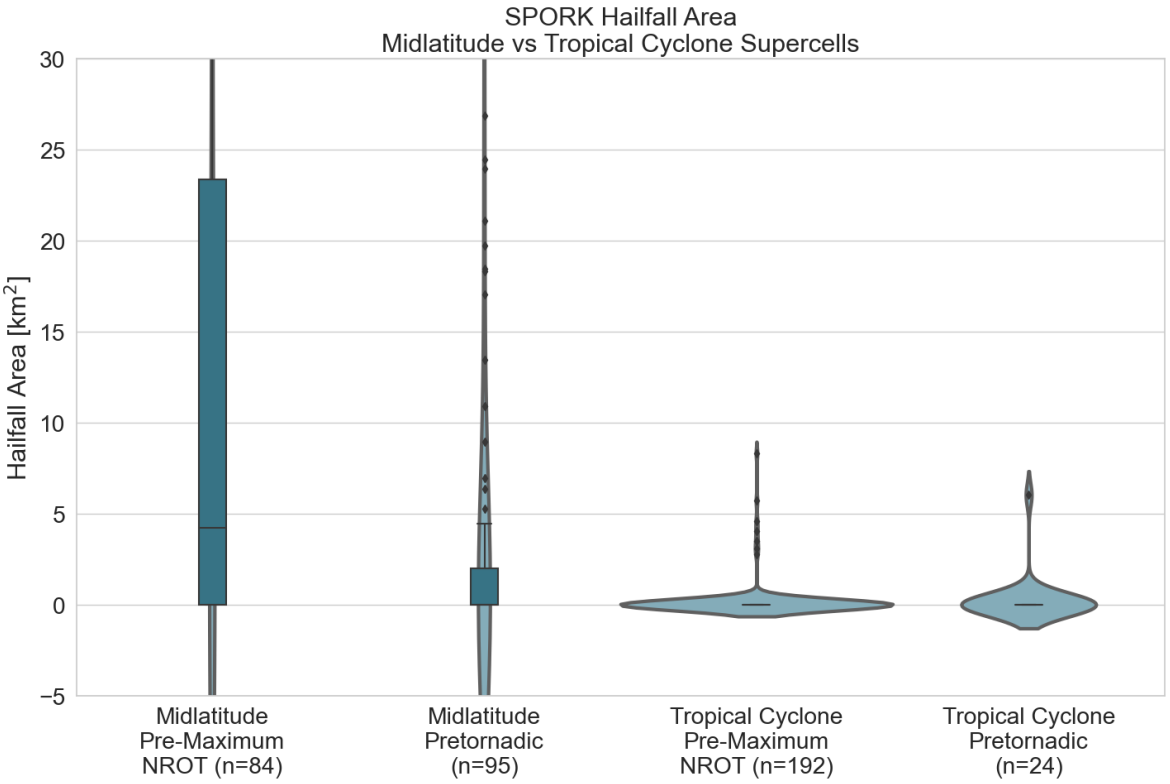

Figure 4.8. As in Fig. 4.7, but for SPORK hailfall area [km^2].

Differences in Z_{DR} column area and depth can serve as proxies for differences in updraft characteristics between midlatitude and TC supercells. Both Z_{DR} column area and normalized Z_{DR} column area (Figure 4.9) were significantly smaller in TC supercells than midlatitude supercells (Table 4.4), including both PT and NT ($p = 0.02$ and $p < 0.001$, respectively). Occurrences of Z_{DR} columns were infrequent in TC cases compared to midlatitude cases. Midlatitude cases experienced Z_{DR} columns in 94.0% and 95.8% of NT and PT cases, respectively. Meanwhile, TC cases experienced Z_{DR} columns in only 18.2% and 25.0% of NT and PT cases, respectively. These results will be investigated further in the next section.

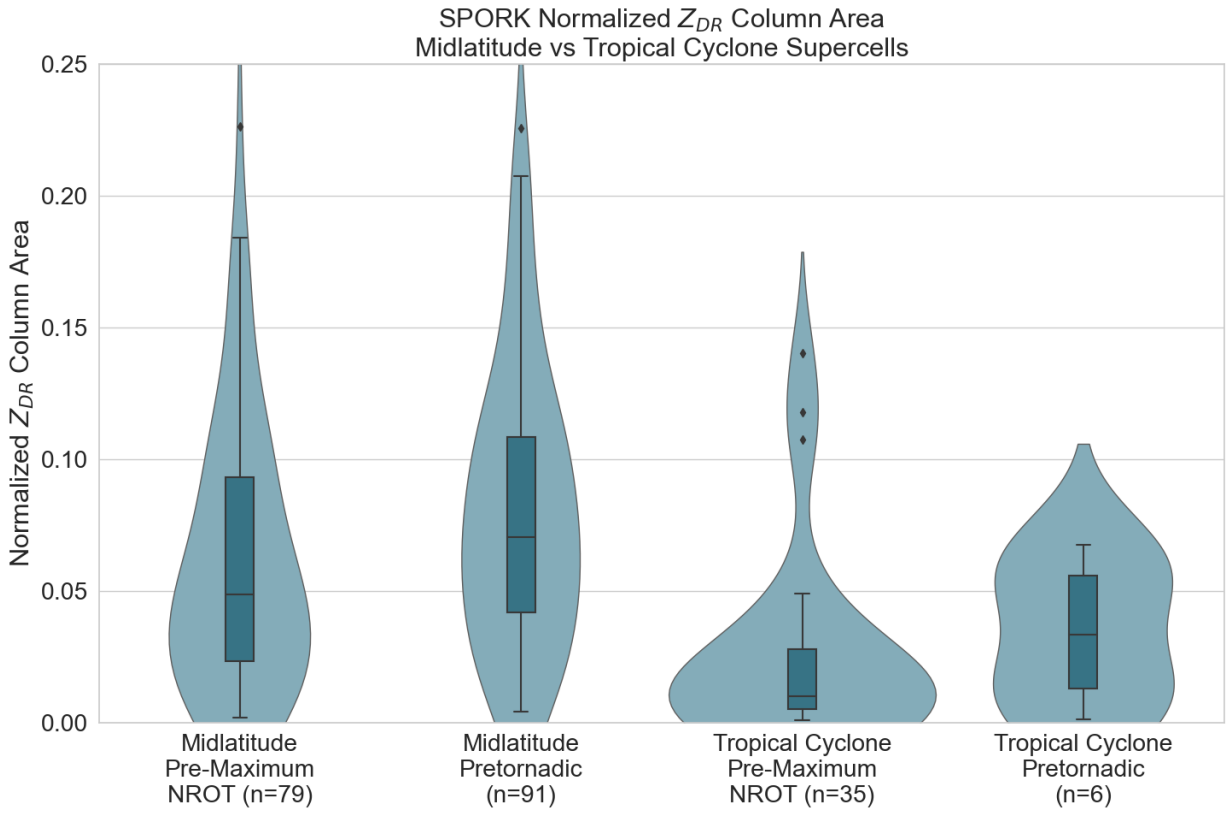

Figure 4.9. As in Fig. 4.7, but for normalized Z_{DR} column area.

Both mean and maximum Z_{DR} column depth were significantly smaller in TC cases than midlatitude cases, when only including TC cases that recorded this signature (Table 4.4). This is consistent with prior literature that TC supercells are shallower than midlatitude supercells (Edwards 2012). On average, Z_{DR} column maximum depth was nearly twice as large in midlatitude supercells than in TC supercells (Figure 4.10). More variation was seen between midlatitude and TC cases with mean Z_{DR} column depth, however midlatitude cases still remain significantly larger in both NT and PT cases ($p < 0.001$ and $p = 0.01$, respectively; Figure 4.11). These differences in Z_{DR} column area and depth support that TC supercells typically have smaller updraft in both the horizontal and vertical extent when compared to typical midlatitude supercells.

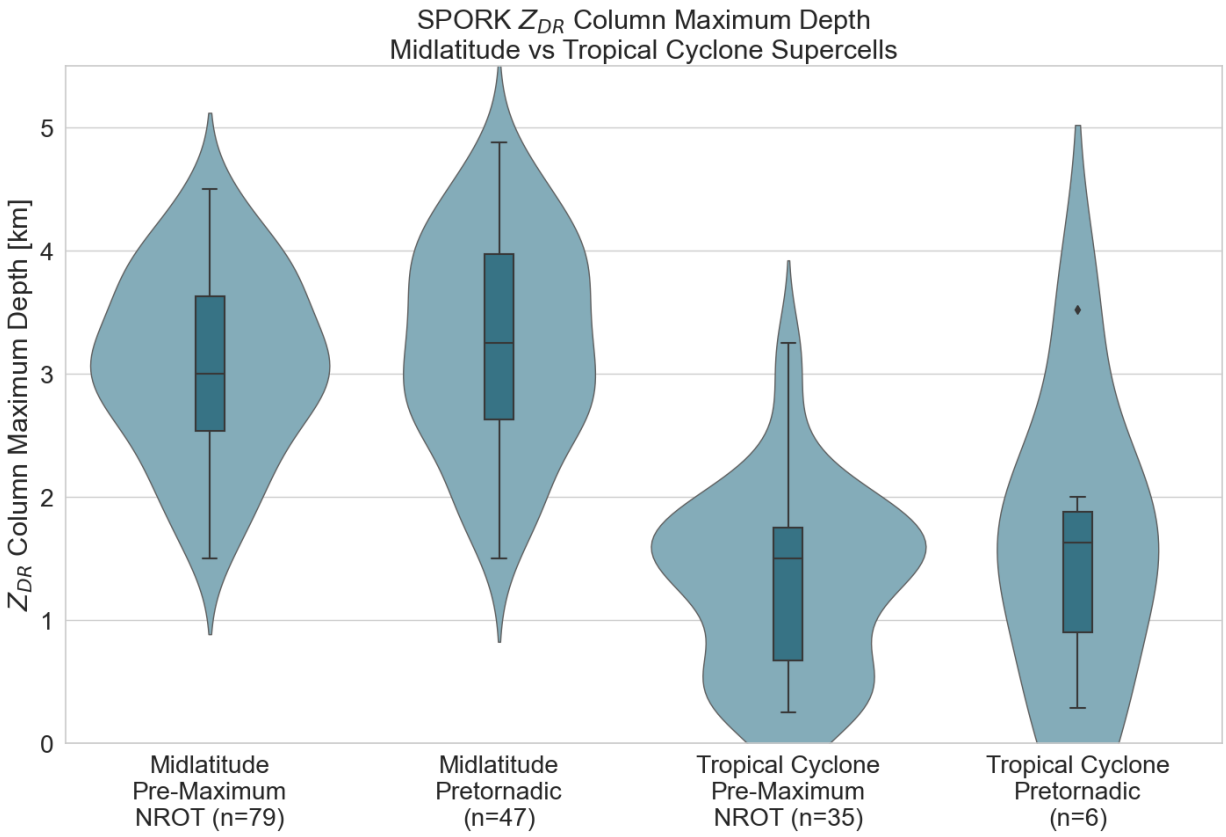

Figure 4.10. As in Fig. 4.7, but for Z_{DR} column maximum depth [km].

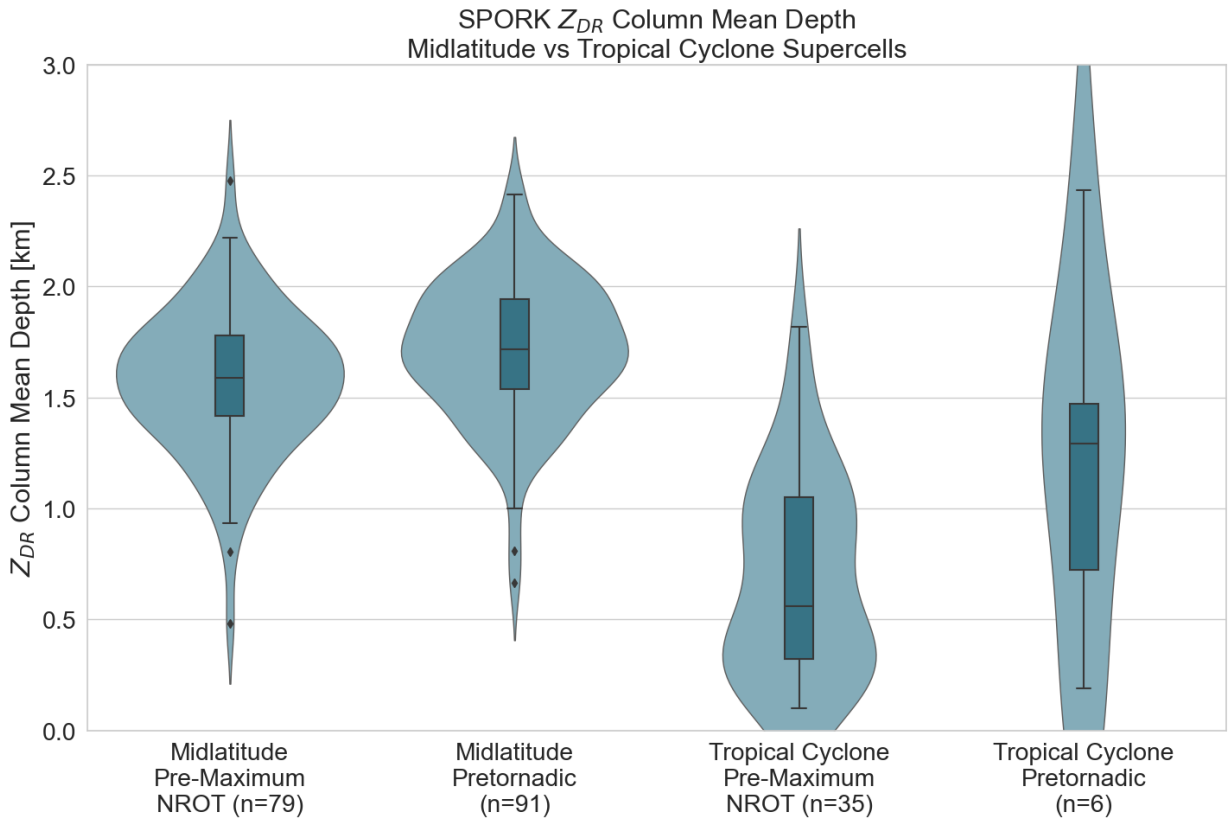

Figure 4.11. As in Fig. 4.7, but for Z_{DR} column mean depth [km].

Following suit with previous signatures, Z_{DR} arcs again appear less common in TC supercells than midlatitude supercells. In midlatitude supercells, Z_{DR} arcs appeared in 92.9% and 94.7% of NT and PT supercells, respectively. However, only 50.0% and 83.3% of NT and PT TC supercells, respectively, featured this signature. Z_{DR} arc mean and maximum values were significantly larger in TC cases than midlatitude cases (Table 4.4). Z_{DR} arc mean values in both NT and PT cases were larger in TC supercells than midlatitude supercells ($p < 0.001$ for each; Figure 4.12). This result was unexpected considering what is known about tropical drop size distributions (DSDs) when compared to midlatitude DSDs. Tropical DSDs are typically comprised of a large concentration of small drops, typically corresponding to lower Z_{DR} values (Tokay et al. 2008; Thompson et al. 2018). The increased low-level wind shear and consequently greater low-level

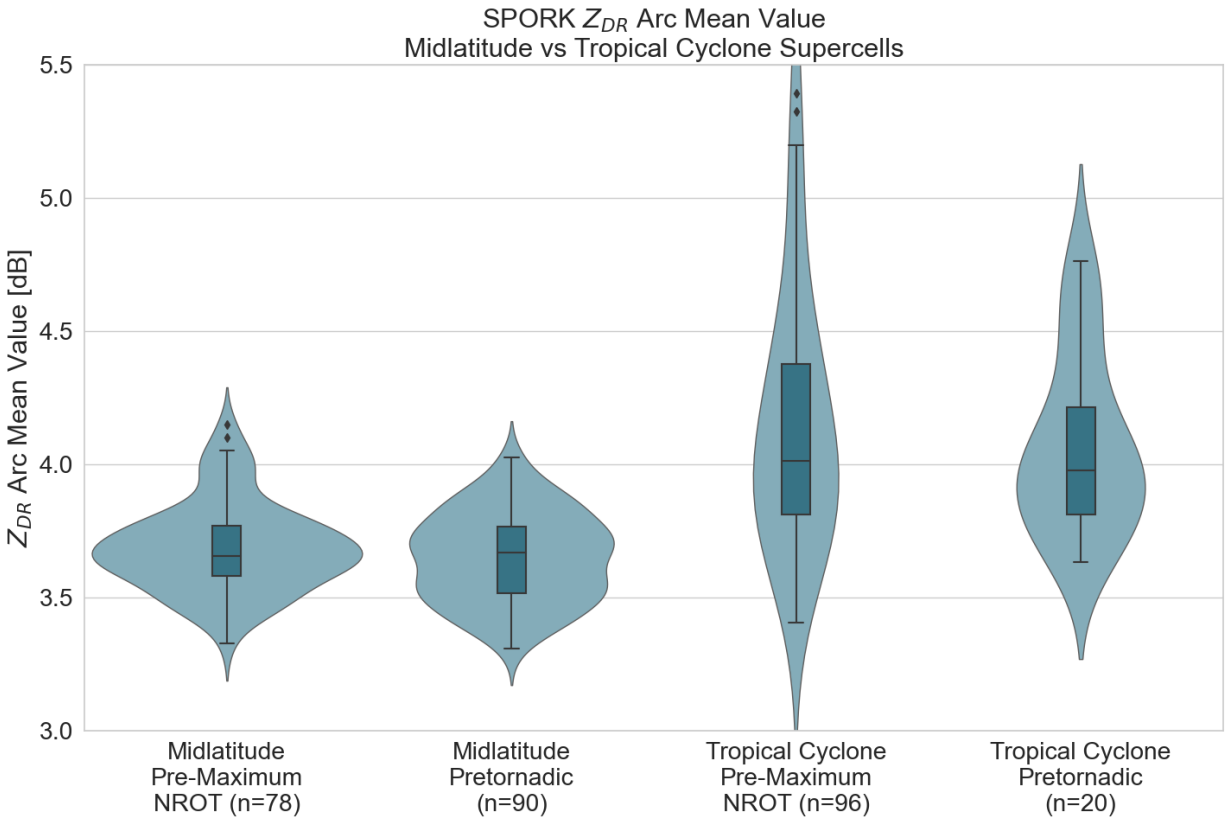

Figure 4.12. As in Fig. 4.7, but for Z_{DR} arc mean value [dB].

storm-relative inflow in TC cases may promote more effective drop size sorting (Dawson et al. 2014), resulting in higher Z_{DR} values in the Z_{DR} arc.

Differences are prominent between both K_{DP} foot and Z_{DR} arc separation angle and distance in midlatitude and TC supercells. Normalized separation distance is significantly larger in PT and weakly larger in NT TC cases than midlatitude cases (p = 0.01 and p = 0.06, respectively; Figure 4.13). Separation angle remains significantly larger in TC supercells when compared to midlatitude supercells (Figure 4.14). It is hypothesized that the increased low-level wind shear in TC environments is responsible for this larger separation distance and angle between the K_{DP} foot and Z_{DR} arc.

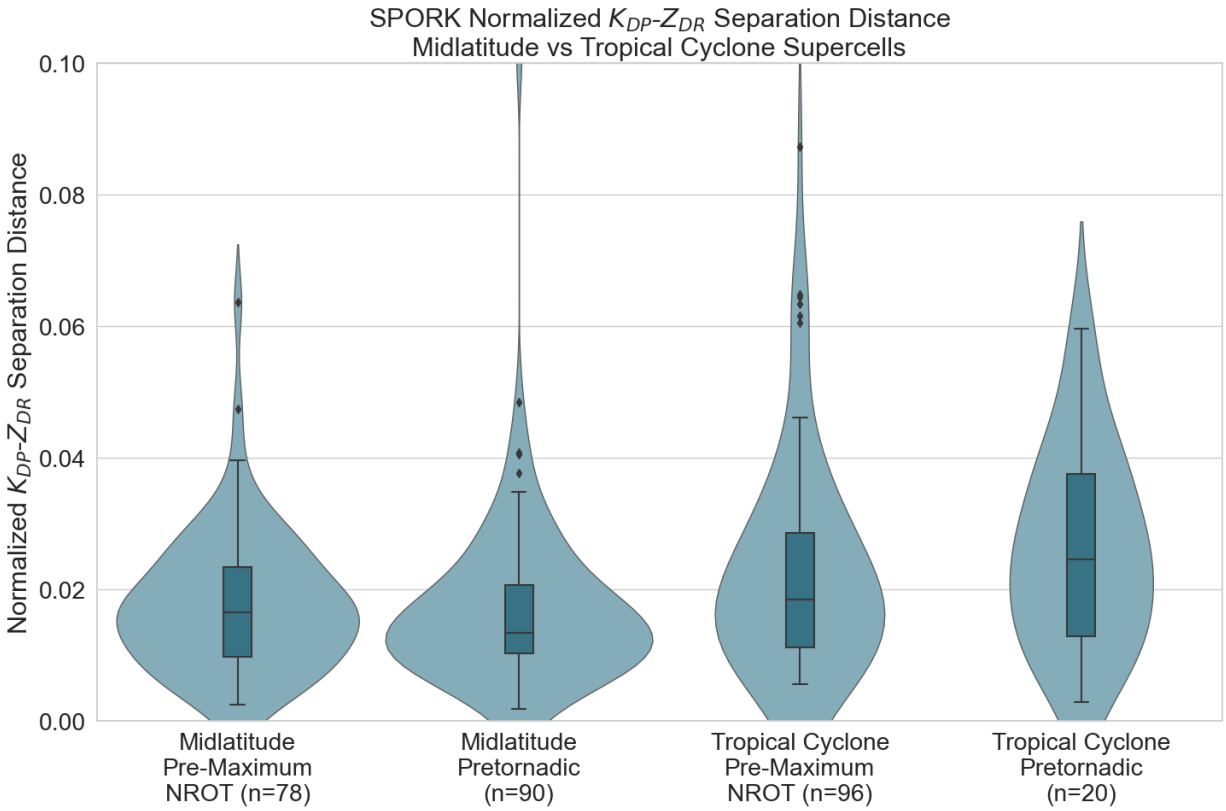

Figure 4.13. As in Fig. 4.7, but for normalized K_{DP}-Z_{DR} separation distance.

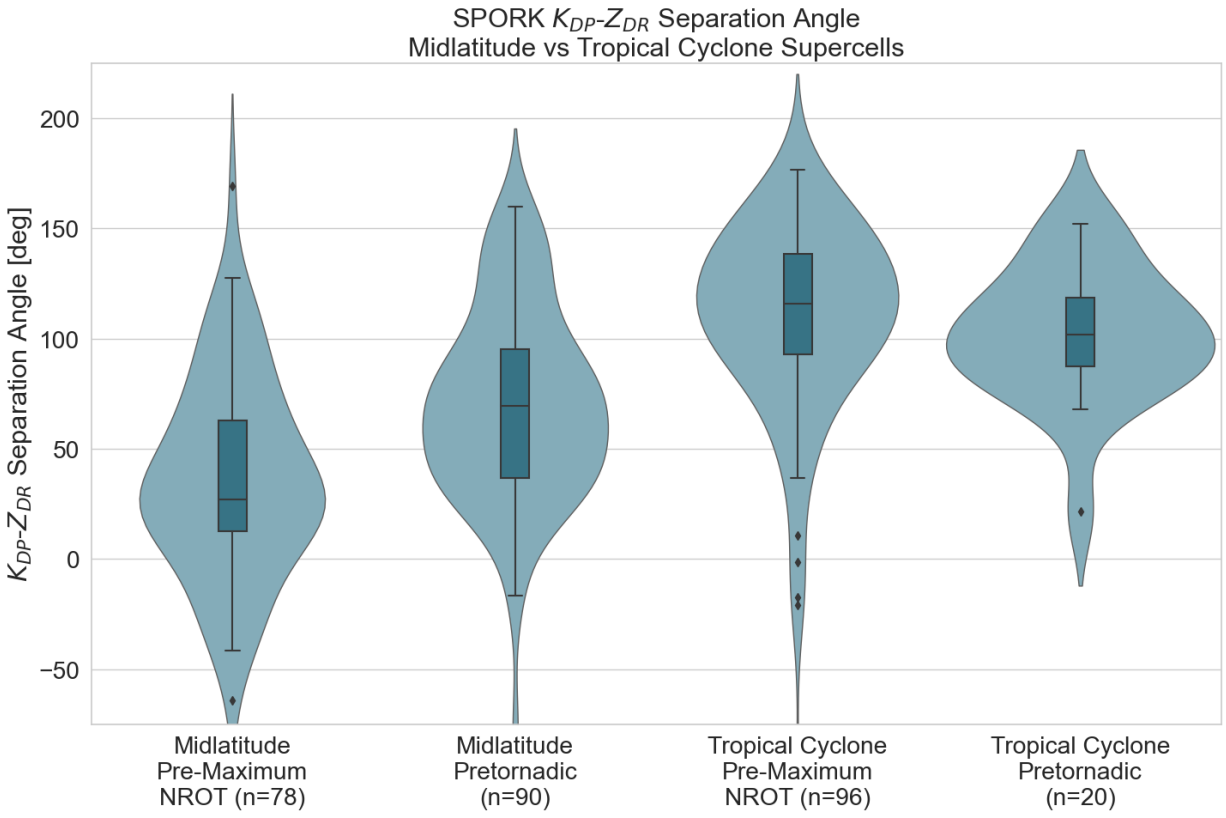

Figure 4.14. As in Fig. 4.7, but for K_{DP}-Z_{DR} separation angle [deg].

4.4 Comparison of Polarimetric Signatures between Pretornadic and Pre-Maximum NROT Supercells in Tropical Cyclones

Comparisons between SPORK polarimetric signatures in PT and NT supercells in tropical cyclones are presented here. Median values between NT and PT polarimetric signatures and their corresponding *p*-values can be found in Table 4.5. This analysis utilizes the 30 minutes prior to the first tornado report for PT cases and 30 minutes prior to the maximum NROT for NT cases. Spearman's rank-order correlations between environmental parameters and SPORK metrics have also been calculated to determine if environments play a role in SPORK metric variations (Table 4.6).

Variable	Median, Pre-Maximum NROT	Median, Pretornadic	WMW *p*-value
Hailfall Area [km^2]	0.00	0.00	0.99
Z_{DR} Column Area [km^2]	2.95	4.44	0.59
Normalized Z_{DR} Column Area	0.01	0.03	0.27
Z_{DR} Column Mean Depth [km]	0.56	1.27	0.07
Z_{DR} Column Maximum Depth [km]	1.50	1.56	0.68
Z_{DR} Arc Mean Value [dB]	4.02	3.98	0.70
Z_{DR} Arc Maximum Value [dB]	5.33	5.32	0.65
K_{DP}-Z_{DR} Separation Angle [deg]	5.25	5.18	0.41
K_{DP}-Z_{DR} Separation Distance [km]	115.89	101.93	0.18

Figure 4.5. Tropical cyclone supercell SPORK polarimetric radar metric (column 1) median values for pre-maximum NROT (column 2), pretornadic (column 3), and WMW *p* values for a comparison of the nontornadic and pretornadic distributions (column 4).

Environmental Variable	Hailfall Area	Z_{DR} Column Area	Z_{DR} Column Mean Depth	Z_{DR} Column Maximum Depth	K_{DP}-Z_{DR} Separation Distance	K_{DP}-Z_{DR} Separation Angle
LCL Height	**0.33**	**0.30**	**0.38**	0.13	0.02	-0.00
LFC Height	**0.42**	**0.32**	**0.30**	0.17	0.07	0.07
MLCAPE	0.10	-0.12	0.18	-0.12	-0.03	0.06
MUCAPE	-0.12	-0.19	0.14	-0.18	-0.01	0.08
CIN	-0.26	**-0.32**	**-0.31**	-0.28	-0.06	-0.05
Supercell Composite Parameter	0.03	0.11	0.04	0.20	-0.04	0.03
Significant Tornado Parameter	-0.02	0.11	0.06	0.24	-0.03	0.00
Freezing Level Height	-0.08	-0.03	-0.05	-0.08	0.08	0.07
Effective SRH	0.00	0.19	0.03	0.18	-0.04	0.04
0-1 km SRH	-0.12	0.27	0.03	0.24	0.03	0.03
0-3 km SRH	0.00	**0.33**	0.08	**0.32**	0.01	0.06
0-1 km Shear	**0.36**	0.14	-0.04	0.27	-0.13	0.18
0-3 km Shear	-0.07	**0.34**	0.8	**0.41**	-0.07	0.13
0-6 km Shear	0.12	0.04	-0.16	0.01	-0.03	-0.24

Table 4.6. Spearman's rank-order correlations between uncontaminated RAP sounding environmental parameters and both NT and PT TC SPORK dual-polarimetric variables. Correlations ≥ 0.30 are bolded.

Neither NT nor PT cases typically experienced hailfall surviving to base scan, with median values equal to zero in both (Figure 4.15). This result is consistent with our hypothesis and is likely a result of the high freezing levels and RH throughout the depth of TC supercells, inhibiting both the production and survival of hail. Additional analysis was done to determine if freezing level height was the discerning factor between TC supercells with and without hailfall area (Figure 4.16). Freezing level heights were not significantly larger for TC supercells with hailfall area when compared to those without (p = 0.23). Spearman's rank order correlation coefficient showed low correlation between hailfall area and both LCL and LFC height as cases with hailfall experienced larger LCL and LFC heights (r = 0.33 and r = 0.42, respectively; Table 4.6).

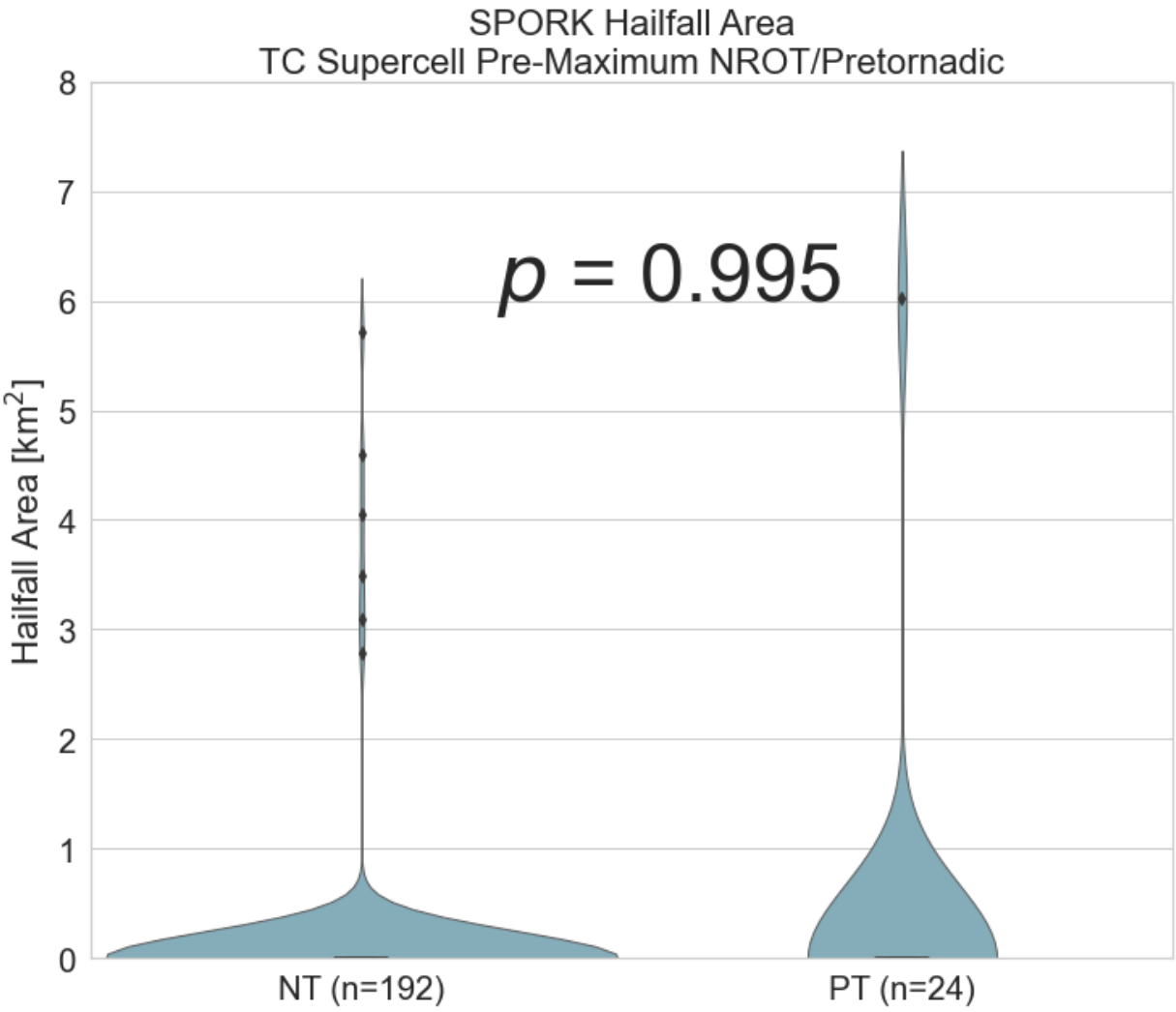

Figure 4.15. Violin plots displaying the distribution of median hailfall area [km^2] for pre-maximum NROT (left) and pretornadic (right) TC supercells. Values are valid for 30 minutes prior to the maximum NROT and first tornado report. The number of samples contributing to each violin are indicated on the axis labels. Box and whisker plots are embedded in violin plots with boxes displaying the 25^{th} and 75^{th} percentile and the black horizontal line indicating the median value. Whiskers convey the 10^{th} and 90^{th} percentile with the outliers represented by black diamonds.

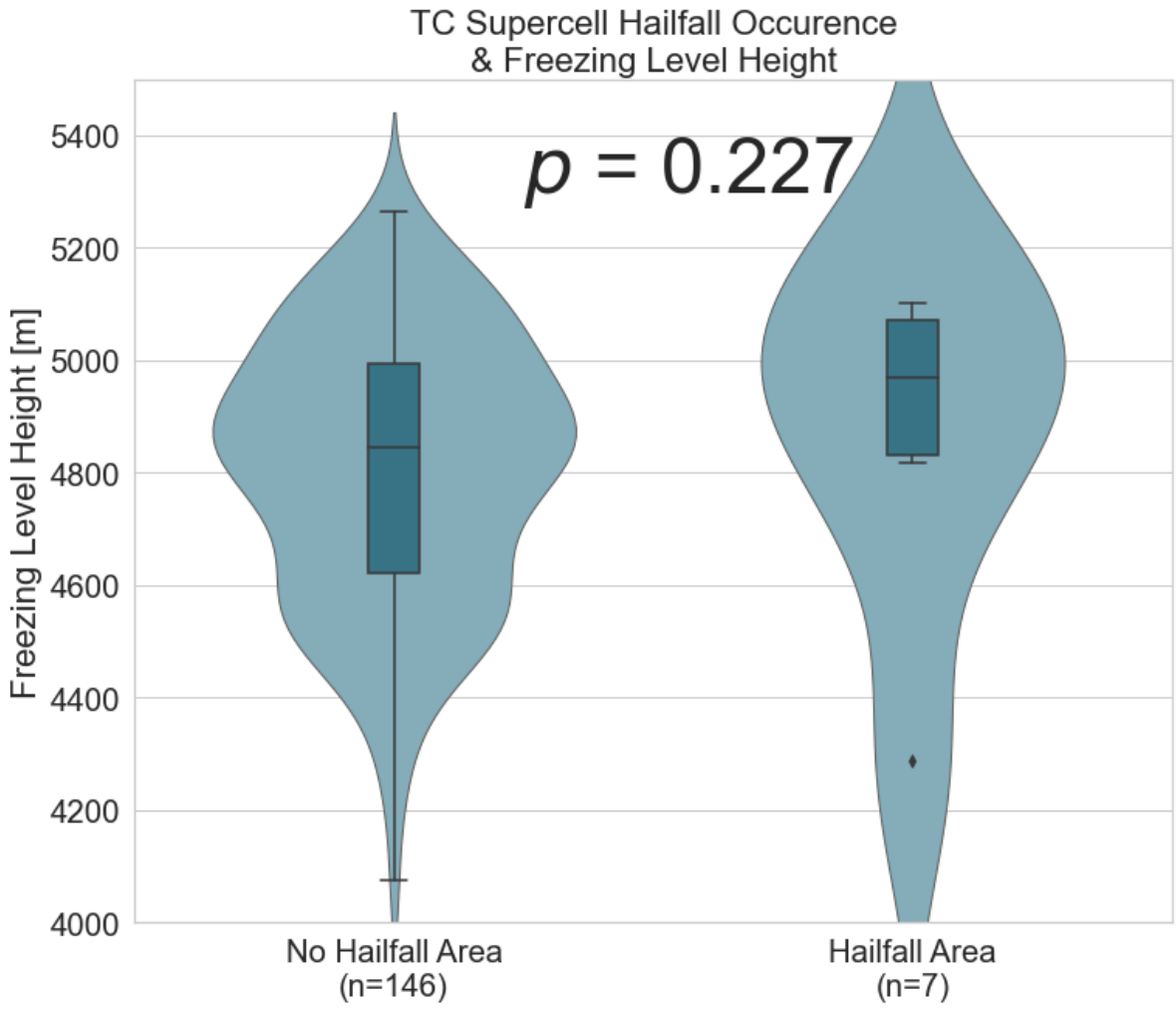

Figure 4.16. As in Fig. 4.15, but for non-contaminated freezing level height [m] for TC supercells with no hailfall area (left) and with hailfall area (right).

Neither Z_{DR} column area (Figure 4.17) nor normalized Z_{DR} column area displayed significant differences between NT and PT supercells ($p = 0.59$ and $p = 0.27$, respectively). Median values of Z_{DR} column mean depth were slightly larger in PT cases when compared to NT cases ($p = 0.07$; Figure 4.18). However, maximum Z_{DR} column depth was similar between NT and PT cases ($p = 0.68$). These results indicate that Z_{DR} column area and depth in TC supercells may not be an indication of tornadic potential.

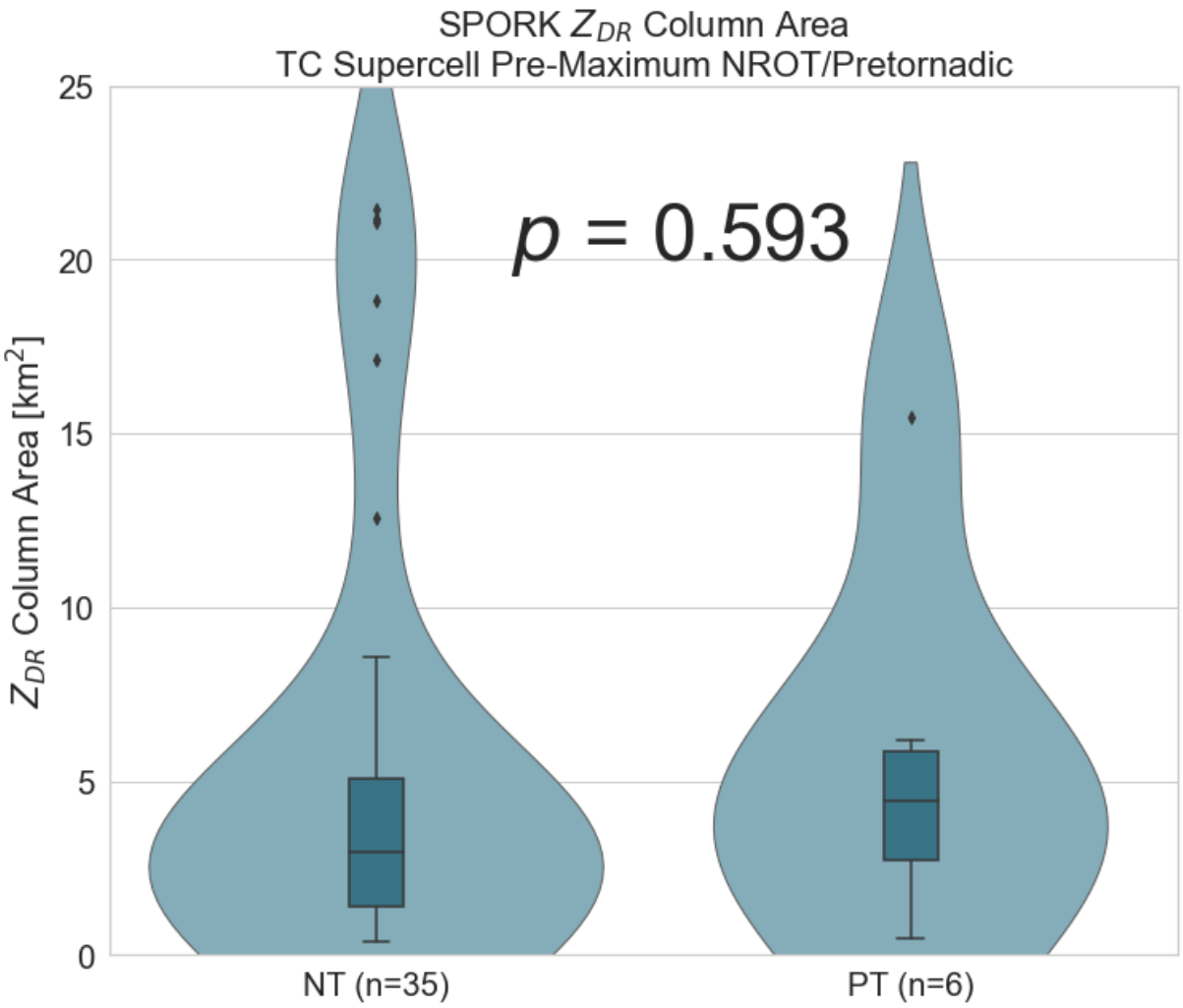

Figure 4.17. As in Fig. 4.15, but for Z_{DR} column area [km^2].

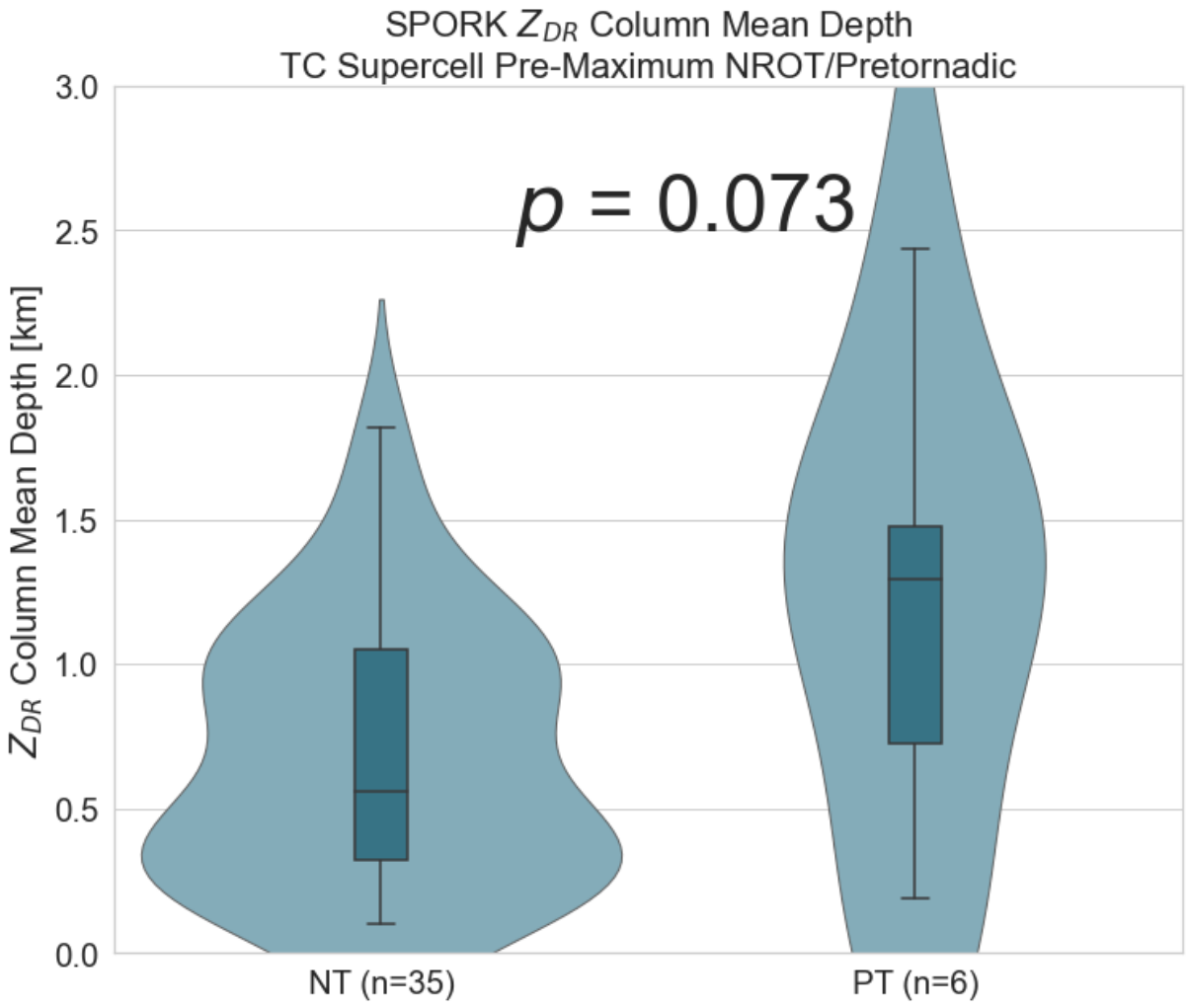

Figure 4.18. As in Fig. 4.15, but for Z_{DR} column mean depth [km].

The lack of Z_{DR} column signatures in TC cases (18.2% of NT cases, 25.0% of PT cases) warrants further investigation. Z_{DR} columns are defined as areas of positive Z_{DR} values above the environmental freezing level that occur as updrafts loft raindrops and/or water-coated ice particles above the freezing level (Kumjian et al. 2014; Snyder et al. 2015; Wilson and Van Den Broeke 2022). A combination of the shallow vertical depth and high freezing levels in TC environments may provide evidence as to why these signatures occur infrequently in TC cases. Analysis between the freezing level height of TC cases that recorded Z_{DR} columns signatures compared to those without displayed no significant differences ($p = 0.88$; Figure 4.19). Spearman's rank order correlation coefficient showed low correlation between Z_{DR} column area and mean depth with both LCL and LFC height as higher heights are seen with larger Z_{DR} column area and depth ($r = 0.30$ and $r = 0.32$ for Z_{DR} column area, $r = 0.38$ and $r = 0.30$ for Z_{DR} column mean depth, respectively; Table 4.6). No correlation was found between Z_{DR} column area and depth with either MUCAPE or MLCAPE. This contrasts with the findings of Wilson and Van Den Broeke (2022) who found that Z_{DR} column area and depth have a moderate positive correlation with both MUCAPE and MLCAPE in midlatitude supercells.

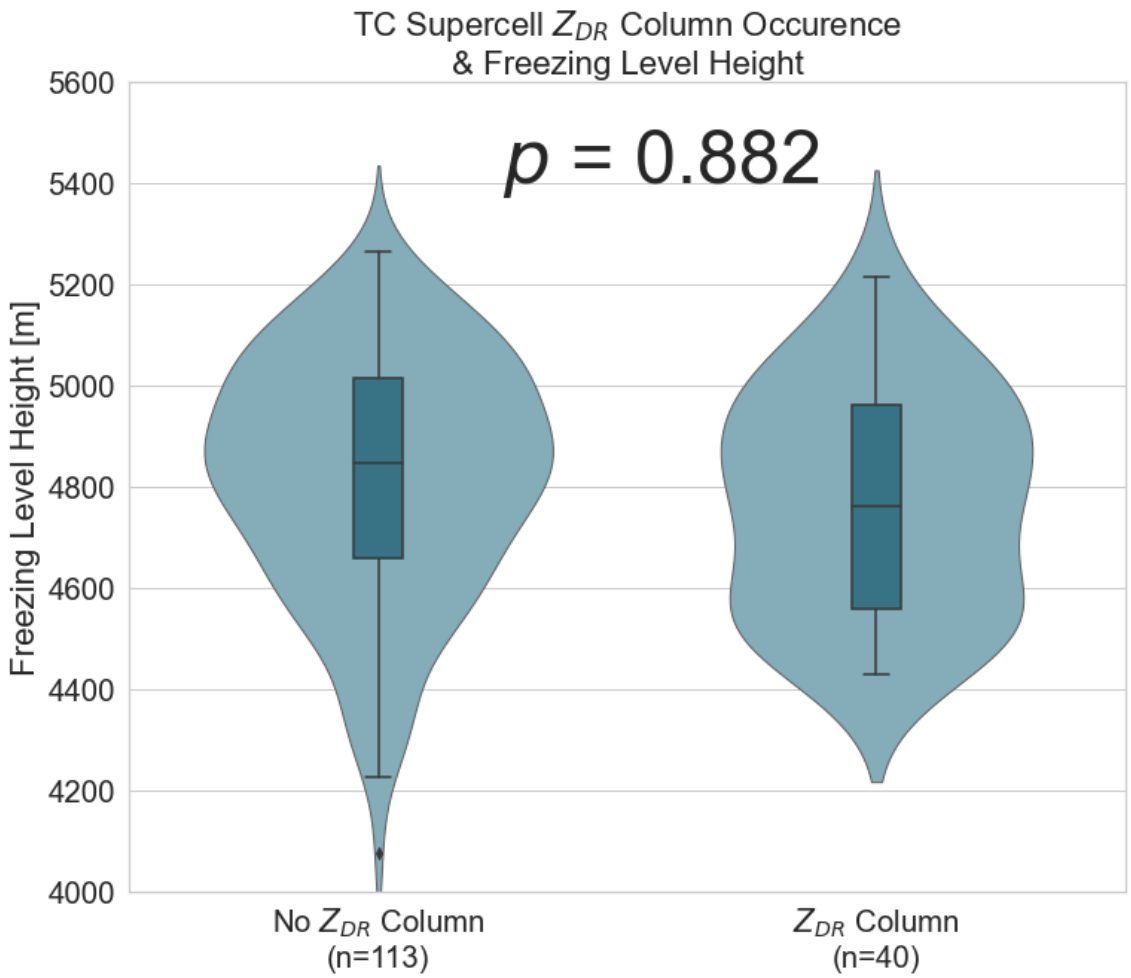

Figure 4.19. As in Fig. 4.15, but for non-contaminated freezing level height [m] for TC supercells with no Z_{DR} columns (left) and with Z_{DR} columns (right).

Z_{DR} arc maximum and mean values also remained similar between pretornadic and pre-maximum NROT cases (p = 0.65 and p = 0.70, respectively). This result concurs with our hypothesis that Z_{DR} arcs will remain pronounced in TC cases, however they may not be used to help distinguish tornadic potential. This result disagrees with prior work using a smaller sample size that found a larger Z_{DR} arc magnitude in tornadic TC supercells (Crowe et al. 2010).

Median values of separation distance between the K_{DP} foot and Z_{DR} arc remained at approximately 5 km in both NT and PT cases (Figure 4.20). No significant difference in separation distance was observed between NT and PT cases (p = 0.41). Separation angle between the K_{DP} foot and Z_{DR} arc remained large in TC cases, with median values over 100 degrees in both NT and PT cases (Figure 4.21). There are again no significant differences in the K_{DP}-Z_{DR} separation angle between NT and PT cases (p = 0.18). These results reject our hypothesis that K_{DP}-Z_{DR} separation distance will be larger in PT cases and help to distinguish tornadic potential in TC supercells. No correlation was found between either K_{DP}-Z_{DR} separation distance and angle and the 0-1 km shear or 0-3 km shear (Table 4.6).

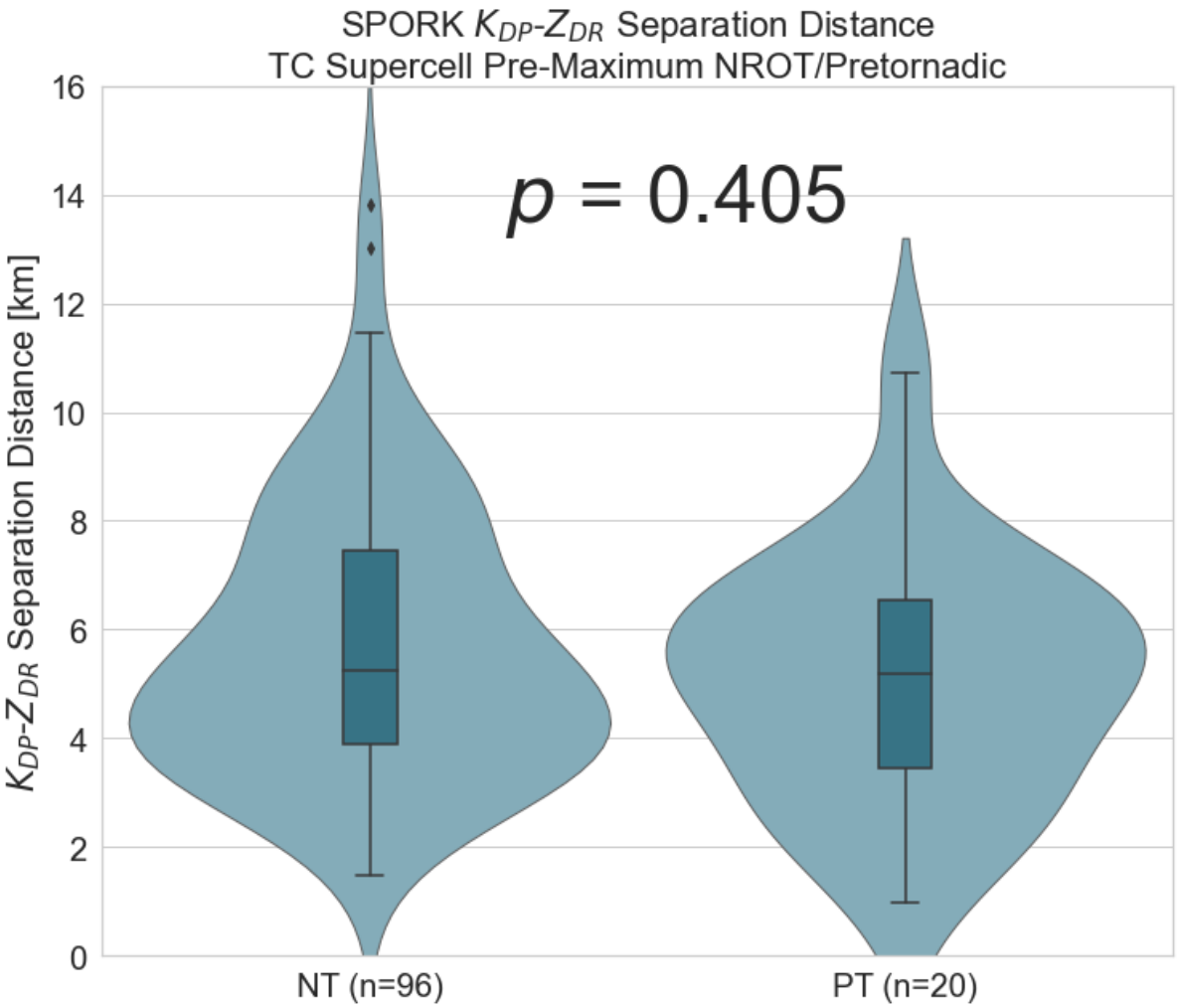

Figure 4.20. As in Fig. 4.15, but for K_{DP}-Z_{DR} separation distance [km].

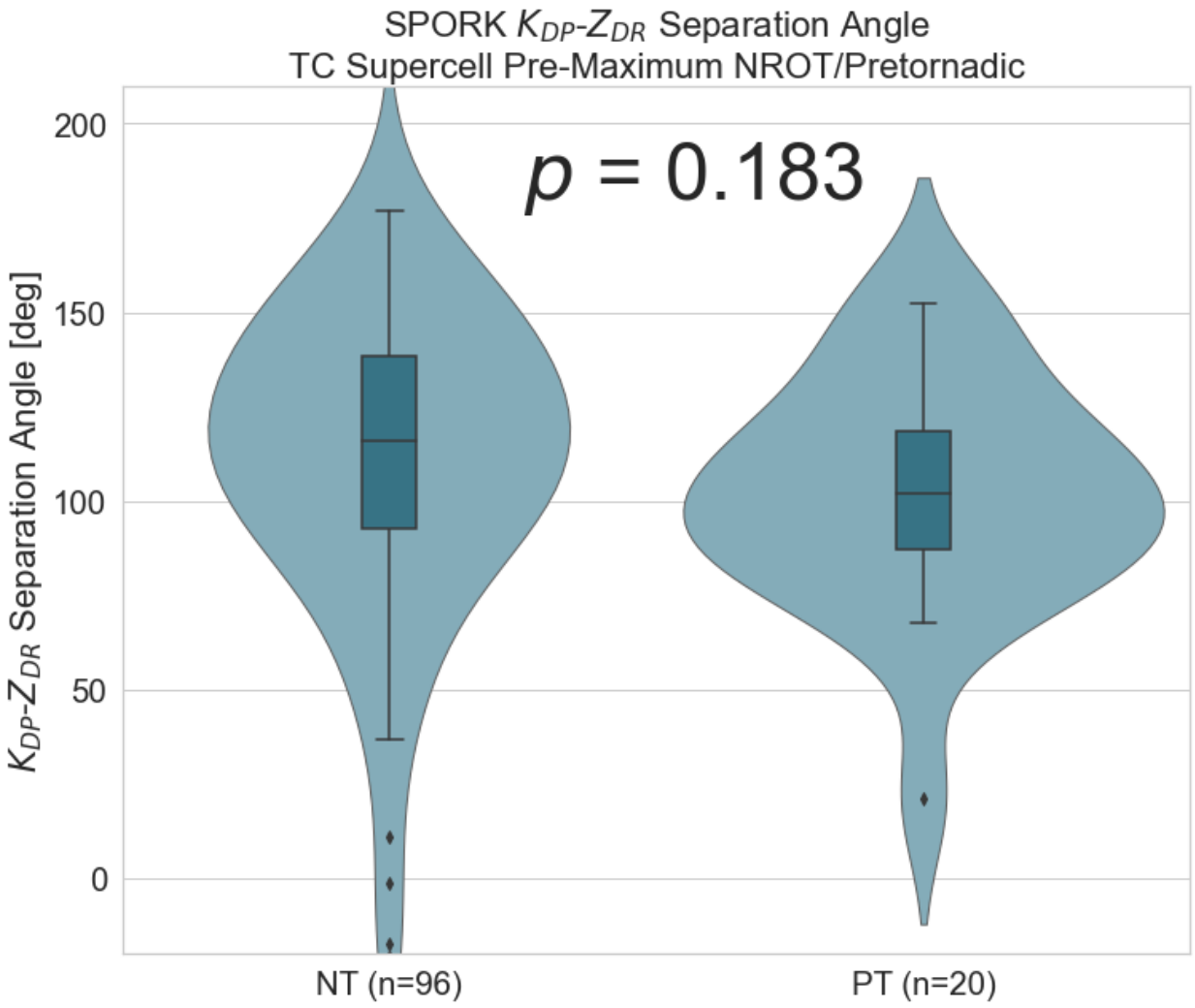

Figure 4.21. As in Fig. 4.15, but for K_{DP}-Z_{DR} separation angle [deg].

4.5 Comparison of Mesocyclone Strength between Tornadic and Nontornadic Supercells in Tropical Cyclones

Maximum NROT values can be used as a proxy for low-level mesocyclone strength (Turnage 2014; Cooper and Vorst 2016). Before comparing maximum NROT values between tornadic and nontornadic TC supercells, maximum NROT values were correlated against distance from the radar. Also, since the maximum NROT value could occur at different elevation angles for different storms, the radar and elevation altitude of the maximum NROT value was also correlated against magnitude of the NROT maximum. For both tornadic and nontornadic cases, low Pearson's correlation was found between NROT values and distance from the radar ($r = 0.05$ and $r = 0.02$, respectively; Figure 4.22). Low correlation was found between NROT values and elevation for both tornadic and nontornadic cases ($r = 0.28$ and $r = 0.35$, respectively; Figure 4.23), explaining approximately 10% of the variation in NROT values. Through this analysis, it was determined that NROT values were not strongly correlated with distance from the radar and elevation, and therefore were a justifiable proxy for low-level mesocyclone strength.

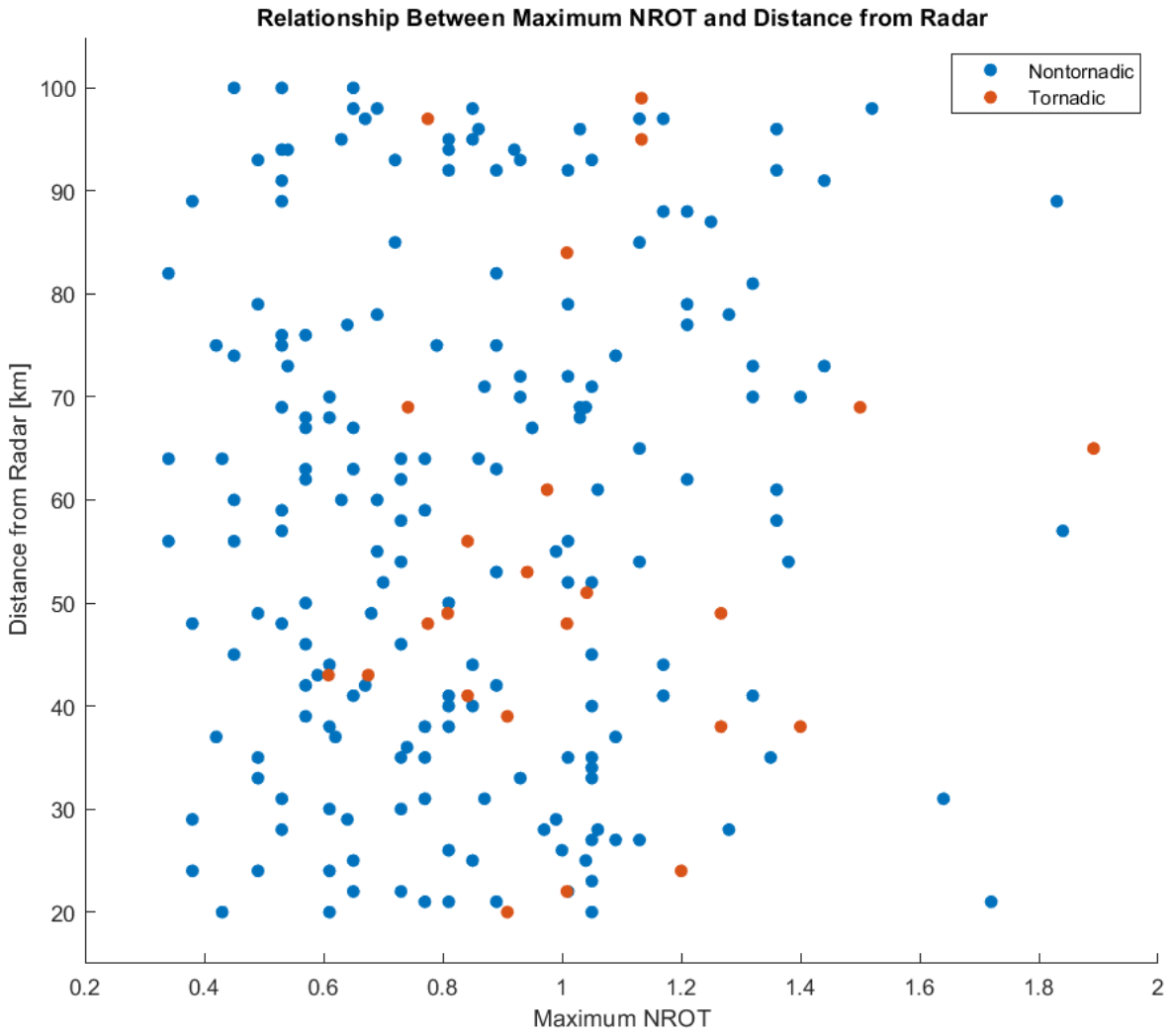

Figure 4.22. Scatterplot displaying the lack of relationship between the maximum NROT value in TC nontornadic (blue) and tornadic (orange) supercells and distance from the radar (r = 0.022 for nontornadic supercells, r = 0.044 for tornadic supercells).

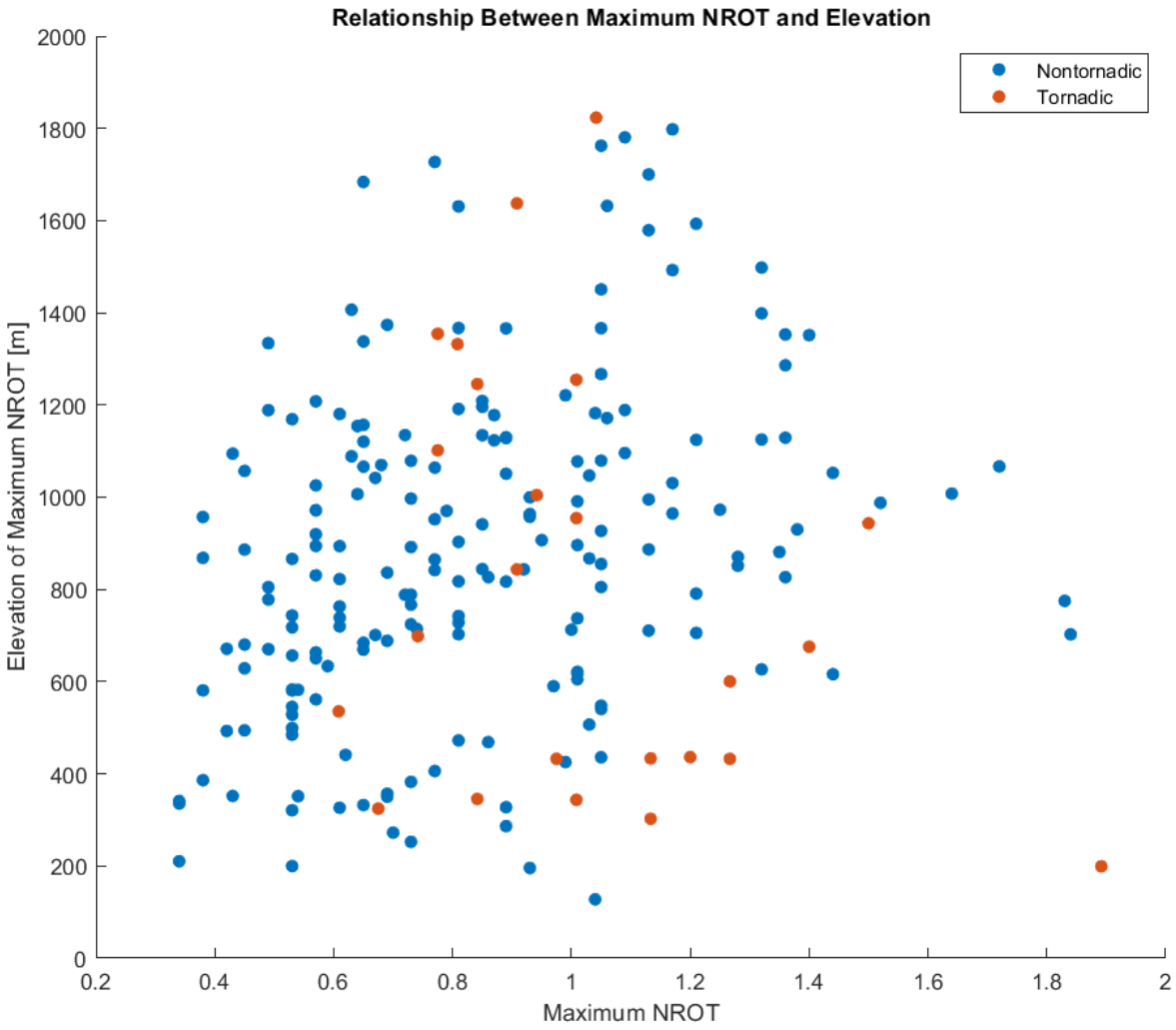

Figure 4.23. Scatterplot displaying the weak relationship between the maximum NROT value in TC nontornadic (blue) and tornadic (orange) supercells and elevation of the maximum NROT (r = 0.351 for nontornadic supercells, r = 0.275 for tornadic supercells).

Maximum NROT values were obtained for all 192 nontornadic and 24 tornadic TC supercells. These values were obtained from the time of peak NROT for nontornadic cases or the time closest to the first tornado report for tornadic cases. Maximum NROT values for supercells within approximately < 10-15 km of a radar can make the process of obtaining and interpreting NROT values difficult. These NROT values would be discarded, however this scenario did not apply to any of our cases. When analyzing the maximum NROT values in nontornadic and tornadic TC supercells, tornadic TC supercells had significantly larger maximum NROT values (p = 0.01; Figure 4.24). The median NROT value for nontornadic TC supercells was 0.810, while this value increased to 0.992 for tornadic cases. This result is not surprising given that prior literature indicates that tornadic mesocyclones are stronger than nontornadic mesocyclones in TC cases (Schneider and Sharp 2007; Martinaitis 2017).

The increased mesocyclone strength in tornadic TC supercells prompted an additional investigation into the distance of tornado reports from the coastline. The importance of the water-to-land transition has been emphasized in past research by Novlan and Grey (1974) and Gentry (1983) as frictional effects increase tornado-favorable ingredients such as low-level wind shear and convergence near the coast. In this dataset, 23 of the 24 tornado reports were located within 100 km of the coast (Figure 4.25).

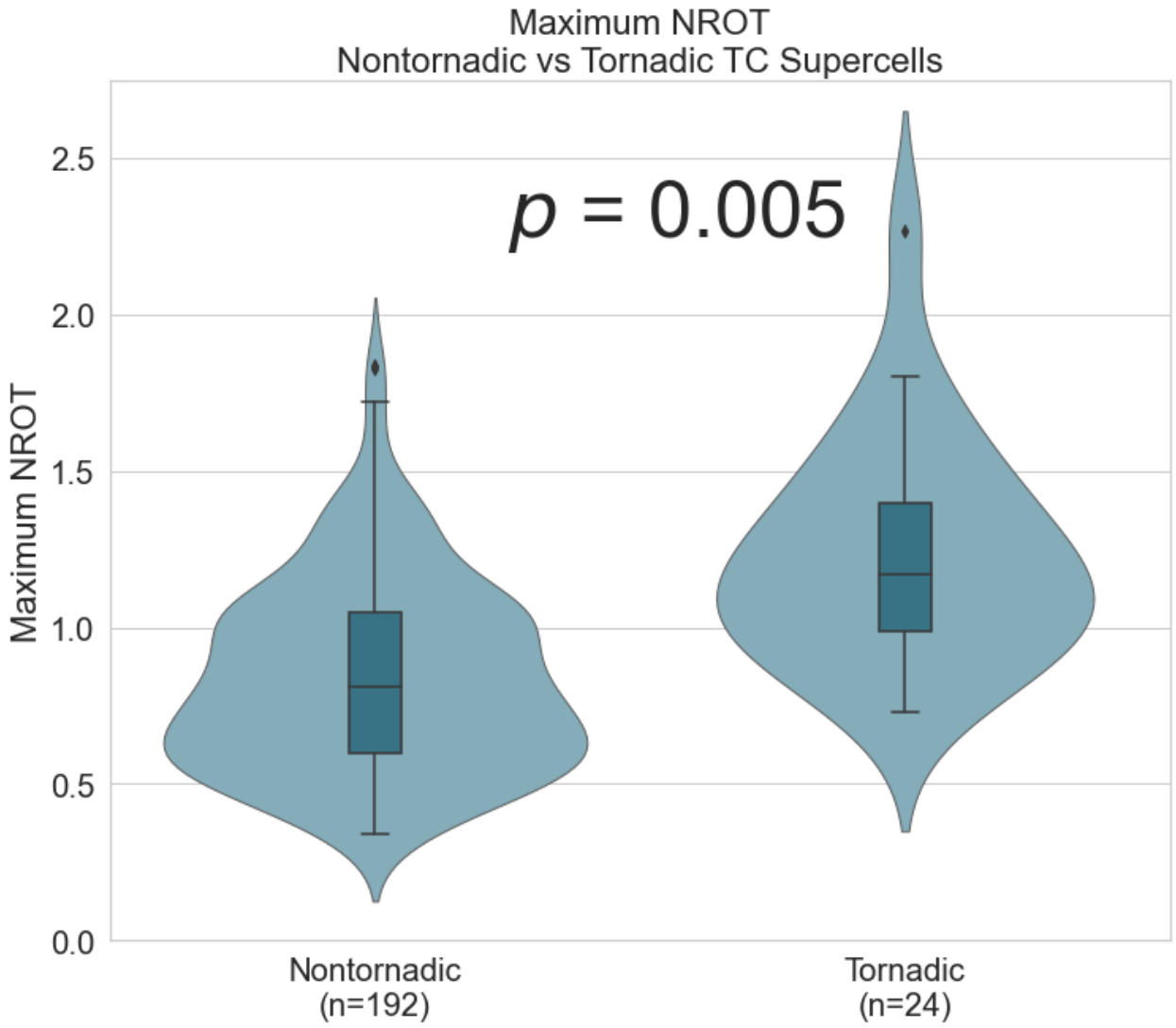

Figure 4.24. As in Figure 4.15, but for maximum NROT values from nontornadic (left) and tornadic (right) TC supercells.

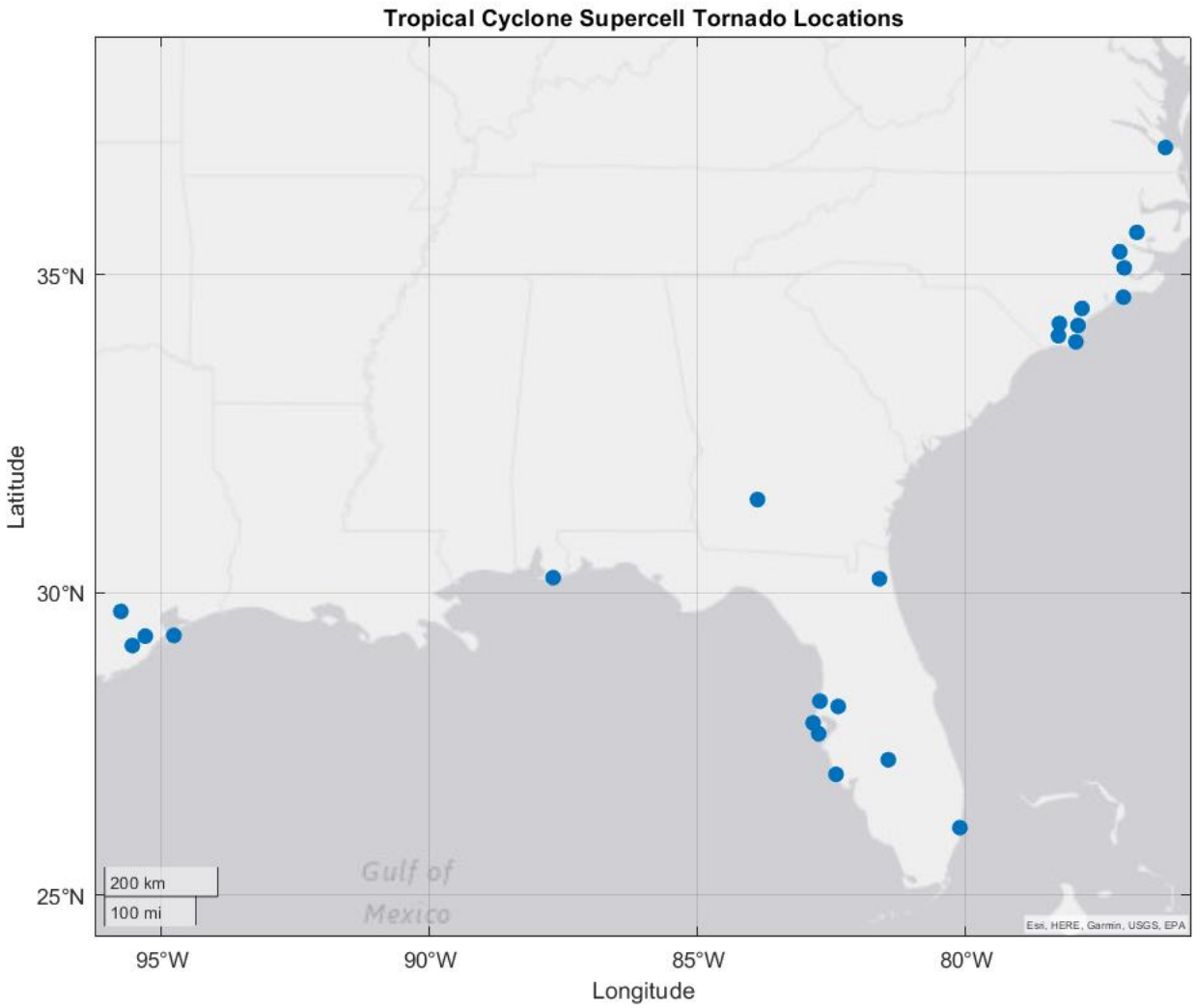

Figure 4.25. Starting locations of all 24 tornadoes associated with TC supercells. If a TC supercell was associated with multiple tornado reports, only the first report was plotted.

Chapter V: Discussion and Conclusion

Establishing differences in dual-polarimetric signatures between the well-established midlatitude and research-lacking TC supercells is important for the understanding and interpretation of these signatures in TC supercells. An understanding of these signatures can give valuable insight into the size sorting processes and tornadic potential of these supercells. Our hypotheses regarding these dual-polarimetric signatures and their differences include:

- TC supercells will have shallower Z_{DR} columns than midlatitude supercells. However, Z_{DR} column area and depth will behave similarly between tornadic and nontornadic TC supercells.
- Tornadic TC supercells will have stronger mesocyclones than nontornadic TC supercells.
- Z_{DR} arcs will remain pronounced in TC supercells.
- TC supercells will have an increased separation angle and normalized separation distance between the K_{DP} foot and Z_{DR} arc when compared to midlatitude supercells.
- TC supercells will have relatively little, if any, hailfall surviving to the base scan.

Results from this study related to these hypotheses were as follows:

- Z_{DR} columns remained shallower in TC supercells when compared to their midlatitude counterparts, with an average depth half the size of midlatitude cases. The occurrence of Z_{DR} columns was also much rarer in TC cases than midlatitude

cases. No significant differences were found in Z_{DR} column area, mean depth, or maximum depth between pretornadic and pre-maximum NROT TC supercells.

- Tornadic TC supercells had significantly larger NROT values than nontornadic TC supercells.
- Z_{DR} arcs occurred less in TC cases than midlatitude cases. However, both Z_{DR} arc maximum and mean values were significantly larger in TC cases than midlatitude cases.
- TC cases had a larger normalized separation distance between the K_{DP} foot and Z_{DR} arc, and separation angle was significantly larger in TC cases. There was no significant difference between separation distance or angle between pretornadic and pre-maximum NROT TC supercells.
- Neither pretornadic nor pre-maximum NROT TC supercells typically experienced hailfall surviving to base scan.

Dual-polarimetric signatures showed extensive differences between midlatitude and TC supercells. Operational meteorologists who utilize dual-polarimetric signatures in midlatitude cases should be aware of these differences when making warning decisions in TC cases. The absence of Z_{DR} columns in the majority of TC cases makes this signature an unreliable proxy for updraft characteristics. This absence is likely due to a combination of the high environmental freezing level and shallower depth of TC supercells, making the presence of raindrops or water-coated ice particles being lofted above the freezing level a rare occurrence (Kumjian et al. 2014; Snyder et al. 2015; Wilson and Van Den Broeke 2022). The increased ground-relative velocity of TC supercells could also cause the storm to have an unrepresentative tilted appearance

between radar scans at different elevation angles, minimizing the ability to detect Z_{DR} columns. In TC cases where Z_{DR} columns are present, the signature is shallow and shows little variation in area or depth with time. Therefore, this signature does not appear to give an indication of a TC supercell's tornadic potential or cyclic activity as it can in midlatitude cases (Kuster et al. 2020; Sessa and Trapp 2020; Van Den Broeke 2020).

A key result from this study is the difference in low-level mesocyclone strength between tornadic and nontornadic TC supercells. Tornadic TC supercells had significantly larger NROT values than nontornadic TC supercells, indicating that tornadic TC supercells typically have stronger mesocyclones than nontornadic supercells. This agrees with both Schneider and Sharp (2007) and Martinaitis (2017) who detected stronger mesocyclones in tornadic TC supercells than nontornadic cases. With additional work, this result may be important for operational meteorologists when gauging tornadic potential in TC supercells.

Not only are Z_{DR} arcs present in most TC supercells, but mean and maximum Z_{DR} values within this signature were typically larger than those of their midlatitude counterparts. The enhancement of this signature in TC cases leads to the inference that more effective drop size sorting is taking place in TC supercells. This effective drop size sorting is likely due to the increased low-level wind shear in TC environments (Conway and Zrnić 1993; Dawson et al. 2014). While the presence of this signature indicates the size sorting mechanisms occurring in TC supercells, neither the mean nor maximum values within the signature gave insight into the tornadic potential of a supercell. This finding contrasts with Crowe et al. (2010) who observed larger Z_{DR} arc values in tornadic TC supercells than nontornadic supercells in Hurricane Rita (2005).

Separation angle between the K_{DP} foot and Z_{DR} arc are significantly larger in TC cases than midlatitude cases. As previously mentioned, this is likely due to the increased low-level wind shear in TC cases promoting more effective size sorting processes (Crowe et al 2010; Loeffler and Kumjian 2018). While the separation angle between the K_{DP} foot and Z_{DR} arc appeared larger in TC cases, normalized separation distance was still larger in midaltitude cases. Rejecting the hypothesis, there were no differences in separation distance or angle between the K_{DP} foot and Z_{DR} arc between tornadic and nontornadic TC supercells. This result contrasts with that of Crowe et al. (2010) and Martinaitis (2017) who observed a larger separation distance between the K_{DP} foot and Z_{DR} arc in tornadic TC supercells.

In agreement with our hypothesis, neither tornadic nor nontornatic TC supercells typically experienced hailfall surviving to base scan. This is likely due to a combination of the shallow depth of these storms and the high environmental freezing level and is consistent with Wilson and Van Den Broeke (2022) who found a moderate negative correlation between hailfall area and freezing level height. The decreased environmental lapse rate would also make it difficult for any hail to survive to the base scan.

Loeffler and Kumjian (2018) hypothesized that the separation distance between the K_{DP} foot and Z_{DR} arc would be enhanced with a strengthening updraft and therefore increased low-level storm-relative inflow. However, the results of this study found stronger mesocyclones in tornadic cases but no differences in any signature related to size sorting processes. While 23 out of the 24 tornadic TC cases occurred within 100 km of the coast, it is possible that the frictional effects from the water-to-land transition increased the low-level wind shear and convergence in these cases, therefore increasing

tornado favorable ingredients (Novlan and Grey 1974; Gentry 1983; McCaul and Weisman 1996). With these processes taking place on a short time scale as TC supercells enter the water-to-land transition phase, it is possible that additional size sorting effects from a mesocyclone increasing in strength is not captured in the time span between radar scans. A similar effect may also be possible in cases that interact with small scale orographic features or baroclinic boundaries (Markowski et al. 1998; Knupp et al 2006). With the shallow depth of these storms, it is also possible that the radar beam height is above the level at which these processes are taking place, even within the 100 km range from the radar to be included in this study. Operational meteorologists should pay attention to TC supercells as they transition from water-to-land for any signs of increasing mesocyclone strength as tornadic production could be quick and without prior indication from other dual-polarimetric signatures.

Future work should focus on differences in dual-polarimetric signatures between tornadic and nontornadic TC supercells with a larger sample size of tornadic cases to improve statistical robustness. Observing mesocyclone strength throughout interactions with the coastline and baroclinic boundaries may also be beneficial. Attention should also be focused on radar signatures as a function of supercell distance from the TC center since supercells farther from the TC center have more of a dependence on the ambient environment (Schultz and Cecil 2009). Additional work should also be done to better understand and predict small scale inhomogeneity in environmental variables such as SRH and 0-1 km shear in TC environments.

References

Blumberg, W. G., K. T. Halbert, T. A. Supinie, P. T. Marsh, R. L Thompson, and J. A. Hart, 2017: SHARPpy: An open-source sounding analysis toolkit for the atmospheric sciences. *Bull. Amer. Meteor. Soc.*, **98**, 1625–1636, https://doi.org/10.1175/BAMS-D-15- 00309.1.

Bodine, D. J., Kumjian, M. R., Palmer, R. D., Heinselman, P. L., and Ryzhkov, A. V., 2013: Tornado damage estimation using polarimetric radar. *Wea. Forecasting*, **28,** 139-158, https://doi.org/10.1175/WAF-D-11-00158.1.

Brandes, E. A., Ryzhkov, A. V., and Zrnić, D. S., 2001: An evaluation of radar rainfall estimates from specific differential phase. *J. Atmos. Oceanic Technol.*, **18**, 363-375, https://doi.org/10.1175/1520-0426(2001)018<0363:AEORRE>2.0.CO;2.

Browning, K. A., 1962: Cellular structure of convective storms. *Meteor. Mag*., **91**, 341-350.

— —, 1964: Airflow and precipitation trajectories within severe local storms which travel to the right of the winds. *J. Atmos. Sci.*, **21**, 634-639, https://doi.org/10.1175/1520-0469(1964)0212.0.CO;2.

— —, 1965. Some inferences about the updraft within a severe local storm. *J. Atmos. Sci.* **22**, 669–678.

Bunkers, M. J., Klimowski, B. A., Zeitler, J. W., Thompson, R. L., and Weisman, M. L., 2000: Predicting supercell motion using a new hodograph technique. *Wea. Forecasting*, **15,** 61-79, https://doi.org/10.1175/1520-0434(2000)015<0061:PSMUAN>2.0.CO;2.

Burgess, D.W., and L. R. Lemon, 1991: Characteristics of mesocyclones detected during a NEXRAD test. Preprints, *25th Int. Conf. on Radar Meteorology*, Paris, France, Amer. Meteor. Soc., 39–42.

Coffer, B. E., Parker, M. D., Thompson, R. L., Smith, B. T., and Jewell, R. E., 2019: Using near-ground storm relative helicity in supercell tornado forecasting. *Wea. Forecasting*, **34,** 1417-1435, https://doi.org/10.1175/WAF-D-19-0115.1.

Coniglio, M. C., and Parker, M. D., 2020: Insights into supercells and their environments from three decades of targeted radiosonde observations. *Mon. Wea. Rev.*, **148**, 4893-4915, https://doi.org/10.1175/MWR-D-20-0105.1.

Conway, J. W., and D. S. Zrnićc., 1993: A study of embryo production and hail growth using dual-Doppler and multiparameter radar. *Mon. Wea. Rev.* **121**, 2511–2528.

Cooper, D.T., and A. B. Vorst, 2016: Assessing the utility of normalized rotation in detecting tornado development along the Allegheny front. Northeast Regional Operational Workshop XVII, Albany, NY.

Crowe, C. C., W. A. Petersen, L. D. Carey, and D. J. Cecil, 2010: A dual-polarization investigation of tornado-warned cells associated with Hurricane Rita (2005). *Electron. J. Oper. Meteorol.*, **4**, 1–25.

Crowe, C. C., C. J. Schultz, M. Kumjian, L. D. Carey, and W. A. Petersen, 2012: Use of dual-polarization signatures in diagnosing tornadic potential. *Electron. J. Oper. Meteor*., **13**, 57-87.

Davies-Jones, R., 1984: Streamwise vorticity: The origin of updraft rotation in supercell storms. *J. Atmos. Sci.*, **41**, 2991–3006, https://doi.org/10.1175/1520-0469(1984)041<2991:SVTOOU>2.0.CO;2.

— —, 1990: Midget supercell spawns tornadoes. *Weatherwise*, **43**, 260-261.

— —, 2006: Hurricane and tropical cyclone tornado environments from RUC proximity soundings. *23rd Conf. on Severe Local Storms*, 12.6A, St. Louis, MO, Amer. Meteor. Soc.

— —, 2015: A review of supercell and tornado dynamics. *Atmos. Res.*, **158–159**, 274–291, doi:10.1016/j.atmosres.2014.04.007.

Dawson, D. T., II, Mansell, E. R., Jung, Y., Wicker, L. J., Kumjian, M. R., and Xue, M., 2014: Low-Level Z_{DR} signatures in supercell forward flanks: the role of size sorting and melting of hail. *J. Atmos. Sci.*, **71**, 276-299.

— —, II, Mansell, E. R., and Kumjian, M. R., 2015: Does wind shear cause hydrometeor size sorting? *J. Atmos. Sci.*, **72**, 340–348, https://doi.org/10.1175/JAS-D-14-0084.1.

Devanas, A. D., D. Gregoria, K. B. Kasper, and P. Santos, 2008: Tropical cyclone induced tornadoes associated with the formation of Tropical Storm Barry. *Tropical Meteorology Special Symp./20th Conf. on Climate Variability and Change*, New Orleans, LA, Amer. Meteor. Soc., JP3.16. [Available online at https://ams.confex.com/ams/pdfpapers/131758.pdf.]

Doswell C. A. III, and Burgess D. W., 1993: Tornadoes and tornadic storms: A review of conceptual models. *The Tornado: Its Structure, Dynamics, Prediction, and Hazards, Geophys. Monogr*., Vol. 79, Amer. Geophys. Union, 161–172.

Durran, D. R., and L. W. Snellman, 1987: The diagnosis of synoptic-scale vertical motion in an operational environment. *Wea. Forecasting*, **2**, 17-31, https://doi.org/10.1175/1520- 0434(1987)002%3C0017:TDOSSV%3E2.0.CO;2

Edwards, R., 2012: Tropical cyclone tornadoes: A review of knowledge in research and prediction. *Elec. J. Severe Storms Meteor.*, **7(6)**, 1-33.

Fritz, C., and Wang, Z., 2013: A numerical study of the impacts of dry air on tropical cyclone formation: A development case and a nondevelopment case. *J. Atmos. Sci.*, **70**, 91-111, https://doi.org/10.1175/JAS-D-12-018.1.

Gentry, R. C., 1983: Genesis of tornadoes associated with hurricanes. *Mon. Wea. Rev.*, **111**, 1793–1805.

Green, B. W., F. Zhang, and P. M. Markowski, 2011: Multiscale processes leading to supercells in the landfalling outer rainbands of Hurricane Katrina (2005). *Wea. Forecasting*, **26**, 828–847.

Herzegh, P. H., and Jameson, A. R., 1992: Observing precipitation through dual-polarization radar measurements. *Bull. Amer. Meteor. Soc.*, **73**, 1365-1376, https://doi.org/10.1175/1520-0477(1992)073<1365:OPTDPR>2.0.CO;2.

Houston, A. L., Thompson, R.L., and R. Edwards, 2008: The optimal bulk wind differential depth and the utility of the upper-tropospheric storm-relative flow for forecasting supercells. *Wea. Forecasting*., **23**, 825–837, doi:10.1175/2008WAF2007007.1.

Hubbert, J., Bringi, V. N., Carey, L. D., and Bolen, S., 1998: CSU-CHILL Polarimetric radar measurements from a severe hail storm in eastern Colorado. *J. Appl. Meteor. Climatol.*, **37**, 749-775, https://doi.org/10.1175/1520-0450(1998)037<0749:CCPRMF>2.0.CO;2.

Jones, T. A., McGrath, K. M., and Snow, J. T., 2004: Association between NSSL mesocyclone detection algorithm-detected vortices and tornadoes. *Wea. Forecasting*, **19**, 872-890, https://doi.org/10.1175/1520-0434(2004)019<0872:ABNMDA>2.0.CO;2.

Kerr, B. W., and G. L. Darkow, 1996: Storm-relative winds and helicity in the tornadic thunderstorm environment. *Wea. Forecasting*, **11**, 489–505, https://doi.org/10.1175/1520- 0434(1996)0112.0.CO;2.

Kingfield, D. M., and Picca, J. C., 2018: Development of an operational convective nowcasting algorithm using raindrop size sorting information from polarimetric radar data. *Wea. Forecasting*, **33**, 1477-1495, https://doi.org/10.1175/WAF-D-18-0025.1.

Knupp, K. R., J. R. Stalker, and E. W. McCaul, 1998: An observational and numerical study of a mini-supercell storm. *Atmos. Res.*, **49**, 35-63.

— —, J. Walters, and M. Biggerstaff, 2006: Doppler profiler and radar observations of boundary layer variability during the landfall of Tropical Storm Gabrielle. *J. Atmos. Sci*., **63**, 234–251.

Kumjian, M. R., and A. V. Ryzhkov, 2007: Polarimetric characteristics of tornadic and nontornadic supercell thunderstorms. Preprints, *33rd Conf. on Radar Meteorology*, Cairns, Queensland, Australia, Amer. Meteor. Soc., P10.1. [Available online at http://ams.confex.com/ams/pdfpapers/122882.pdf.].

— —, Ryzhkov, A. V., 2008: Polarimetric signatures in supercell thunderstorms. *J. Appl. Meteor. Climatol.*, **47,** 1940-1961, https://doi.org/10.1175/2007JAMC1874.1

— —, Ryzhkov, A. V., 2009: Storm-relative helicity revealed from polarimetric radar measurements. *J. Atmos. Sci.*, **66,** 667-685, https://doi.org/10.1175/2008JAS2815.1.

— —, Ryzhkov, A. V., Melnikov, V. M., and Schuur, T. J., 2010: Rapid-scan super-resolution observations of a cyclic supercell with a dual-polarization WSR-88D. *Mon. Wea. Rev.*, **138,** 3762-3786, https://doi.org/10.1175/2010MWR3322.1.

— —, 2013: Principles and applications of dual-polarization weather radar. Part I: Description of the polarimetric radar variables. *J. Operational Meteor.*, **1**, 226–242, http://dx.doi.org/10.15191/nwajom.2013.0119.

— —, Khain, A. P., Benmoshe, N., Ilotoviz, E., Ryzhkov, A. V., and Phillips, V. T. J., 2014: The anatomy and physics of Z_{DR} Columns: Investigating a polarimetric radar signature with a spectral bin microphysical model. *J. Appl. Meteor. Climatol.*, **53(7),** 1820-1843, https://doi.org/10.1175/JAMC-D-13-0354.1.

— —, Lombardo, K., and Loeffler, S., 2021: The evolution of hail production in simulated supercell storms. *J. Atmos. Sci.,* **78,** 3417-3440, https://doi.org/10.1175/JAS-D-21-0034.1.

Lemon, L. R. and C. A. Doswell, 1979: Severe thunderstorm evolution and mesocyclone structure as related to tornadogenesis. *Mon. Wea. Rev.*, **107,** 1184–1197, doi:10.1175/1520-0493(1979)1072.0.CO;2

Lin, Y., and M. R. Kumjian, 2022: Influences of CAPE on hail production in simulated supercell storms. *J. Atmos. Sci.*, **79**, 179–204, https://doi.org/10.1175/JAS-D-21-0054.1.

Liu, H., and Chandrasekar, V., 2000: Classification of hydrometeors based on polarimetric radar measurements: Development of fuzzy logic and neuro-fuzzy systems, and in situ verification. *J. Atmos. Oceanic Technol.*, **17**, 140-164, https://doi.org/10.1175/1520-0426(2000)017<0140:COHBOP>2.0.CO;2.

Loeffler, S. D., and Kumjian, M. R., 2018: Quantifying the separation of enhanced Z_{DR} and K_{DP} regions in nonsupercell tornadic storms. *Wea. Forecasting*, **33**, 1143-1157, https://doi.org/10.1175/WAF-D-18-0011.1.

— —, M. R. Kumjian, M. Jurewicz, and M. M. French, 2020: Differentiating between tornadic and nontornadic supercells using polarimetric radar signatures of hydrometeor size sorting. *Geophys. Res. Lett*., **47**, 1–9, https://doi.org/10.1029/2020GL088242.

Markowski, P. M., Rasmussen E. N., and Straka J. M., 1998: The occurrence of tornadoes in supercells interacting with boundaries during VORTEX-95. *Wea. Forecasting*, **13**, 852–859.

— —, 2002: Hook echoes and rear-flank downdrafts: A review. *Mon. Wea. Rev.*, **130**, 852-876, https://doi.org/10.1175/1520-0493(2002)130<0852:HEARFD>2.0.CO;2.

— —, C. Hannon, J. Frame, E. Lancaster, A. Pietrycha, R. Edwards, and R. L. Thompson, 2003: Characteristics of vertical wind profiles near supercells obtained from the Rapid Update Cycle. *Wea. Forecasting*, **18**, 1262–1272, doi:10.1175/1520-0434(2003)018<1262:COVWPN>2.0.CO;2.

— —, Richardson, Y., Rasmussen, E., Straka, J., Davies-Jones, R., and Trapp, R. J., 2008: Vortex lines within low-level mesocyclones obtained from pseudo-dual-Doppler radar observations. *Mon. Wea. Rev.*, **136,** 3513-3535, https://doi.org/10.1175/2008MWR2315.1.

— —, and Y. Richardson, 2014: The influence of environmental low-level shear and cold pools on tornadogenesis: Insights from idealized simulations. *J. Atmos. Sci.*, **71**, 243–275, doi:10.1175/JAS-D-13-0159.1.

Martinaitis, S. M., 2017: Radar observations of tornado-warned convection associated with tropical cyclones over Florida. *Wea. Forecasting*, **32**, 165-186, https://doi.org/10.1175/WAF-D-16-0105.1.

Mashiko, W., 2016a: A numerical study of the 6 May 2012 Tsukuba City supercell tornado. Part I: Vorticity sources of low-level and midlevel mesocyclones. *Mon. Wea. Rev.*, **144**, 1069–1092, https://doi.org/10.1175/MWR-D-15-0123.1.

May, R. M., S. C. Arms, P. T. Marsh, E. Bruning, and J. R. Leeman, 2017: MetPy: A Python package for meteorological data. Unidata. [Available online at https://github.com/Unidata/MetPy.] https://doi.org/10.5065/D6WW7G29.

McCaul, E. W., Jr., 1991: Buoyancy and shear characteristics of hurricane-tornado environments. *Mon. Wea. Rev.*, **119**, 1954-1978, https://doi.org/10.1175/1520-0493(1991)119<1954:BASCOH>2.0.CO;2.

— —, and M. L. Weisman, 1996: Simulations of shallow supercell storms in landfalling hurricane environments. *Mon. Wea. Rev*., **124**, 408–429.

— —, D. E. Buechler, S. J. Goodman, and M. Cammarta, 2004: Doppler radar and lightning network observations of a severe outbreak of tropical cyclone tornadoes. *Mon. Wea. Rev.*, **132**, 1747–1763.

Molinari, J., and D. Vollaro, 2008: Extreme helicity and intense convective towers in Hurricane Bonnie. *Mon. Wea. Rev*., **136**, 4355–4372.

— —, and D. Vollaro, 2010: Distribution of helicity, CAPE, and shear in tropical cyclones. *J. Atmos. Sci.*, **67**, 274-284.

Moller, A. R., C. A. Doswell III, M. P. Foster, and G. R. Woodall, 1994: The operational recognition of supercell thunderstorm environments and storm structures. *Wea. Forecasting*, **9**, 327-347.

Novlan, D. J., and Gray, W. M., 1974: Hurricane-spawned tornadoes. *Mon. Wea. Rev.*, **102,** 476-488.

Nowotarski, C. J., Markowski, P. M., Richardson, Y. P., and Bryan, G. H., 2015: Supercell low-level mesocyclones in simulations with a sheared convective boundary layer. *Mon. Wea. Rev.*, **143,** 272-297, https://doi.org/10.1175/MWR-D-14-00151.1.

— —, Spotts, J., Edwards, R., Overpeck, S., and Woodall, G. R., 2021: Tornadoes in Hurricane Harvey. *Wea. Forecasting*, **36,** 1589-1609, https://doi.org/10.1175/WAF-D-20-0196.1.

Orf, L., R. Wilhelmson, B. Lee, C. Finley, and A. Houston, 2017: Evolution of a long-track violent tornado within a simulated supercell. *Bull. Amer. Meteor. Soc.*, **98**, 45– 68, doi:10.1175/BAMS-D-15-00073.1.

Palmer, R. D., and Coauthors, 2011: Observations of the 10 May 2010 tornado outbreak using OU-PRIME: Potential for new science with high-resolution polarimetric radar. *Bull. Amer. Meteor. Soc*., **92**, 871–891, doi:10.1175/2011BAMS3125.1.

Parker, M. D., 2014: Composite VORTEX2 Supercell environments from near-storm soundings. *Mon. Wea. Rev.*, **142,** 508-529, https://doi.org/10.1175/MWR-D-13-00167.1.

Picca, J., and A. Ryzhkov, 2012: A dual-wavelength polarimetric analysis of the 16 May 2010 Oklahoma City extreme hailstorm. *Mon. Wea. Rev.,* **140**, 1385–1403, https://doi.org/10.1175/MWR-D-11- 00112.1.

Potvin, C. K., K. L. Elmore, and S. J. Weiss, 2010: Assessing the impacts of proximity sounding criteria on the climatology of significant tornado environments. *Wea. Forecasting*, **25**, 921-930, https://doi.org/10.1175/2010WAF2222368.1

Rasmussen, E. N., and D. O. Blanchard, 1998: A baseline climatology of sounding-derived supercell and tornado forecast parameters. *Wea. Forecasting*, **13**, 1148–1164, doi:10.1175/1520-0434(1998)013<1148:ABCOSD>2.0.CO;2.

Romine, G. S., Burgess, D. W., and Wilhelmson, R. B., 2008: A dual-polarization-radar-based assessment of the 8 May 2003 Oklahoma City area tornadic supercell. *Mon. Wea. Rev.*, **136**, 2849-2870, https://doi.org/10.1175/2008MWR2330.1.

Ryzhkov, A. V., S. E. Giangrande, V. M. Melnikov, and T. J. Schuur, 2005: Calibration issues of dual-polarization radar measurements. *J. Atmos. Oceanic Technol*., **22**, 1138–1155, https://doi.org/10.1175/JTECH1772.1.

— —, Schuur, T. J., Burgess, D. W., and Zrnić, D. S., 2005: Polarimetric tornado detection. *J. Appl. Meteor.*, **44**, 557-570, https://doi.org/10.1175/JAM2235.1.

Scharfenberg, K. A., Miller, D. J., Schuur, T. J., Schlatter, P. T., Giangrande, S. E., Melnikov, V. M., Burgess, D. W., Andra, D. L., Jr., Foster, M. P., and Krause, J. M., 2005: The joint polarization experiment: Polarimetric radar in forecasting and warning decision making. *Wea. Forecasting*, **20,** 775-788, https://doi.org/10.1175/WAF881.1.

Schneider, D., and Sharp, S., 2007: Radar signatures of tropical cyclone tornadoes in central North Carolina. *Wea. Forecasting*, **22**, 278-286, https://doi.org/10.1175/WAF992.1.

Schultz, L. A., and D. J. Cecil, 2009: Tropical cyclone tornadoes, 1950–2007. *Mon. Wea. Rev.* **137**, 3471-3484, https://doi.org/10.1175/2009MWR2896.1.

Seliga, T. A., and Bringi, V. N., 1976: Potential use of radar differential reflectivity measurements at orthogonal polarizations for measuring precipitation. *J. Appl. Meteor. Climatol.*, **15**, 69-76, https://doi.org/10.1175/1520-0450(1976)015<0069:PUORDR>2.0.CO;2.

Sessa, M. F., and Trapp, R. J., 2020: Observed relationship between tornado intensity and pretornadic mesocyclone characteristics. *Wea. Forecasting*, **35(4)**, 1243-1261, https://doi.org/10.1175/WAF-D-19-0099.1.

Snyder, J. C., A. V. Ryzhkov, M. R. Kumjian, A. P. Khain, and J. Picca, 2015: A Z_{DR} column detection algorithm to examine convective storm updrafts. *Wea. Forecasting*, **30**, 1819– 1845, https://doi.org/10.1175/WAF-D-15- 0068.1.

Spratt, S. M., and A. J. Nash, 1995: Central Florida WSR-88D observations and NWSO operations during Tropical Cyclones Alberto, Beryl and Gordon, 1994: Preprints, *17th Conf. on Hurricanes and Tropical Meteorology*, Miami, FL, Amer. Meteor. Soc., 298–300.

— —, Sharp, D. W., Welsh, P., Sandrik, A., Alsheimer, F., and Paxton, C., 1997: A WSR-88D assessment of tropical cyclone outer rainband tornadoes. *Wea.*

Forecasting, **12,** 479-501, https://doi.org/10.1175/1520-0434(1997)012<0479:AWAOTC>2.0.CO;2.

Stumpf, G. J., Witt A., Mitchell E. D., Spencer P. L., Johnson J. T., Eilts M. D., Thomas K. W., and Burgess D. W., 1998: The National Severe Storms Laboratory mesocyclone detection algorithm for the WSR-88D. *Wea. Forecasting*, **13,** 304–326.

Thompson, R. L., R. Edwards, J. A. Hart, K. L. Elmore, and P. Markowski, 2003: Close proximity soundings with supercell environments obtained from the Rapid Update Cycle. *Wea. Forecasting*, **18**, 1243–1261, doi:10.1175/1520-0434(2003)018<1243:CPSWSE>2.0.CO;2.

— —, Mead, C. M., and Edwards, R., 2007: Effective storm-relative helicity and bulk shear in supercell thunderstorm environments. *Wea. Forecasting*, **22**, 102-115, https://doi.org/10.1175/WAF969.1.

Thompson, E. J., S. A. Rutledge, B. Dolan, M. Thurai, and V. Chandrasekar, 2018: Dual-polarization radar rainfall estimation over tropical oceans. *J. Appl. Meteor. Climatol.*, **57**, 755–775, https://doi.org/10.1175/JAMC-D-17-0160.1.

Tokay, A., P. G. Bashor, E. Habib, and T. Kasparis, 2008: Raindrop size distribution measurements in tropical cyclones. *Mon. Wea. Rev.*, **136**, 1669–1685, https://doi.org/10.1175/2007MWR2122.1.

Trapp, R. J., G. J. Stumpf, and K. L. Manross, 2005: A reassessment of the percentage of tornadic mesocyclones. *Wea. Forecasting*, **20**, 680–687, doi:10.1175/WAF864.1.

Turnage, T.J., 2014: An evaluation of normalized rotation vorticity couplets to assess tornadic mesocyclone potential, *27th Conf. of Severe Local Storms*, Madison, WI, Amer. Meteor. Soc.

Van Den Broeke, M. S., Straka, J. M., and Rasmussen, E. N., 2008: Polarimetric radar observations at low levels during tornado life cycles in a small sample of classic southern plains supercells. *J. Appl. Meteor. Climatol.*, **47**, 1232-1247, https://doi.org/10.1175/2007JAMC1714.1.

— —, and Jauernic, S. T., 2014: Spatial and temporal characteristics of polarimetric tornadic debris signatures. *J. Appl. Meteor. Climatol.*, **53**, 2217-2231.

— —, 2016: Polarimetric variability of classic supercell storms as a function of environment. *J. Appl. Meteor. Climatol.*, **55**, 1907-1925, https://doi.org/10.1175/JAMC-D-15-0346.1.

— —, 2017: Polarimetric radar metrics related to tornado life cycles and intensity in supercell storms. *Mon. Wea. Rev.*, **145**, 3671-3686, https://doi.org/10.1175/MWR-D-16-0453.1.

— —, 2020: A preliminary polarimetric radar comparison of pretornadic and nontornadic supercell storms. *Mon. Wea. Rev.*, **148**, 1567-1584, https://doi.org/10.1175/MWR-D-19-0296.1.

Weisman, M. L., and J. B. Klemp, 1982: The dependence of numerically simulated convective storms on vertical wind shear and buoyancy. *Mon. Wea. Rev*., **110**, 504-520.

Wilhelmson, R. B., and Klemp, J. B., 1978: A numerical study of storm splitting that leads to long-lived storms. *J. Atmos. Sci.*, **35(10),** 1974-1986.

Wilson, M. B., and M. S. Van Den Broeke, 2021: An automated Python algorithm to quantify Z_{DR} arc and K_{DP}–Z_{DR} separation signatures in supercells. *J. Atmos. Oceanic Technol.*, **38**, 371–386, https://doi.org/10.1175/JTECH-D-20-0056.1.

— —, and Van Den Broeke, M. S., 2022: Using the Supercell Polarimetric Observation Research Kit (SPORK) to examine a large sample of pretornadic and nontornadic supercells. *Elec. J. Severe Storms Meteor*, **17**, 1-38, https://doi.org/10.55599/ejssm.v17i2.85.

NWS, 2012: Hurricane Irene, August 21–30, 2011. NOAA/NWS Service Assessment, 129 pp. [Available online at http://www.nws.noaa.gov/om/assessments/pdfs/Irene2012.pdf.]

Yokota, S., H. Niino, H. Seko, M. Kunii, and H. Yamauchi, 2018: Important factors for tornadogenesis as revealed by high-resolution ensemble forecasts of the Tsukuba

supercell tornado of 6 May 2012 in Japan. *Mon. Wea. Rev.*, **146**, 1109–1132, https://doi.org/10.1175/MWR-D-17-0254.1.

Zrnić, D. S., and Ryzhkov, A. V., 1999: Polarimetry for weather surveillance radars. *Bull. Amer. Meteor. Soc.*, **80**, 389-406, https://doi.org/10.1175/1520-0477(1999)080<0389:PFWSR>2.0.CO;2.